

I: Variability of the outgoing thermal IR spectra and its
application in GCM validation

II: The detection of cloud/aerosol in the outgoing thermal
IR spectra

Thesis by

Xianglei Huang

In Partial Fulfillment of the Requirements

for the Degree of

Doctor of Philosophy



California Institute of Technology

Pasadena, California

2004

(Defended April 12, 2004)

© 2004

Xianglei Huang

All Rights Reserved

Acknowledgement

First and foremost, I thank Yuk L. Yung, my thesis advisor, for his encouragement and advice, for serving as a role model with his enthusiasm and curiosity about nature as well as his remarkable industriousness and dedication. With Yuk's support and encouragement, I was able to attend the 11th AMS atmospheric radiation conference, the GRC Solar radiation conference, and several workshops at UCLA IPAM. I have benefited enormously from these conferences and workshops. I also wish to thank other members in my thesis committee: Andy Ingersoll, Paul Wennberg, Tapio Schneider, Jim Randerson, and Mark Richardson. I have learned a lot about geophysical fluid dynamics and atmospheric general circulation from Andy and Tapio. Having been TA for Paul's class three times was a useful experience for me. The work about Mars could not have been done without generous help from Mark.

I am greatly indebted to Professor Richard Goody for his frequent help during my junior years. I benefited a lot from his insightful comments and suggestions. I am very thankful to John Farrara at UCLA, Stephen Leroy and Jack Margolis at JPL. The collaborations with them have been fruitful and I have learned a lot from them too.

I was lucky to take many classes taught by extraordinarily excellent and dedicated teachers. I thank Peter Goldreich for his fantastic Ge103 lectures. I wish to acknowledge Bradford Sturtevant in Aeronautics for the one-student-one-teacher class that he taught before he passed away. His dedication to teaching impresses me most. I also thank Anthony Leonard in Aeronautics for the three-term training in CFD which was full of challenges but very rewarding.

I am very thankful to Mike Black and other staff at the Planetary Science office, Irma Black, Leticia Calderon, Nora Oshima and Loreta Young, for their help and support. I also thank NCAR Super Computing Division for kindly providing computer resources for part of my simulation works.

I am greatly indebted to Mimi Gerstell. She has proofread all manuscripts that I submitted. I truly appreciate many enjoyable scientific discussions that I have had with other graduate students and postdoctoral scholars, especially Zhiming Kuang and David Noone. The discussions with Dave C. Camp, Chris Walker, Junjun Liu, Helen Wang were also useful. I am very thankful to other members in Yuk's climate group, especially Yibo Jiang and Run-lie Shia for their useful comments and suggestions. I also appreciate Shengnian Luo and Chen Ji from seismology lab and Yajun Mei from mathematics for the discussions that have broadened my knowledge about the inverse problem. I wish to thank Linsen Zeng, Jing Liu, Zhengrong Wang and Xinkai Wu. Without them, the stay in Southern California would have been without so much fun. Also, I am indebted to Robert Sharp, Leon Silver, Jason Saleeby, and Paul Asimow for the unforgettable 2003 Pahoehoe trip.

It is not possible for me to show all my appreciation to my parents for their eternally unselfish support and love to their son, for their nurturing my curiosity in many ways when I was a child, for the family tradition in academic excellence. Last but not least, many thanks to my wife, Shun Han, for taking care of everything when I was tied up with thesis research. Her love and support have been, and continue to be, uniquely important to me.

Table of Contents

Part I: Variability of the outgoing thermal infrared spectra	1
Chapter 1: An introduction to the observations of the outgoing thermal IR spectra and their application in climate studies	2
1.1 A brief history of the measurement of the outgoing thermal IR spectra	3
1.2 Climate change detected from the space-borne observations of the outgoing thermal IR spectra	4
1.3 Using the outgoing thermal infrared observation to test model variability	11
1.4 Summary	17
1.5 Acknowledgement	18
1.6 Appendix: Details of simulating IMG-IRIS difference	18
1.7 Reference	19
Chapter 2: Temporal Variability of the Thermal IR Spectra Seen from IRIS Data and GCM Simulations	25
2.1 Abstract	26
2.2 Data and methodology	27
2.3 The tropical cases	33
2.4 The midlatitude cases	48
2.5 Conclusion	58
2.6 Acknowledgement	59
2.7 Appendix	60
2.8 Reference	64

Chapter 3: Spatial variability of the outgoing thermal IR spectra seen from AIRS data and CAM2 simulations	71
3.1 Abstract	72
3.2 AIRS and data manipulation	73
3.3 The tropical/subtropical oceans	76
3.4. The midlatitude oceans	87
3.5 Results from CAM2 simulation	94
3.6 Conclusion and discussion	103
3.7 Acknowledgement	104
3.8 References	105
Chapter 4: The spatial and temporal variability of the Martian outgoing thermal IR spectra seen from MGS-TES data	112
4.1 Abstract	113
4.2 Introduction and data manipulation	114
4.3 The spatial-spectral variability seen from TES tropical data	116
4.4 The temporal-spectral variability seen from TES tropical data	121
4.5 Summary	124
4.6 Acknowledgement	126
4.7 References	126
Part II: The detection of cirrus/dust aerosol from the thermal IR spectra	129
Chapter 5: High-resolution thermal IR detection and characterization of cirrus from the retrieval point of view	130
5.1 Abstract	131

5.2 Introduction	132
5.3 A simplified analytic model	136
5.4 Line-by-line model and sensitivity studies	141
5.5 More considerations about realistic retrieval	148
5.6 Summary	156
5.7 Acknowledgement	157
5.8 Reference	157
Chapter 6: Detecting dust, water ice cloud and surface anisothermality from the Martian low-resolution outgoing thermal IR spectra: a tri-spectral approach	162
6.1 Abstract	163
6.2 Description of tri-spectral algorithm	164
6.3 Sensitivity studies with a line-by-line radiative transfer model	167
6.4 Case studies and comparison with TES retrievals	170
6.5 Summary	179
6.6 Acknowledgement	179
6.7 References	180

List of Figures

Figure 1.1 The wintertime IMG-IRIS difference spectrum	7
Figure 1.2 Simulated IMG-IRIS difference spectrum	9
Figure 1.3 10-month averages and standard deviations of IRIS spectra and synthetic spectra based on GCM simulations.	14
Figure 2.1 Standard deviations of synthetic spectra derived from the UCLA GCM	32
Figure 2.2 Mean spectra over the central Pacific and the western Pacific	35
Figure 2.3 PC1s over the central Pacific and the western Pacific	36
Figure 2.4 PC1 time series over the central Pacific and the western Pacific	38
Figure 2.5 PC1s from several sensitivity studies	43
Figure 2.6 Mean spectra over the northern Pacific and the southern Pacific	47
Figure 2.7 PC1s over the northern Pacific and the southern Pacific	52
Figure 2.8 PC1 time series over the northern Pacific and the southern Pacific	53
Figure 2.9 Standard deviations of 25-day averaged temperature profiles	53
Figure 2.10 Retrieved vertical profiles from the PC1s over the northern Pacific	55
Figure 2.11 Retrieved vertical profiles from the PC1s over the southern Pacific	55
Figure 2.12 Retrieved upper tropospheric water vapor profiles	57
Figure 2.13 The original PC1s and the residual spectra after fit	63
Figure 3.1 Number of spectra used for averaging in each grid box	75

Figure 3.2 Mean AIRS spectrum over the tropical/subtropical oceans	75
Figure 3.3 Three leading PCs of AIRS over the tropical/subtropical oceans	80
Figure 3.4 The spatial maps of three leading PCs shown in Figure 3.3	81
Figure 3.5 (a) The climatological high cloud amount in July. (b) The climatological low cloud amount in July. (c) The 850mb relative humidity. (d) The mean temperature in the layer of 150-70mb	82
Figure 3.6 A schematic plot to demonstrate the EOF analysis results	84
Figure 3.7 The PC2 spatial maps of the simulated clear-sky and cloudy cases	87
Figure 3.8 Two leading PCs of AIRS over the NHMO and the SHMO	90
Figure 3.9 (a) The PC2 spatial map over the NHMO. (b) The climatological low cloud amount in July over the NHMO. (c) The PC2 spatial map over the SHMO. (d) 100mb temperature over the SHMO	91
Figure 3.10 PC2s and their spatial maps derived from NCEP+ISCCP case	92
Figure 3.11 PC2s from spatial-spectral EOF analysis of January AIRS data over the NHMO and SHMO	94
Figure 3.12 Sensitivity of PCs to the spectral resolution	95
Figure 3.13 Three leading PCs and their spatial maps over the tropical/subtropical oceans based on CAM2 simulation	96
Figure 3.14 observed and simulated OLR and precipitation anomaly of July 2003	99
Figure 3.15 Simulated PC2s and their spatial maps over the NHMO and SHMO	102

Figure 4.1 Two leading PCs over the Martian tropics during three different periods in the first MGS mapping year	118
Figure 4.2 The spatial maps of the PCs shown in Figure 4.1	119
Figure 4.3 Topography of Mars smoothed over 10° latitude by 20 °longitude	119
Figure 4.4 PC1s and their time series and the time series of the target-temperature	123
Figure 4.5 PC2s and their time series	124
Figure 5.1 Schematic of three-layer atmosphere model	136
Figure 5.2 Plots of $L(x) = \exp(-\frac{C_2}{x^2 + 1}) - \exp(-\frac{C_1}{x^2 + 1})$ with three different combinations of C_2 and C_1	139
Figure 5.3 (a) Simulated outgoing spectrum from 930 to 938 cm^{-1} . (b) The residual spectrum	142
Figure 5.4 Simulated outgoing spectra from 744 to 748 cm^{-1} and 1260 to 1270 cm^{-1} and the corresponding residual spectra	143
Figure 5.5 Sensitivity of the shape of residual spectra to the spectral resolution	146
Figure 5.6 Sensitivity of residual spectra to cirrus optical depth and the altitude of the cirrus top	146
Figure 5.7 Sensitivity of residual spectra to errors in retrieved temperature profiles	152
Figure 6.1 Sensitivity of tri-spectral algorithm to cirrus and dust optical depth and the surface emissivity	169
Figure 6.2 Results of applying tri-spectral algorithm to 300 TES daytime spectra	171

- Figure 6.3 (a) A TES sample spectrum and a fit with the superposition of two areas with different surface temperatures. (b) The corresponding topography map 174
- Figure 6.4 Geographical distributions of all TES daytime spectral with $\Delta BT_{12.4-9} < 0$ and $\Delta BT_{e9-7.3} < 0$ over two periods 176
- Figure 6.5 Scatter-plot of the TES team's retrieved dust opacity vs. its retrieved ice opacity 178
- Figure 6.6 Geographical distribution of icy TES spectra classified by tri-spectral algorithm during a period of dust storm 179

List of Tables

Table 1.1 Major characteristics of IRIS and IMG	6
Table 2.1 The major features of UCLA GCM and UCNAR CAM 2.0	28
Table 2.2 Properties of the PC1s of IRIS and the two GCMs	37
Table 2.3 The correlation coefficients between three PC1 time series	39
Table 2.4 The standard deviations of monthly-averaged total cloud amount and high cloud amount derived from ISCCP products and CAM2 simulations	47
Table 2.5 The percentage of the total variance explained by the PC1s and the PC2s over the northern Pacific and the southern Pacific	51
Table 2.6 The correlation coefficients between three PC1 time series	51
Table 2.7 The goodness-of-fit statistics of each retrieval case	62
Table 3.1 The percentage of variance explained by three leading PCs	76
Table 3.2 The percentage of variance explained by three leading PCs over NHMO and SHMO	87
Table 3.3 The fraction of variance explained by three leading CAM2 PCs	96
Table 4.1 Summary of the fraction of total variance explained by PC1s and PC2s	118
Table 4.2 Summary of the fraction of total variance explained by PC1s and PC2s for two different regions	123
Table 5.1 The degrees of freedom for signal in the cases of clear sky and thin cirrus retrieval with different instrumental resolution (FWHM) and different NESR	155
Table 6.1 Summary of the tri-spectral algorithm	166

Overview

The theme of this thesis is studying the outgoing thermal IR spectra of Earth and Mars. It is divided into two parts: the first part (Chapters 1-4) is focused on the variability seen in the outgoing thermal IR spectra and its application in validating model simulation, and the second part (Chapters 5-6) concentrates on the detection of cirrus (cirrus/dust aerosol) from terrestrial (Martian) outgoing thermal IR spectra.

In Chapter 1, an example of climate change seen from two spectrometers separated by 26 years is used to illustrate the singular importance of the outgoing thermal IR spectra in climate observations. The importance of testing the variability of models and the feasibility of using the outgoing thermal IR spectra in such tests are discussed.

In Chapter 2, a study of the temporal variability at the tropical and midlatitude Pacific Oceans seen from IRIS (Infrared Interferometer Spectrometer) spectra and corresponding synthetic spectra based on simulations from two GCMs (UCLA GCM and NCAR CAM2) is presented. The discrepancies between modeled and observed temporal variability are substantial. The differences between two GCMs are also significant. Further examination shows that these discrepancies are insensitive to the parameterization of cloud optical properties and most likely due to deficiencies in simulating the seasonal and intraseasonal variations of the Walker Circulation in the tropical Pacific and the seasonal variations of boundary-layer temperature, low cloud, and stratospheric temperature in the midlatitude Pacific.

In Chapter 3, a survey of the spatial variability seen from AIRS (Atmospheric Infrared Sounder) spectra and corresponding synthetic spectra based on NCAR CAM2

simulation is presented. To a large extent, the simulated spatial variability agrees well with the observed counterpart. The major discrepancies between model and observation can be attributed to the incorrect location of ITCZ in the western Pacific, the underrepresented dust aerosol at the Arabian Sea and off the Atlantic Coast of North Africa, and the overestimated spatial variation of stratospheric temperature in the model.

Chapter 4 presents a comparative study of the temporal and spatial variability seen in the Martian outgoing thermal IR spectra collected by MGS-TES (Thermal Emission Spectrometer). Surface temperature variation is the dominant contributor to the temporal and spatial variability seen here. The variations of CO₂ column abundance, dust aerosol and water ice cloud associated with topography, as well as the imprint of dust storms, can be also seen from such analysis. The negative correlation between dust and water ice spectral features seen from this analysis suggests that, to some extent, dust and water ice cloud are mutually exclusive of each other in the Martian atmosphere.

Chapter 5 presents a sensitivity study of identifying optically thin cirrus from high-resolution (each individual absorption line is almost resolved) thermal IR spectra based on the line shapes of the residual spectra. This cirrus-detection approach is different from all previous cirrus-detection algorithms in the sense of making use of information content contained in the high-resolution measurements.

Chapter 6 presents a tri-spectral algorithm to detect water ice cloud, dust, and surface anisothermality from low-resolution Martian outgoing thermal IR spectra, such as MGS-TES spectra. This algorithm is complementary to any more sophisticated retrieval scheme and can be used to screen large amounts of data to get a quick overview.

Part I: Variability of the outgoing thermal
infrared spectra

Chapter 1: An introduction to the observations
of the outgoing thermal IR spectra and their
application in climate studies

1.1 A brief history of the measurement of the outgoing thermal IR spectra

In our solar system, all terrestrial planets emit radiation mainly in the thermal infrared portion of the electromagnetic spectrum (200 cm^{-1} to 2500 cm^{-1}). The photons emitted from the surface are absorbed then reemitted or scattered by various constituents in the planetary atmosphere, except on Mercury which has a vacuum-like atmosphere. The absorption and reemission are affected by the concentration of absorber as well as by the ambient temperature. The scattering process is affected by the concentrations, size distributions, and geometric shapes of the substances that scatter photons, mostly clouds and aerosols. All these processes are frequency-dependent. As a result, the outgoing thermal IR spectra recorded at the top of atmosphere (TOA) have plenty of information about surface and atmosphere. The higher the spectral resolution, the more information about the vertical profiles of the thermodynamic variables and trace gases concentrations the spectrum contains. Therefore, spectrally resolved and well-calibrated thermal IR radiance measured at TOA is a uniquely important quantity and particularly relevant to climate research [Goody *et al.*, 1998].

The first attempt to measure thermal IR spectra from a satellite was made in 1962 using an interferometer spectrometer with a resolution of 40 cm^{-1} and a spectral coverage from 660 cm^{-1} to 5550 cm^{-1} [Block and Zachor, 1964]. The errors in these measurements could be as much as 50% due to the flight control and calibrations [Block and Zachor, 1964]. Only a few spectra from this attempt and several following attempts have been published [Mertz, 1963; Block and Zachor, 1964; Lovett *et al.*, 1967], because of the difficulty of such measurement at that time. The first set of outgoing thermal IR spectra with good quality was obtained in 1969 by a Michelson interferometer on Nimbus 3,

IRIS-B (Infrared Interferometer Spectrometer) [Hanel *et al.*, 1970]. An improved version of IRIS-B, IRIS-D, aboard Nimbus 4 launched in 1970 [Hanel *et al.*, 1971] was a great success and collected around 700,000 good-quality spectra during its 10-month operation.

In the late 1970s and 1980s, only three Fourier transform infrared (FTIR) spectrometers aboard Soviet Meteor-2 series satellites with a resolution of 5 cm^{-1} occasionally measured thermal infrared spectra [Spankuch and Dohler, 1985]. In the meantime, the outgoing thermal IR spectra from Mars were taped by Mariner 9 in 1971, those from Venus were observed by Venera 15 in 1983, and those from the outer solar planets were observed by Voyager 1 and 2 in 1979 and 1980s. In 1996, the outgoing thermal IR spectra from Earth were measured globally again by IMG (Interferometric Monitor for Greenhouse gases), a FTIR spectrometer aboard a Japanese satellite ADEOS with a resolution of 0.1 cm^{-1} and a spectral coverage from 600 cm^{-1} to 3300 cm^{-1} . Thirty-two years after Hanel's great success with IRIS-D, the United States returned to this business with the launch of AIRS (Atmospheric Infrared Sounder) on EOS AQUA satellite. AIRS is a grating spectrometer with a resolving power of 1200 and a non-continuous spectral coverage from 650 cm^{-1} to 2700 cm^{-1} .

1.2 Climate change detected from the space-borne observations of the outgoing thermal IR spectra

This section presents a study of the difference in the spectrally resolved thermal radiances over the tropical ocean obtained by IRIS-D (for brevity, hereafter IRIS) and IMG separated by 26 years, focusing on the imprints of the secular changes of greenhouse gases (GHGs) reflected in the difference. A similar study has been done by Harries *et al.* [2001] using clear-sky IRIS and IMG data over the central Pacific.

1.2.1 Data Analysis

Table 1 lists the major instrument and orbit characteristics of IRIS and IMG based on Hanel *et al.* [1971; 1972] and Kobayashi *et al.* [1999]. We limit our study to the spectra over the tropical ocean, defined as the ocean between 20°S and 20°N, during the wintertime (December and January). The choice is necessitated by the relatively uniform radiative properties of oceanic surface and the limited data overlap by matching months between IMG and IRIS. Only the spectral range 650-1400 cm^{-1} is studied, because both IRIS and IMG have good enough signal-to-noise ratio (SNR) in this range. We do not categorize data as clear-sky and cloudy data, as others did with a brightness temperature threshold [Harries *et al.*, 2001; Haskins *et al.*, 1997; Iacono and Clough, 1996]. We doubt the reliability of using a brightness temperature threshold to select cloud-free spectra, especially in this case when the fields of view of IRIS and IMG are different by two orders of magnitude. On the other hand, cloud itself plays an important role in climate and cloud variation is at least as important as the changes of the greenhouse gases. Therefore, we do not classify data here as clear-sky and cloudy spectra. Instead, we study them all together. For IRIS, the number of spectra qualified for this study is 9268; for IMG, it is 2346.

	IRIS	IMG
Instrument Type	Michelson FTIR spectrometer	Michelson FTIR spectrometer
Spectral coverage	400-1600 cm ⁻¹	600-3030 cm ⁻¹ (three detectors)
Apodized spectral resolution	2.8 cm ⁻¹	0.1 – 0.25 cm ⁻¹
Signal-to-Noise Ration (SNR)	20 ⁱ -100 ⁱⁱ	200 ⁱ -2000 ⁱⁱ
Field of View	95 by 120 km	10 by 10 km
Operational Period	April 1970 – January 1971	November 1996 – June 1997
Orbit type	Sun-synchronous orbit of 1100-km altitude	Sun-synchronous orbit of 800-km altitude

ⁱ At the endpoints of the spectrum

ⁱⁱ At the mid-point of the spectrum

Table 1.1 Major characteristics of IRIS and IMG

We obtain the IRIS mean spectrum over the tropical ocean during wintertime by equally weighting the spectra collected during the ascending node (around local midnight) and the spectra collected during the descending node (around local noon) to minimize any potential diurnal aliasing. The IMG mean spectrum is obtained in the same way. Then the IMG mean spectrum is degraded to the same resolution as the IRIS mean spectrum and the effect of the different instrument fields of view between IRIS and IMG spectra is accounted for by convolving the IMG spectrum with a varying rectangular window [*Bell, 1972; Iacono and Clough, 1996*].

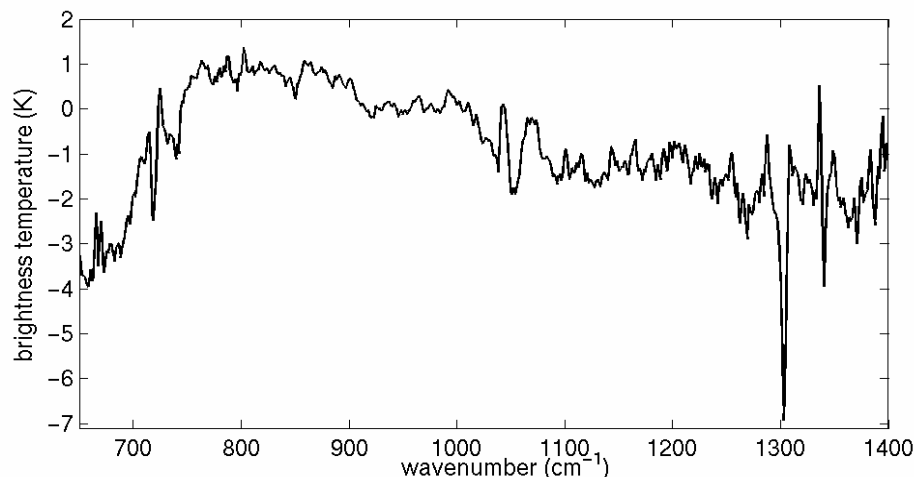


Figure 1.1 The IMG-IRIS difference spectrum for the tropical ocean between 20°S and 20°N over the wintertime (December and January).

The difference between the IMG and IRIS mean spectra (IMG-IRIS) is plotted in Figure 1.1. A number of features are apparent. The carbon dioxide 15 μm band (650-700 cm^{-1}) shows that the stratosphere of IMG wintertime is cooler than that of IRIS wintertime by several degrees. This result was anticipated by *Kiehl* [1983] and *Charlock* [1984]: the increase of carbon dioxide in the atmosphere results in a warming of the surface via the greenhouse effect and a greater rate of radiative cooling in the stratosphere. There is a -7 K change in the methane band (1306 cm^{-1}) between IMG and IRIS observations, partially due to the steady rise of atmospheric methane concentration from 1.35 to 1.75 ppmv between 1970 and 1996. According to the NCEP reanalysis [*Kalnay et al.*, 1996], the averaged SST difference between the IMG and IRIS wintertime is 0.42 K. Therefore the slope in the window regions (800-1000 cm^{-1} , 1100-1200 cm^{-1}) is due to either the differences of clouds between these two periods or the calibration errors, or some combination of these factors.

1.2.2 Modeling the IMG-IRIS difference

In order to further understand the IMG-IRIS difference, a simulation was carried out using the best available data for these two observing periods (see appendix for details). The surface measurements might be as accurate as needed to reproduce the IMG-IRIS difference while the vertical profiles are less reliable. The cloud data are no more than suggestive. Coincidentally, the cloud differences between these two periods are little; significant radiance differences due to the variability of clouds are more likely.

To first order, the simulated difference shown in Figure 1.2a is the sum of three factors, (1) the *forcings* due to the increase of the concentrations of greenhouse gases except water vapor; (2) the *responses* of climate system to these forcings: the climate system responds to forcing by adjusting the dependent variables such as temperature, humidity, and clouds, then those adjustments leave imprints in the outgoing thermal IR spectra; (3) the internal variability of these dependent variables in the climate system: the natural variability (for this case, the interannual variability) of these climate variables are comparable to or even larger than their responses to the given forcings.

Given that we have only two snapshots here, separating (2) and (3) is a difficult task beyond the scope of this study. The difference due to (2) and (3) together is shown in Figure 1.2b and the difference due to (1) is plotted in Figure 1.2c. The three factors are approximately additive (Figure 1.2, $a \approx b+c$) with the root-mean-square (rms) of the residual being 7% of the rms of the difference in Figure 1.2a. The results in Figure 1.2 show that the differences derived from the outgoing thermal IR spectra contain not only the spectrum of the *forcings*, but also the spectrum of the *responses*. Therefore, if the greenhouse gas concentrations are known accurately enough, the “forcing spectrum”

could be calculated and, to the first order, subtracted from the observed difference spectrum to give the spectrum of the *responses* plus internal variability.

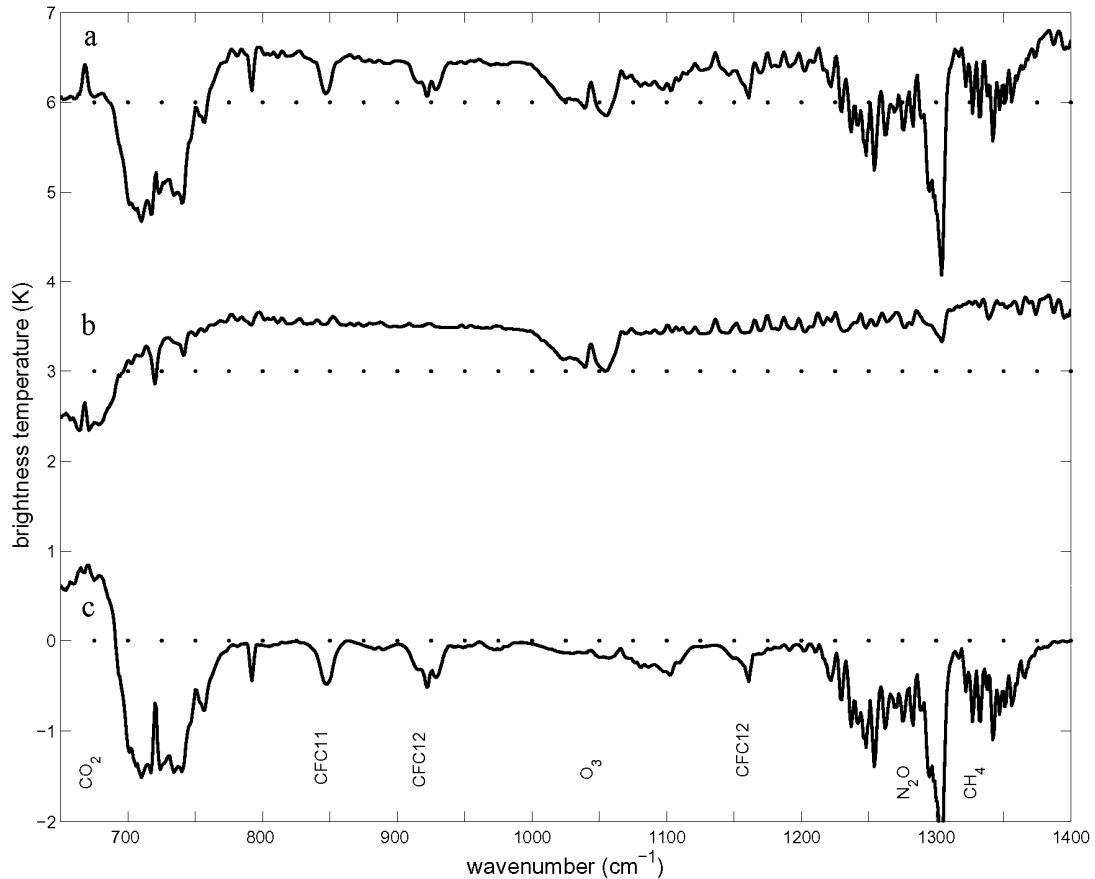


Figure 1.2 Simulated IMG-IRIS difference spectra over the same geographical zone and the months as those used in Figure 1.1. (a) Simulated difference from calculation including changes in both greenhouse gases and the dependent variables such as water vapor, temperature, and clouds, displaced by 6 K. (b) Same as (a) except that the greenhouse gases are held constant at 1970 values, displace by 3 K. (c) Same as (a) except that the water vapor, temperature and clouds are held constant at 1970 values.

Although the calibration information about IRIS and IMG is not complete, calibration errors are unlikely to have an effect on the shapes of those gas-absorption band profiles. Sampling errors are most likely too small to be important given the number

of spectra used and the relatively uniform spatial distributions of CO₂ and CH₄. Therefore, it is instructive to compare the shapes of spectral features in Figure 1.1 and Figure 1.2a. The most striking differences between these two curves are the spectral shapes in two CO₂ bands (667 cm⁻¹ and 720 cm⁻¹). The 667 cm⁻¹ CO₂ band is sensitive to stratospheric temperature: the weighting function at the band center peaks around 8 mb. The 720 cm⁻¹ CO₂ band is basically sensitive to the lower stratospheric and upper tropospheric temperature. Given the relatively uniform distribution of CO₂ in both horizontal and vertical directions, this striking difference indicates that the temperature profiles used here (from NCEP reanalysis data) contain errors in stratospheric and upper tropospheric temperature: either the stratospheric and upper tropospheric temperature is too cold during IRIS wintertime, or it is too warm during IMG wintertime. The methane band in Figure 1.1 peaks about 6K below its wings, while the best available data give only ~2 K in Figure 1.2a. Even taking the possible errors in the early measurements of methane and the NCEP reanalysis temperature in the upper troposphere into account explains no more than 4 K difference between the methane peak and the wings. We speculate there might be systematic calibration error in this spectral region.

Limited by the lack of calibration information and the paucity of IMG observations [*Brindley and Harries, 2003*], the IMG-IRIS difference presented here cannot yield very useful quantitative results. However, together with simulations, it clearly demonstrates the utility of such observations and the approaches to handle such data with cloudy situations included. This supports the view that, with careful consideration of the sampling problems, well-calibrated observations of the outgoing

spectrally resolved radiance over a long term can be used as a benchmark for climate monitoring [Goody *et al.*, 1998; Keith and Anderson, 2001].

1.3 Using the outgoing thermal infrared observation to test model variability

1.3.1 The importance of testing model second-moment statistics

Confidence in statements about the influence of anthropogenic activities on climate change and about climate change on decadal timescales depends upon the reliability of general circulation models (GCMs). GCMs should be tested against observations for their performance in various aspects before they can make credible prediction about future climate change. As a matter of fact, the climate sensitivity (defined as the increase of surface temperature caused by a doubling of CO₂) predicted by different GCMs is spread over a wide range (~1.5 K to 4.5 K) and this range has not been narrowed down in the last ten years [Houghton, 1990; Houghton, 1996; Houghton, 2001]. This fact shows the importance and necessity of testing GCMs.

The second-moment statistics predicted by a GCM should be particularly tested because of its relation to the prediction of climate change due to external forcings (in this context, the anthropogenic emission of GHGs). In a seminal paper, *Leith* [1975] applied the fluctuation-dissipation theorem (FDT) to show that there is a direct connection between the second-moment statistics of the climate system and the sensitivity of that climate system to external forcings. Recently, *Boffetta et al.* [2003] presented a generalization of FDT which holds for a finite amplitude perturbation. Even though FDT is rigorously valid only for a Liouville system, numerical works by *Bell* [1980] and *North et al.* [1993] demonstrated that, to a large degree, this theorem remains applicable to a truncated barotropic system and a GCM with all-land surface and no topography.

Therefore, testing the second-moment statistics from GCMs against their counterpart from the observations has special importance.

Here is an example showing that two GCMs can have good agreement on simulating the 10-month mean but that the considerable discrepancies can still exist in the second-moment statistics between the two GCMs and IRIS observations. UCLA GCM and NCAR CAM2 (Community Atmospheric Model Version 2) are forced by the realistic monthly-averaged SST over the IRIS period, April 1970 to January 1971. The twice-per-day outputs from the two GCMs are fed into a radiative transfer model, MODTRAN [Bernstein *et al.*, 1996], to generate synthetic IRIS-like spectra. Figure 1.3a shows the 10-month averaged mean spectrum over the western Pacific (90°-150°E, 10°S-10°N) from UCLA GCM, CAM2, and IRIS observations, respectively. The mean spectra from the two GCMs both agree well with IRIS mean spectra except at the CO₂ 667cm⁻¹ bandⁱ. For the whole spectral range, the root-mean-square (rms) difference between the UCLA GCM and IRIS mean spectra is 3.5K. For CAM2 and IRIS, it is 2.7K. The rms difference between UCLA GCM and CAM2 is 2.4K. But when the standard deviation of monthly-averaged spectra is studied, GCMs and observation show a substantial difference. At any point within this spectral range, the standard deviation derived from CAM2 simulation is at least twice as large as that derived from UCLA GCM. Meanwhile, the standard deviation of IRIS spectra is even larger than that of CAM2. Here, observation shows a greater variability than either GCM. Understanding causes of these discrepancies between observed and simulated variability would lead us to a better

ⁱ It turns out that tropical stratosphere in this UCLA GCM simulation does not have a realistic variability, partially due to the crude vertical resolution in the stratosphere. Therefore, temperature and humidity above the lower stratosphere are fixed in the radiative transfer calculation. The difference between UCLA and IRIS at CO₂ 667cm⁻¹ band just reflects the difference between fixed stratosphere temperature and real stratosphere temperature over IRIS period.

understanding of the deficiencies in the GCMs and even providing clues to improve the modeling work.

1.3.2 Using the outgoing thermal infrared spectra to test model variability

The comparison between models and observations is not restricted to standard model output parameters. Any quantity that can be calculated uniquely and accurately from the model can be used for the purpose of model testing. As mentioned in Section 1.1, the outgoing thermal IR spectrum contains plenty of information about the vertical profiles of the atmospheric thermodynamic variables and the trace gas concentrations. So it is physically meaningful to use such quantities to validate models. On the other hand, thermal infrared spectra also contain information about trace gases, which are usually prescribed in GCM simulation. But given the relatively uniform horizontal distributions and slow temporal variations of these trace gases, to the first order, the effects of those trace gases in observations can be removed by differencing an individual spectrum and the mean spectrum averaged over a certain area and a certain period. This is a practical reason for using thermal infrared spectra to test model variability rather than to test the model long-term mean.

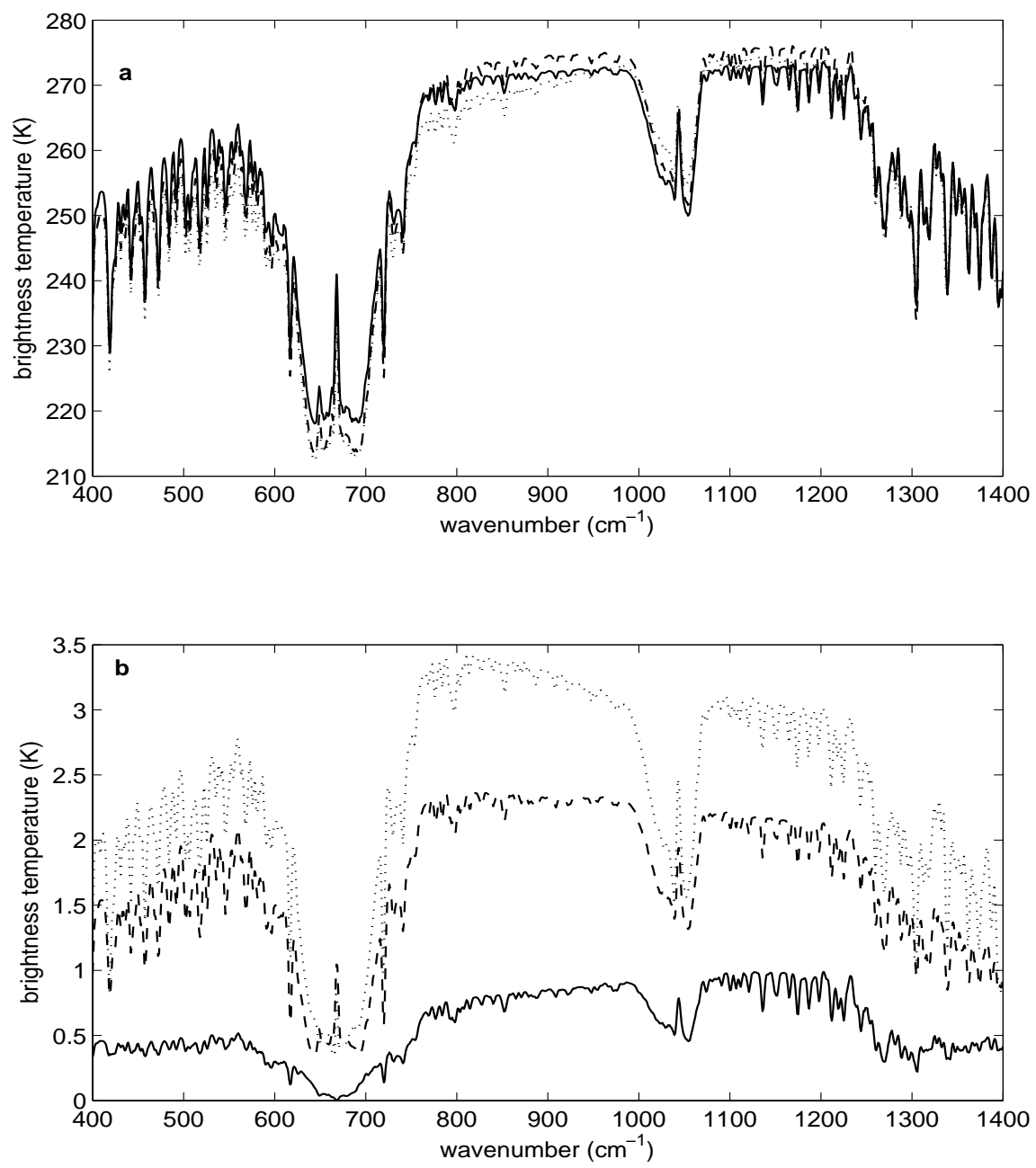


Figure 1.3 (a) The 10-month mean spectrum of the western Pacific over the IRIS period. The dotted line is from IRIS observation, the dash line is a synthetic spectrum based on NCAR CAM2 simulation, and the solid line is based on UCLA GCM simulation. (b) The standard deviations of the monthly average of IRIS spectra (the dotted line), synthetic spectra based on NCAR CAM2 simulation (the dash line), and synthetic spectra based on UCLA GCM (the solid line).

The comparison can be done in two ways. One is to invert vertical profiles from each individual spectrum, then compare them with modeled profiles. The other is to calculate synthetic spectra based on model outputs, then compare them with observed spectra. The equation describing the thermal infrared radiative transfer from surface to space is essentially a Fredholm equation of the first kind [Liou, 2002]. As long as the measurement is done at a finite number of spectral points, retrieving the temperature (gas concentration) profile from such an equation is an ill-posed problem even though the measurement is perfectly free of error and the gas concentration (temperature) profile is known *a priori*. Taking measurement uncertainty and the complexity of the scene (clear-sky, overcast, or partially cloudy) into account, the retrieval problem is even more difficult and sometimes the solution is not unique [Rodgers, 2000]. On the other hand, with the advance of radiative transfer knowledge and computer technology, forward simulation of spectra is fast and reliable. With today's computational power, generating millions of synthetic thermal infrared spectra with a resolution up to 1cm^{-1} can be done within one day using an ordinary workstation. Moreover, the radiative transfer algorithm can gain the maximum possible efficiency when it is parallelized. Putting all these factors together, calculation of synthetic spectra is a better choice than inversion of observed spectra.

The approach of generating synthetic radiance from GCM output and then comparing with observations has been used in pioneering work of Morecette [1991], Schmetz and Vandenberg [1994], and Soden and Bretherton [1994]. For example, Soden and Bretherton [1994] computed narrow-band averaged radiance over the water vapor $6.3\ \mu\text{m}$ band using clear-sky outputs from two GCMs, ECMWF and NCAR CCM, and

compared with GOES cloud-clearing observation. They showed that the discrepancies between ECMWF and the observations can be attributed to the underestimated strength of the large-scale circulation in the GCM while the discrepancies between NCAR CCM and observation are not simply correlated with features of the large-scale circulation. *Haskins et al.* [1997] compared various statistical properties of IRIS spectra and synthetic spectra based on a surrogate GCM simulation and demonstrated the discrepancies in the second- and higher-moment statistics between the model and IRIS. Due to the lack of access to the cloud data of the model, this work was also focused on clear-sky situations only. Given the prominent role played by cloud in the climate system, the big uncertainty of cloud forcing in GCMs [*Cess et al.*, 1995], and the potential of introducing sampling bias by any cloud clearance algorithm [*Soden and Bretherton*, 1994], we include both clear-sky and cloudy data in our studies presented in the following Chapter 2 and Chapter 3.

1.3.3 Using observations with a dense sampling pattern

For observations with a dense spatial sampling pattern like AIRS (2025 spectra per minute, covering an area of 1650km by 290km), there are two ways in which comparisons between model and observation can be done, focusing on testing different aspects of the model. One is to generate synthetic spectra based on the outputs from a GCM. This will test all aspects of the GCM, not only the subgrid parameterizations. The advantage of this approach is that parameterization schemes are tested as they are intended to be used. If the observation is not from a geostationary satellite, the under-sampling issue of the satellite has to be considered in order to make meaningful comparisons. One solution is to average over a certain area and a certain period from both

the GCM outputs and satellite data. An alternative approach is to implement the satellite's sampling pattern inside the GCM.

The second way to do such a comparison is to generate synthetic spectra based on the single-column model (SCM, the column-physics component of GCM) outputs while the large-scale advection terms are provided by numerical weather prediction or reanalysis data. SCM usually contains all physical subgrid parameterization schemes so that more emphasis can be put on testing parameterizations. The advantage of this approach is that SCM is computationally cheap. Compared with the popular way to test SCM against limited field observations like ARM [*Ghan et al.*, 2000], this approach can test over a variety of areas. So at least those parameters used in the parameterization schemes can be better “tuned” with respect to the different climate zones.

1.4 Summary

The singular importance of the outgoing thermal infrared spectra in the climate observations is due to the large amount of information about atmospheric thermodynamic variables and greenhouse gases contained in such measurements. As illustrated in Section 1.2, such measurements can be used to detect climate change caused by the increase of greenhouse gases as well as infer the “climate response spectrum.” It can be used also in testing the climate model, especially the model variability. Such tests would examine the variability of temperature, humidity, and cloud together. Given the information about the vertical profiles contained in the high spectral resolution measurements, it is unlikely that the model can have wrong variability at certain levels but yield a satisfactory agreement with observed spectra at all the spectral channels. In this sense, testing model variability

using the outgoing thermal infrared spectra is stricter than the traditional tests which use selected quantities from the standard model outputs.

The major disadvantage of using thermal infrared spectra in testing models is that the spectra contain information about the atmosphere in a complicated way, which makes interpreting test results not straightforward. But with the help of the spectral shape, the spatial maps or the time series associated with the spectra, as well as the retrieval, this difficulty can be at least partially overcome.

1.5 Acknowledgement

IRIS data and UCLA GCM simulation used in this study were kindly provided by L. Chen and J. Farrara, respectively. The computer resources for NCAR CAM2 run were kindly provided by NCAR Scientific Computing Division. The study presented in Section 1.2 was mentored by R.M. Goody and Y.L. Yung.

1.6 Appendix: Details of simulating IMG-IRIS difference

Figure 1.2 is based upon the following:

Radiation algorithm: These three panels have been calculated using MODTRAN 4.1 [Bernstein *et al.*, 1996]. An 8-stream discrete ordinate calculation was used for cloudy situation, and correlated-k for band absorption.

Data: Temperature profiles up to 10 mb and water vapor profiles up to 300 mb were obtained from the NCEP reanalysis data [Kalnay *et al.*, 1996]. Above 10 mb (300 mb), a typical tropical temperature (water vapor) profile [McClatchey *et al.*, 1972] is used. Concentrations of CO₂ are from Mauna Loa monthly meansⁱ, and the vertical profile is

ⁱ <http://www.cmdl.noaa.gov/ccgg/>

assumed to be uniform. Surface concentrations of CFC-11 and CFC-12 are from the same sourceⁱ as CO₂ with a linear extrapolation to the IRIS period. The vertical distributions of CFCs are from *Minschwaner et al.* [1993]. Surface concentration of CH₄ for the IMG winter is also from the Mauna Loa dataⁱ. For the IRIS winter, result from ice core measurements [*Etheridge et al.*, 1992] is used. The stratospheric ozone change is from *Randel et al.* [1999]; the tropospheric ozone change is from *Kim and Newchurch* [1996]. Changes of nitrous oxide surface concentration follow *Houghton et al.* [1996]. The vertical distributions of methane, nitrous oxide, and ozone are based on *McClatchey et al* [1972]. Changes of cloud amount are derived from the Extended Edited Cloud Report Archive (EECRA) [*Hahn and Warren*, 1999]. Using the procedure recommended by *Hahn and Warren* [1999], the frequency of occurrence for each type of cloud and the cloud amount when presents (AWP) are calculated. Although the EECRA is a sophisticated compilation of surface observations of clouds, large uncertainty might still exist. So the cloud information used here is only suggestive.

1.7 Reference

Bell, R. J., *Introductory Fourier Transform Spectroscopy*, Academic Press, San Diego, 1972.

Bell, T. L., Climate sensitivity from fluctuation dissipation: Some simple model tests, *Journal of the Atmospheric Sciences*, 37 (8), 1700-1707, 1980.

Bernstein, L. S., A. Berk, P. K. Acharya, D. C. Robertson, G. P. Anderson, J. H. Chetwynd, and L. M. Kimball, Very narrow band model calculations of

ⁱ <http://www.cmdl.noaa.gov/hats/index.html>

- atmospheric fluxes and cooling rates, *Journal of the Atmospheric Sciences*, 53 (20), 2887-2904, 1996.
- Block, L. C., and A. S. Zachor, Flight satellite measurements of infrared spectral radiance of the Earth, *Applied Optics*, 3 (2), 209-214, 1964.
- Boffetta, G., G. Lacorata, S. Musacchio, and A. Vulpiani, Relaxation of finite perturbations: Beyond the fluctuation-response relation, *Chaos*, 13 (3), 806-811, 2003.
- Brindley, H. E., and J. E. Harries, Observations of the infrared outgoing spectrum of the Earth from space: The effects of temporal and spatial sampling, *Journal of Climate*, 16 (22), 3820-3833, 2003.
- Cess, R. D., M. H. Zhang, P. Minnis, L. Corsetti, E. G. Dutton, B. W. Forgan, D. P. Garber, W. L. Gates, J. J. Hack, E. F. Harrison, X. Jing, J.T. Kiehl, C. N. Long, J. J. Morcrette, G. L. Potter, V. Ramanathan, B. Subasilar, C. H. Whitlock, D. F. Young, and Y. Zhou, Absorption of solar-radiation by clouds observations versus models, *Science*, 267 (5197), 496-499, 1995.
- Charlock, T. P., CO₂ induced climatic-change and spectral variations in the outgoing terrestrial infrared radiation, *Tellus Series B-Chemical and Physical Meteorology*, 36 (3), 139-148, 1984.
- Etheridge, D. M., G. I. Pearman, and P. J. Fraser, Changes in tropospheric methane between 1841 and 1978 from a high accumulation-rate Antarctic ice core, *Tellus Series B-Chemical and Physical Meteorology*, 44 (4), 282-294, 1992.
- Ghan, S., D. Randall, K. M. Xu, R. Cederwall, D. Cripe, J. Hack, S. Iacobellis, S. Klein, S. Krueger, U. Lohmann, J. Pedretti, A. Robock, L. Rotstajn, R. Somerville, G.

- Stenchikov, Y. Sud, G. Walker, S. C. Xie, J. Yio, and M. H. Zhang, A comparison of single column model simulations of summertime midlatitude continental convection, *Journal of Geophysical Research-Atmospheres*, 105 (D2), 2091-2124, 2000.
- Goody, R., J. Anderson, and G. North, Testing climate models: An approach, *Bulletin of the American Meteorological Society*, 79 (11), 2541-2549, 1998.
- Hahn, C. J., and S. G. Warren, Extended Edited Cloud Reports from Ships and Land Stations over the Globe, 1952-1996, pp. 79, Carbon Dioxide Information Analysis Center (CDIAC), Department of Energy, Oak Ridge, Tennessee, 1999.
- Hanel, R. A., V., Salomons, G. Wolford, I. Revah, Prabhaka.C, V.G. Kunde, and B.J. Conrath, Nimbus-4 infrared spectroscopy experiment .1. Calibrated thermal emission-spectra, *Journal of Geophysical Research*, 77 (15), 2629-2641, 1972.
- Hanel, R. A., Schlachm B., F. D. Clark, C. H. Prokesh, J. B. Taylor, W. M. Wilson, and L. Chaney, Nimbus-III Michelson interferometer, *Applied Optics*, 9 (8), 1767-1774, 1970.
- Hanel, R. A., Schlachm B. , D. Rogers, and D. Vanous, Nimbus-4 Michelson interferometer, *Applied Optics*, 10 (6), 1376-1382, 1971.
- Harries, J. E., H. E. Brindley, P. J. Sagoo, and R. J. Bantges, Increases in greenhouse forcing inferred from the outgoing longwave radiation spectra of the Earth in 1970 and 1997, *Nature*, 410 (6826), 355-357, 2001.
- Haskins, R. D., R. M. Goody, and L. Chen, A statistical method for testing a general circulation model with spectrally resolved satellite data, *Journal of Geophysical Research-Atmospheres*, 102 (D14), 16563-16581, 1997.

- Houghton, J. T., *Climate change: the IPCC scientific assessment*, 364 pp., Cambridge University Press, New York, 1990.
- Houghton, J.T., *Climate change 1995: the science of climate change*, 572 pp., Cambridge University Press, New York, 1996.
- Houghton, J. T., *Climate change 2001: the scientific basis*, 881 pp., Cambridge University Press, New York, 2001.
- Iacono, M. J., and S. A. Clough, Application of infrared interferometer spectrometer clear sky spectral radiance to investigations of climate variability, *Journal of Geophysical Research-Atmospheres*, 101 (D23), 29439-29460, 1996.
- Kalnay, E., M. Kanamitsu, R. Kistler, W. Collins, D. Deaven, L. Gandin, M. Iredell, S. Saha, G. White, J. Woollen, Y. Zhu, M. Chelliah, W. Ebisuzaki, W. Higgins, J. Janowiak, K.C. Mo, C. Ropelewski, J. Wang, A. Leetmaa, R. Reynolds, R. Jenne, and D. Joseph, The NCEP/NCAR 40-year reanalysis project, *Bulletin of the American Meteorological Society*, 77 (3), 437-471, 1996.
- Keith, D. W., and J. G. Anderson, Accurate spectrally resolved infrared radiance observation from space: Implications for the detection of decade-to-century- scale climatic change, *Journal of Climate*, 14 (5), 979-990, 2001.
- Kiehl, J. T., Satellite detection of effects due to increased atmospheric carbon-dioxide, *Science*, 222 (4623), 504-506, 1983.
- Kim, J. H., and M. J. Newchurch, Climatology and trends of tropospheric ozone over the eastern Pacific Ocean: The influences of biomass burning and tropospheric dynamics, *Geophysical Research Letters*, 23 (25), 3723-3726, 1996.

- Kobayashi, H., A. Shimota, C. Yoshigahara, I. Yoshida, Y. Uehara, and K. Kondo, Satellite-borne high-resolution FTIR for lower atmosphere sounding and its evaluation, *IEEE Transactions on Geoscience and Remote Sensing*, 37 (3), 1496-1507, 1999.
- Leith, C. E., Climate response and fluctuation dissipation, *Journal of the Atmospheric Sciences*, 32 (10), 2022-2026, 1975.
- Liou, K. N., Remote sensing using emitted infrared radiation, in *An introduction to atmospheric radiation*, pp. 388, Academic Press, San Diego, 2002.
- Lovett, J., L. Marcotte, and R. Nadile, *Report AFCRL-67-0563*, Office of Aerospace Res., USAF, 1967.
- Mertz, L., in *Proc. 12th Intern. Astrophys. Symp.*, p. 120, Gov. Res. Rep., U.S. Dept. of Commerce, Rep. No. AD602963, 1963.
- McClatchey, R. A., R. W. Fenn, J. E. A. Selby, P. E. Volz, and J. S. Garing, *Optical Properties of the Atmosphere*, 3d ed., pp. 113, Air Force Cambridge Research Laboratory, 1972.
- Minschwaner, K., R. J. Salawitch, and M. B. McElroy, Absorption of solar-radiation by O₂ - Implications for O₃ and lifetimes of N₂O, CF₄, and CFC₂, *Journal of Geophysical Research-Atmospheres*, 98 (D6), 10543-10561, 1993.
- Morcrette, J. J., Evaluation of model-generated cloudiness: Satellite-observed and Model-generated diurnal variability of brightness temperature, *Monthly Weather Review*, 119 (5), 1205-1224, 1991.
- North, G. R., R. E. Bell, and J. W. Hardin, Fluctuation dissipation in a General-Circulation Model, *Climate Dynamics*, 8 (6), 259-264, 1993.

- Randel, W. J., and F. Wu, A stratospheric ozone trends data set for global modeling studies, *Geophysical Research Letters*, 26 (20), 3089-3092, 1999.
- Rodgers, C. D., *Inverse method for atmospheric sounding: theory and practice*, 238 pp., World Scientific, Singapore, 2000.
- Soden, B. J., and F. P. Bretherton, Evaluation of water-vapor distribution in General-Circulation Models using satellite-observations, *Journal of Geophysical Research-Atmospheres*, 99 (D1), 1187-1210, 1994.
- Spankuch, D., and W. Dohler, Radiative properties of cirrus clouds in the middle IR derived from Fourier spectrometer measurements from space, *Zeitschrift Fur Meteorologie*, 35 (6), 314-324, 1985.
- Schmetz, J., and L. Vandenberg, Upper-tropospheric humidity observations from Meteosat compared with short-term forecast fields, *Geophysical Research Letters*, 21 (7), 573-576, 1994.

Chapter 2: Temporal Variability of the Thermal IR Spectra Seen from IRIS Data and GCM Simulations

Part of the material in this chapter was published in

Huang, X., J. Farrara, S. S. Leroy, Y. L. Yung, and R. M. Goody, Cloud variability as revealed in outgoing infrared spectra: Comparing model to observation with spectral EOF analysis, *Geophys. Res. Lett.*, 29(8), 1270, doi:10.1029/2001GL014176, 2002.

2.1 Abstract

In order to evaluate how well current GCMs can simulate the temporal variability seen from the IRIS observations, we apply spectral empirical orthogonal function (EOF) analysis to IRIS data and synthetic spectra based on the simulations from two GCMs (UCLA GCM and NCAR CAM2). We show that proper averaging over a correct timescale is necessary. We focus on two tropical Pacific regions (the central Pacific and the western Pacific) and two midlatitude Pacific regions (the northern Pacific and the southern Pacific). For all regions examined here, the first *principal component* (PC1) is the dominant contributor to the total variance and the PC1s from two GCMs show substantial discrepancies from the PC1s from IRIS. The PC1s from two GCMs do not agree with each other either. At two tropics regions, cloud can explain most variance seen in the PC1s. The discrepancies seen from the PC1s at these two regions are insensitive to the parameterizations of cloud optical properties and cloud fraction. The discrepancies at the western (central) Pacific are most likely caused by the deficiency in simulating the intraseasonal (seasonal) variation of the Walker Circulation.

At two midlatitude regions, both the stratospheric and the tropospheric variations can be seen from the PC1s but two GCMs significantly underestimate the variations in the stratosphere. Using a retrieval scheme, we show that the differences between the modeled PC1s and the IRIS PC1s is closely related to how well models can simulate the variations of low clouds, boundary layer temperatures, and stratospheric temperatures.

2.2 Data and methodology

IRIS data used in this study have already been introduced in Section 1.2. Two GCMs, the radiative transfer model, and the spectral EOF analysis used in this study are to be introduced here. The sampling issue is also addressed in this section.

2.2.1 GCMs

The two GCMs used here are UCLA GCM 7.0 and NCAR CAM2. The major characteristics and the parameterization schemes of the two GCMs, which are related to this study, are summarized in Table 2.1. It can be seen that the two models are different in many aspects. Particularly, several differences that need noticing are

- (1) CAM2 has many more layers near the tropopause than UCLA GCM.
- (2) The instantaneous cloud fraction over a grid box in CAM2 is diagnostically calculated based on relative humidity, vertical velocity and other variables. It can be any number between 0 and 1. In UCLA GCM it is either 0 or 1, depending on a threshold value of cloud water mixing ratio.
- (3) The ice cloud effective radius in CAM2 is parameterized as a function of ambient pressure. In UCLA GCM, the ice cloud effective radius is uniformly set as 75 μm . The maritime liquid cloud effective radius is set as constant (10 μm) in both GCMs. CAM2 parameterizes the continental liquid cloud effective radius as a function of ambient temperature and UCLA GCM still uses 10 μm as the liquid cloud effective radius over continents.

	UCLA GCM	CAM 2.0
Numerical approach	Finite difference	Spectral method
Horizontal resolution	4°×5°	2.8°×2.8° (T42)
Vertical resolution	15 layers (modified σ coordinate)	26 layers (hybrid coordinate)
Radiation scheme	<i>Harshvardhan et al.</i> [1989]	<i>Collins et al.</i> [2002], <i>Collins</i> [2001]
Cloud scheme	<i>Harshvardhan et al.</i> [1989] <i>Kohler</i> [1999]	<i>Rasch and Kristjansson</i> [1998] <i>Zhang et al.</i> [2003]
Cumulus convection scheme	<i>Arakawa and Schubert</i> [1974] <i>Cheng and Arakawa</i> [1997]	<i>Zhang and MacFarlane</i> [1995]

Table 2.1 The major features of two GCMs used in this study and the parameterization schemes of two GCMs pertinent to this study.

2.2.2 MODTRAN

The radiative transfer model used in this study to generate IRIS-like spectra is Moderate Transmittance Code (MODTRAN) v4.1 developed by Air Force Geophysical Lab [*Bernstein et al.*, 1996; *Wang et al.*, 1996]. It adopted a very-narrow band model approach to generate a spectrum at a fixed sampling interval of 1.0 cm⁻¹. It was designed to be efficient, user friendly, downward compatible, flexible in handling various scene geometries and various cloud/aerosol configurations. It has a fast two-stream algorithm and a more accurate DISORT algorithm to handle the multiple scattering. Given the fact that tens of millions of spectra have to be calculated and DISORT is a very time-consuming approach, we have to adopt a two-stream algorithm in the presence of cloud. In detail, twice-per-day outputs of temperature, humidity, and cloud profiles were generated from each GCM's simulation forced by the realistic monthly mean of sea surface temperature (SST) over the IRIS period. Then these outputs were fed into MODTRAN to generate IRIS-like spectra. More discussion about the feasibility of using MODTRAN in such a study can be found at *Haskins et al.* [1997].

2.2.3 The spectral EOF analysis

The statistical technique used here is principal component analysis [Hotelling, 1933] in the spectral domain, so-called spectral EOF analysis. Let $I_\nu(x)$ be a set of radiances, where ν is frequency and x is either time or space. The EOFs, $\phi_\nu^{(i)}$, are unit eigenvectors of the covariance matrix defined by

$$C_{\nu_1\nu_2} = \overline{(I_{\nu_1}(x) - \bar{I}_{\nu_1})(I_{\nu_2}(x) - \bar{I}_{\nu_2})} \quad (2.1)$$

where the overbars represent averaging over all samples in the given set. Let λ_i be the eigenvalue corresponding to the i^{th} eigenvector $\phi_\nu^{(i)}$ and $\lambda_i \geq \lambda_{i+1}$; then the *principal component* (PC) is defined as¹

$$PC_\nu^{(i)} = \sqrt{\lambda_i} \phi_\nu^{(i)} \quad (2.2)$$

The fraction of variance explained by the i^{th} eigenvector is $\lambda_i / \sum \lambda_i$. With this definition, PCs have the dimensions of radiance and therefore can be more easily interpreted than EOFs [Haskins *et al.*, 1999]. The normalized *expansion coefficient* (EC) of the i^{th} PC is

$$EC_i(x) = \sum_\nu [I_\nu(x) - \bar{I}_\nu(x)] \phi_\nu^{(i)} / \sqrt{\lambda_i} \quad (2.3)$$

With this definition, the standard deviation of the EC is 1 and the mean is 0. If x is space (time), then ECs can be interpreted as the spatial (temporal) patterns associated with the corresponding PCs. One thing to note is that each *principal component* is forced to be orthogonal to its all predecessors. As a result, the higher-order *principal components* might not be amenable to simple physical interpretations because linear independence is

¹ There is no consistent terminology for EOF analysis. The terms used by different communities could even contradict each other [Preisendorfer, 1988]. Here, we adopt these definitions to be consistent with previous works on spectral EOF studies [Haskins *et al.*, 1999].

equivalent to statistical independence only when the probability distribution of the variable is Gaussian.

The application of principal component analysis in satellite radiance sounding was pioneered by Smith and Woolf [1976]. Besides using it to study the variability of the infrared spectra [Haskins *et al.*, 1999], recent applications include compression and retrieval of hyper-spectral sounding data [Goldberg *et al.*, 2003; Huang and Antonelli, 2001], detection of cloud in high-resolution infrared spectra [Smith and Taylor, 2004], as well as analysis of solar irradiance spectra [Rabbette and Pilewskie, 2001].

2.2.4 Sampling issue: temporal and spatial average and diurnal variability

Before we can carry out our spectral EOF analysis, we need to average the spectra over certain regions and timescales. This is necessary because the spatial and temporal sampling patterns of observations are not the same as those in the model. In this study, we focus on four regions: two in the tropics, the central Pacific (180°W to 130°W, 10°S to 10°N) and the western Pacific (90°E to 150°E, 10°S to 10°N); two in the midlatitudes, the northern Pacific (180°W to 130°W, 45°N to 60°N) and the southern Pacific (180°W to 130°W, 60°S to 45°S). The appropriate timescale for the averaging is discussed in the next paragraph. For IRIS data, the number of spectra collected during the ascending node is usually different from those collected during the descending node due to the quality control. Before we average the data, we weight data from the ascending branch and from the descending branch such that day-night contrasts are eliminated.

We are forced to choose a temporal averaging window suitably long to reduce complications arising from under-sampling by IRIS, a problem typical of any sounder sensitive to clouds [Salby, 1989]. The asynoptic nature of a sun-synchronous satellite is

especially important for clouds because the space and time scales of cloud variability are easily less than that of the sampling. *Salby* [1989] pointed out that clouds change typically in hours, which is much shorter than the time for the globe to be covered by the satellite and that a sufficiently long period averaging can remove the aliasing from unresolved random variability. We estimate the timescale to do the average with synthetic spectra based on GCM output. We use two different methods to get the daily average over a given region. One is to do the average with all grid points inside this region (hereafter, “average-all” method), the other is to find the grid points nearest to the satellite tracks and average spectra only at those grid points (hereafter, “track-orbit” method). Obviously, the latter method is more directly suitable for comparison to IRIS spectra. With these two methods, we obtain the averages over periods longer than one day. When the averaging is done over a long enough timescale, the difference of two sets of averaged spectra should be very small, demonstrating that the “track-orbit” method is already a good approximation to the “average-all” method at this timescale. Figure 2.1 shows a comparison of the standard deviation of these two sets of spectra over the central Pacific. It can be seen that for 5-day averaging the standard deviation from the “average-all” method is only half of that from the “track-orbit” method; when the averaging period is 25 days, they are almost the same. Therefore, for the central Pacific, we adopt 25-day averages. We apply the same analysis to the western Pacific and it shows that 25 days is again long enough for discrepancies in the standard deviation to cancel.

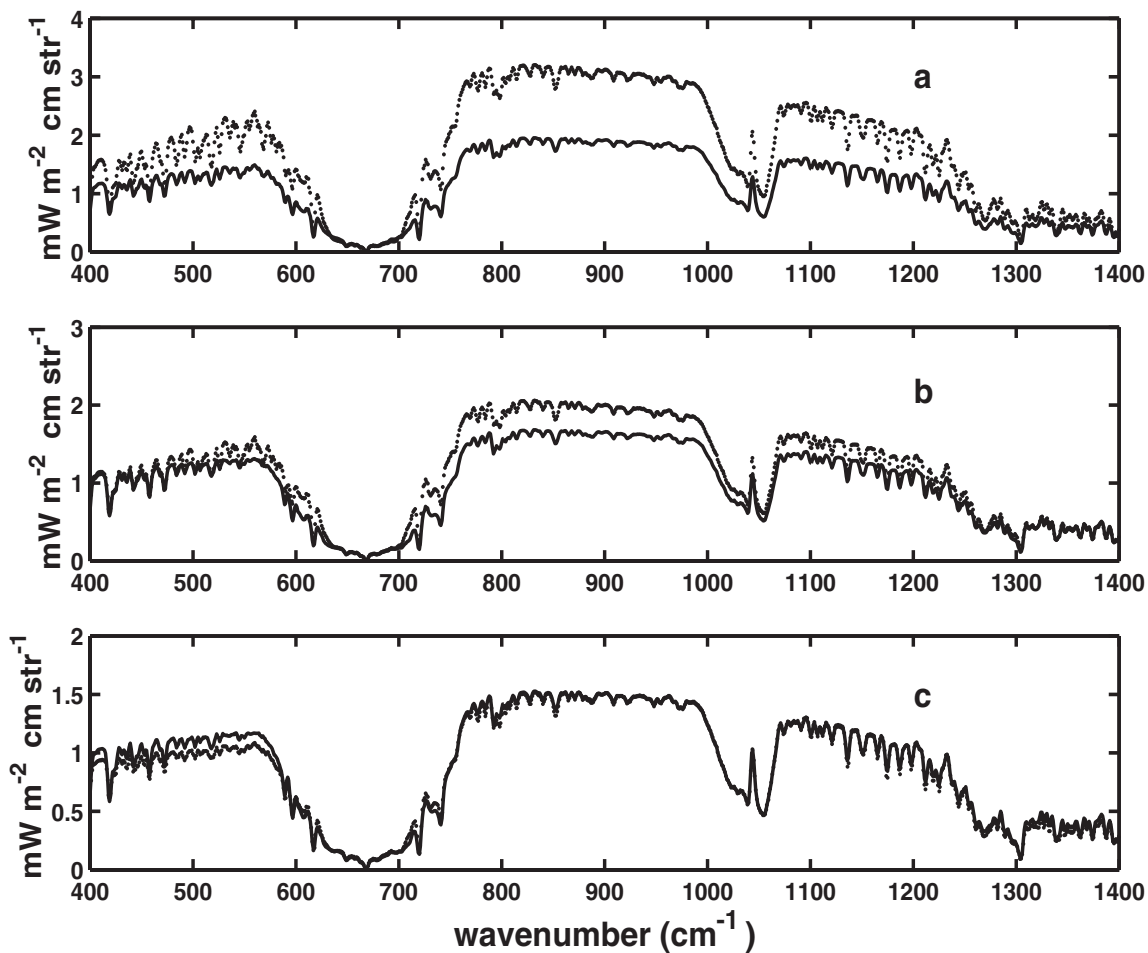


Figure 2.1 (a) The standard deviation of spectrally resolved radiance derived from the UCLA GCM. The dotted line was computed from data averaged over 5 days for the Central Pacific using the ‘track-orbit’ method (as defined in the text). The solid line is the same as the dashed line, except that the averaging was performed using the ‘average-all’ method (as defined in the text). (b) Same as (a), except that the time interval for averaging is 20 days. (c) Same as (a), except that the averaging time is 25 days.

Other than random fluctuations which can be smoothed out by averaging over a long period, there is another kind of temporal variability which we must take into account: diurnal variability. IRIS always sampled around local noon and midnight, but the GCMs gave output at 1200 and 0000 GMT. So we need to investigate to what extent the two different time-sampling patterns affect the spectral EOF analysis. To tackle this issue, we do a simple test. We assume the cloud diurnal variations are sinusoidal, $C(t) = C_0 + C_a \sin[2\pi(t - T_m)/24]$, where C_0 is a constant term, and $0 \leq t \leq 24$ hour. The phase information for different kinds of cloud is obtained from the study about diurnal variations of cloud cover by *Bergman and Salby* [1996]: for low cloud, $T_m \approx -2$; for high cloud, $T_m \approx 11$. Based on this sinusoidal curve, we can interpolate GCM cloud output to local noon and midnight. With these new cloud data, we can calculate spectra and do spectral EOF analysis. It turns out that the first *principal component* (PC1) obtained from this analysis is only slightly different from the original PC1. Other studies [*Bergman and Salby*, 1996; *Bergman and Salby*, 1997] also showed that diurnal variations of cloud over tropical ocean regions are weaker than those over landmasses, and the cloud diurnal contributions to the time-mean thermal flux are usually less than 1 W m^{-2} . Therefore, we conclude that the different phases of diurnal variation sampled by IRIS and the GCMs could not have important impact on the substantial differences found between the observed PCs and the simulated PC1.

2.3 The tropical cases

This section presents the results over the central Pacific and the western Pacific. The focus is the first *principal component* (PC1) and its interpretation because the PC1s can explain more than 92% of the total variance for all the cases. One thing to note is that

UCLA GCM does not have a realistic variability in the tropical stratosphere, partially because (1) the difficulty of avoiding spurious reflection of upward-propagating waves in a model with a rigid upper boundary at 50km [Callaghan *et al.*, 1999] (2) the 6-layer representation of the stratosphere in the model might not be enough for a satisfactory simulation of the stratospheric variability. Given the fact that the PC1s are due to the variations in the troposphere (details in the following Section 2.3.1), for UCLA GCM output we replace the temperature and humidity profiles above 50mb with the typical tropical profiles provided by MODTRAN. By doing this, we eliminate the variability above 50mb in UCLA GCM outputs and focus on the tropospheric variations.

2.3.1 Results from spectral EOF analysis and simple interpretation

Figure 2.2(a) shows the mean spectra over the central Pacific from April to December of 1970 obtained from IRIS data and synthetic spectra based on UCLA GCM and CAM2 simulations, respectively. The good agreements between IRIS and CAM2 mean spectra at the CO₂ 667 cm⁻¹ band indicate that CAM2 can simulate the 9-month mean temperature profiles in the stratosphere quite well. The large discrepancies between IRIS and two GCMs at the window regions reveal that neither GCMs can simulate the cloud mean state satisfactorily. For the western Pacific case shown in Figure 2.2(b), the agreement between IRIS and GCMs is better than for the central Pacific case although there are still discrepancies at the window regions.

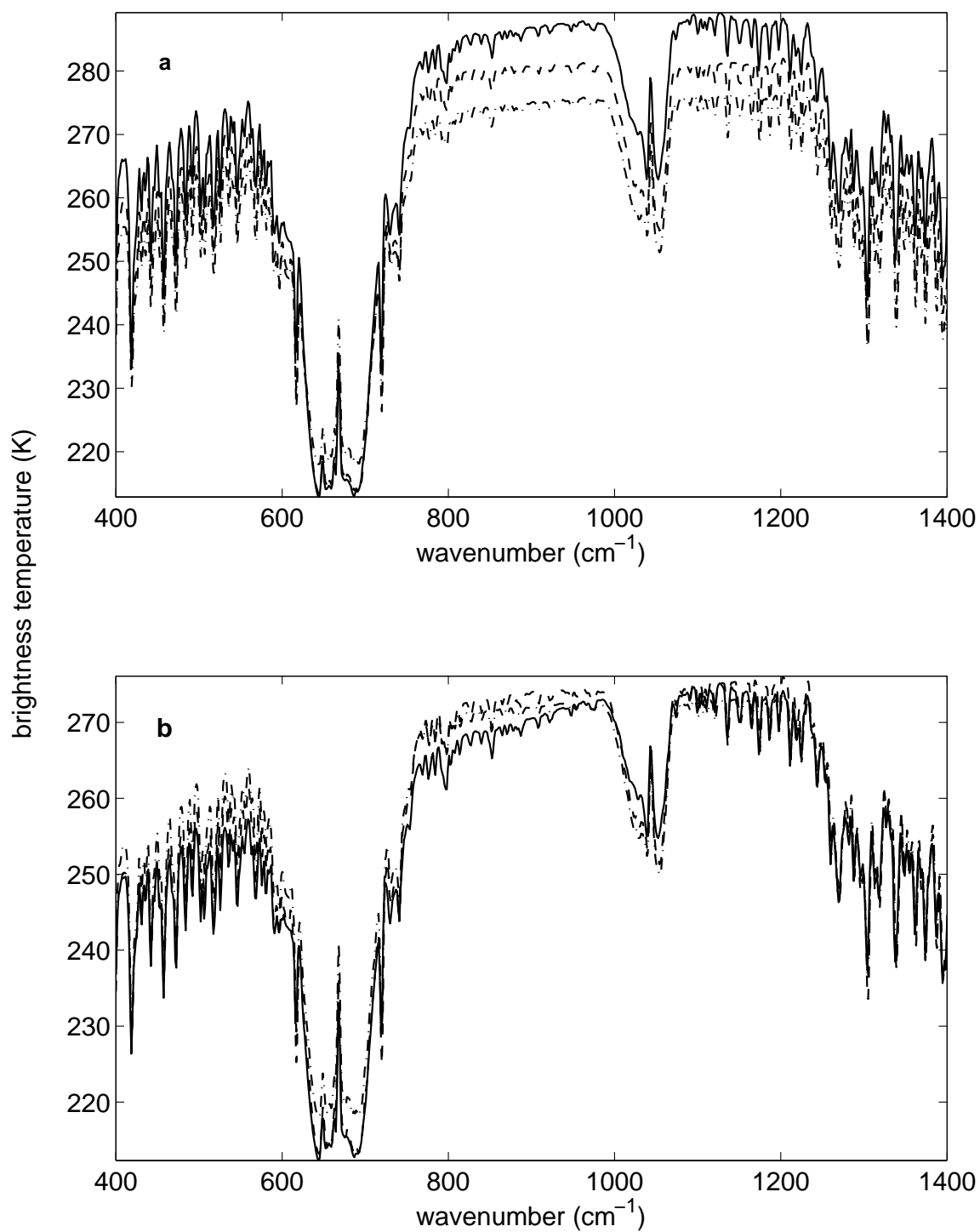


Figure 2.2 (a) The mean spectra over the central Pacific from April to December of 1970 observed by IRIS (the solid line), simulated by CAM2 (the dash line) and UCLA GCM (the dash-dotted line). (b) Same as (a) except over the western Pacific.

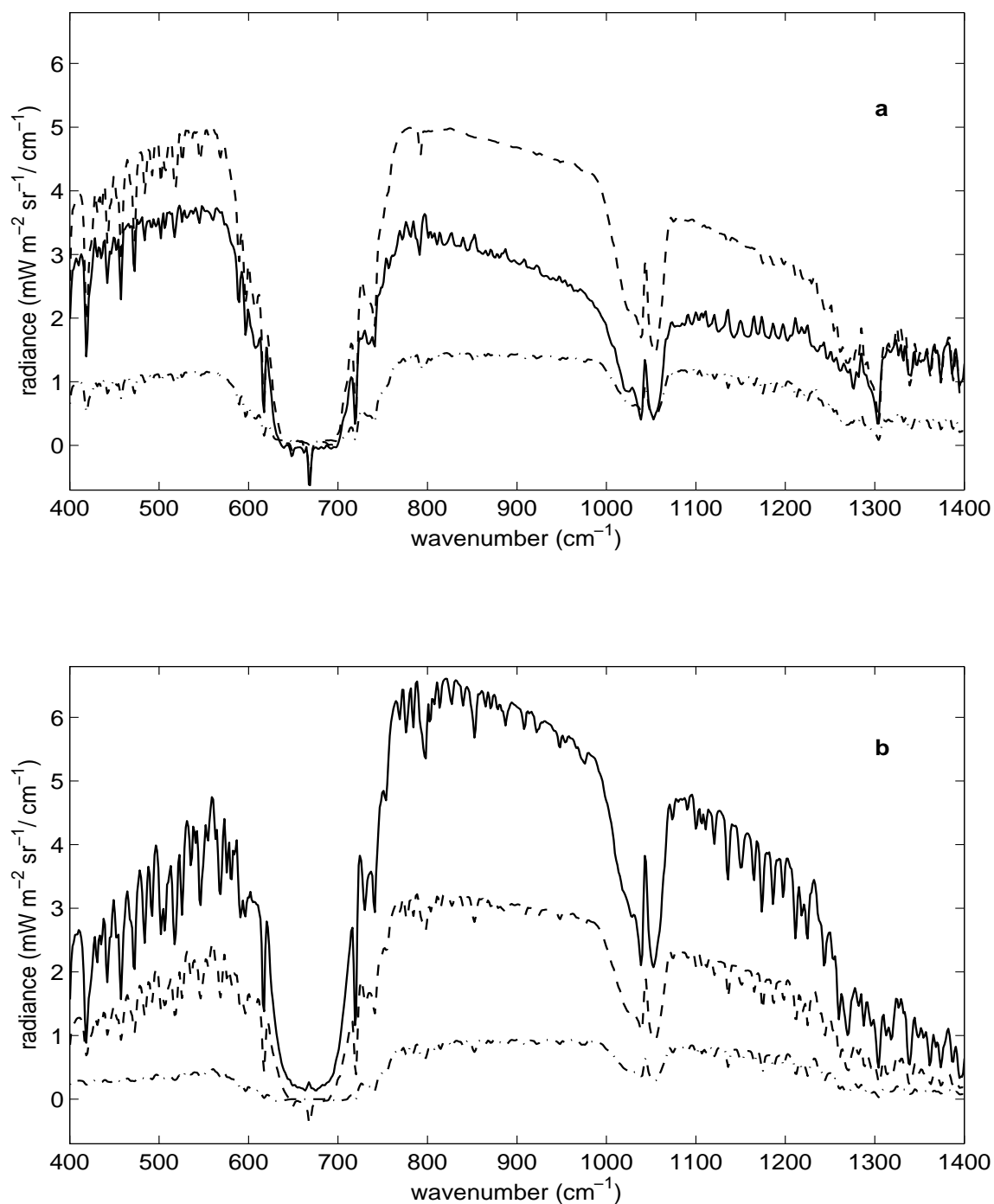


Figure 2.3 (a) The first *principal component* (PC1) over the central Pacific derived from 25-day averaged spectra of IRIS (the solid line), from CAM2 (the dash line) and UCLA GCM (the dash-dotted line) simulations. (b) Same as (a), but over the western Pacific.

	The central Pacific			The western Pacific		
	IRIS	UCLA	CAM2	IRIS	UCLA	CAM2
Variance explained by the PC1	98.0%	98.0%	99.5%	99.1%	92.7%	97.5%
Corresponding ΔBT in the window regions (K)	2.4	1.1	4.2	4.8	0.6	2.0
Integration ($W m^{-2} sr^{-1}$)	2.1	0.9	3.1	3.4	0.5	1.7
Variance explained by cloud (%)	75	94	93	98	96	98
Corresponding cloud fraction change (%)	2.95 (± 0.13)	1.62 (± 0.03)	4.82 (± 0.10)	8.39 (± 0.09)	1.60 (± 0.03)	3.67 (± 0.06)
Corresponding cloud height	16km	10km	16km	8km	10km	6km

Table 2.2 Properties of the PC1s of IRIS and the two GCMs. ΔBT is the change of brightness temperature. Variance explained by cloud, corresponding cloud fraction change, and corresponding cloud height are based on a stepwise regression algorithm [Haskin *et al.*, 1999]. The error bars in parentheses correspond to 95% significance.

The PC1s derived from IRIS and the two GCMs over the central Pacific and the western Pacific are presented in Figure 2.3. Properties of the PC1s are summarized in Table 2.2. The most obvious difference between PC1s from IRIS and PC1s from models is the amplitude. Compared with IRIS, UCLA GCM substantially underestimates the amplitudes of the PC1s over both the central Pacific (by a factor of ~ 2) and the western Pacific (by a factor of ~ 6). CAM2, however, overestimates the amplitude over the central Pacific (by a factor of ~ 1.5) and underestimates that over the western Pacific (by a factor of ~ 2).

We apply a simple inversion scheme to explore the contribution of clouds to the PC1s. The detailed description of this scheme can be found in Haskins *et al.* [1999]. Simply put, stepwise regression is applied to each PC1 to determine the cloud contributions. There are seven types of clouds in this scheme, the tops of which are

located at 2, 4, 6, 8, 10, 12 and 16 km, respectively. For each PC1, the amount of variance that can be explained by clouds is listed in Table 2.2. Except for the IRIS PC1 over the Central Pacific, clouds can explain more than 92% of variance of the PC1 in all the other cases. The corresponding cloud height and cloud fraction change derived from this inversion scheme are also listed in Table 2.2. The results suggest that contributors to PC1s are most likely the high clouds rather than the low clouds. For UCLA GCM, its cloud fraction changes are smaller than the counterparts of IRIS over both the central Pacific and the western Pacific. For CAM2, it has larger cloud fraction change and higher cloud height than IRIS over the central Pacific and the situation is the opposite over the western Pacific. The result from this simple inversion scheme is qualitative, but clearly shows that the major contribution to PC1 is cloud and that both models have deficiencies in getting the cloud variability correct.

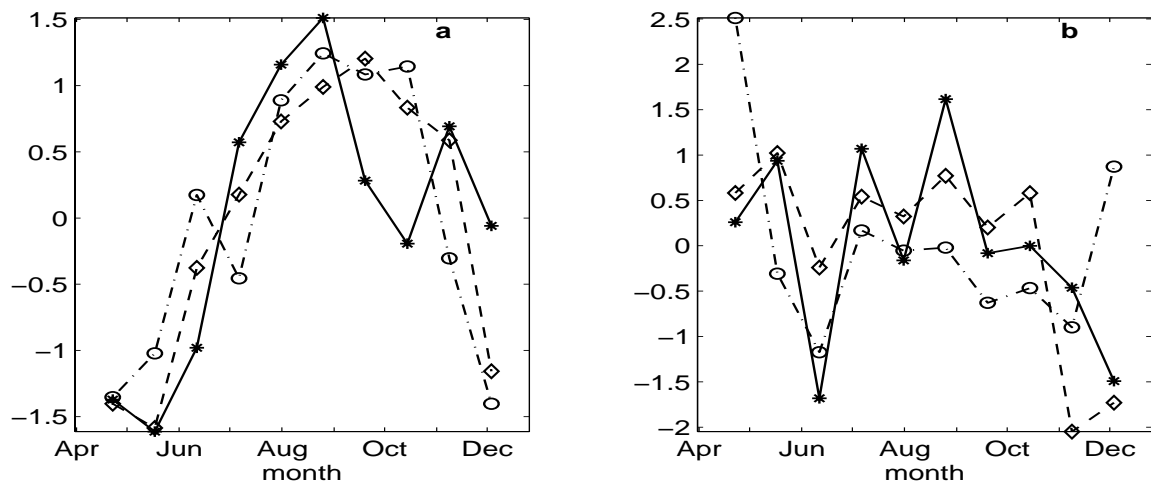


Figure 2.4 (a) The PC1 time series over the central Pacific derived from IRIS (the solid line with stars), CAM2 output (the dash line with diamonds), and UCLA GCM output (the dash-dotted line with circles). (b) Same as (a) except over the western Pacific.

	The central Pacific	The western Pacific
CAM2	0.80 (99%)	0.68 (97%)
UCLA GCM	0.59 (93%)	0.17 (35%)

Table 2.3 The correlation coefficients between the PC1 time series from each GCM and those from IRIS. The numbers in parentheses are the significance derived from zero-hypothesis test.

The time series of these PC1s are shown in Figure 2.4. The correlation coefficients between the PC1 time series from each model and those from IRIS are listed in Table 2.3. For the central Pacific (Figure 2.4a), the PC1s basically show the seasonal variability. Given the dominant contribution of cloud to these PC1s, it can be concluded that the PC1s over the central Pacific essentially capture the cloud seasonal variability. Both GCMs can capture the temporal variation reasonably well.

For the western Pacific (Figure 2.4b), the IRIS time series oscillates at the timescale of around 50 days, the same timescale as intraseasonal oscillation (also known as MJO). A typical cycle of MJO begins with low surface pressure and convergence in the Indian Ocean building convection. Then the low surface pressure and convection will move and spread eastward and, after 7~15 days, arrive at its time-average position, the western Pacific. At this step, the Walker Circulation reaches a relative maximum. Then the convection system will keep moving eastward to 180°W and weaken and disappear over the cold equatorial sea surface [Madden and Julian, 1971; Madden and Julian, 1994]. Therefore, it is conceivable that MJO has a large effect on the variability of the outgoing infrared spectra over the western Pacific. The IRIS PC1 time series is well correlated with the CAM2 PC1 time series but the correlation is not very significant (Table 2.3). The correlation between IRIS and UCLA GCM is poor and not significant at

all. Moreover, from Figure 2.4b it can be seen that the IRIS PC1 time series oscillates with a much larger amplitude than those of the two models (all time series are normalized to have unitary standard deviation). This is consistent with the fact that currently no GCMs can do a realistic simulation of MJO, which is at least partially due to the insufficient representation of mesoscale convection system in the GCMs. One thing to note is that Randall et al. [2003] recently demonstrates the robust simulation of MJO with superparameterizations, coupling a cloud resolving model with a GCM.

2.3.2 Insensitivity of the spectral EOF results to the parameterizations of the cloud effective radius and cloudiness

In the previous subsection, we identify cloud variability as the major contribution to the PC1s. In both GCMs, cloud optical depth is parameterized as a function of cloud water path (CWP) and the effective radius of cloud particles (r_e). In CAM2, other cloud optical properties, such as single scattering albedo and asymmetric factor, are also parameterized as functions of r_e . In UCLA GCM, these optical properties are constant for liquid water cloud and ice cloud, respectively. Nevertheless, as pointed out in Section 2.2, r_e of continental liquid water cloud in CAM2 is parameterized as a function of temperature and r_e of maritime liquid water cloud is 10 μm everywhere; r_e of ice cloud in CAM2 is parameterized as a function of pressure. In UCLA GCM, r_e is 75 μm for ice cloud and 10 μm for liquid water cloud everywhere. On the other hand, UCLA GCM does not parameterize instantaneous cloud fraction (“binary cloud”, either overcast or clear-sky) but CAM2 does parameterize it. Intuitively, it seems that both fixed r_e and binary cloud can contribute to the unrealistic small variability seen from the PC1s of UCLA GCM. But to what extent they contribute to the discrepancies between the UCLA

GCM and CAM2 PC1s is not self-evident. This subsection will address the effects of these different parameterizations used by the two GCMs on the PC1s.

We rerun CAM2 with the cloud effective radii fixed in the same ways as they are in UCLA GCM. By doing this, other cloud optical properties except the cloud optical depth are fixed too. The PC1 from this experiment is plotted in Figure 2.5 (the dash-dotted line). It can be seen that the difference between this PC1 and the original CAM2 PC1 is rather small: the maximal difference in the window region is about 2%. This demonstrates that the different ways to parameterize r_e could not explain the big difference between the PC1s from two models. It alone could not account for the discrepancies between the modeled and observed PC1s either. Recent studies showed that the parameterization of r_e does have a significant impact on the temporal variability of radiative fluxes over a single grid box [*Jacobellis et al.*, 2003; *McFarquhar et al.*, 2003]. Here, our results show that, after the heavy average over space and time, the variability of these mean spectra is not sensitive to the way that r_e is parameterized.

Due to the complexity of GCM, fully replacing the cloud fraction parameterization in CAM2 with the one used in UCLA GCM is beyond the scope of this study. However, to a large extent, the impact of binary cloud on the PC1 can be estimated in this way: (1) set a clear-sky criterion (CLRCRI), (2) at any given time, if the instantaneous clear-sky fraction over a grid box is larger than CLRCRI, the grid box is classified as a clear-sky box and the spectrum over this grid box is calculated with clear sky configuration only; if the instantaneous clear-sky fraction is smaller than this criterion, the grid box is treated as overcast and the spectrum is calculated with cloud configuration only. We try two values for CLRCRI, 0.7 and 0.9, respectively. The PC1s

calculated from these two estimations are presented in Figure 2.5. As expected, the PC1s from binary cloud configurations have smaller amplitude than the original one. But the difference is little: the maximal difference is about 5% for CLRCRI = 0.7 and 8% for CLRCRI = 0.9. This indicates that the different ways of parameterizing cloud fraction between UCLA GCM and CAM2 should not be a major reason for the discrepancies shown in the PC1s. In fact, whether instantaneous cloud fraction should be parameterized or not is still under debates [Kohler, 1999]. The reason why UCLA, as well as some other GCMs, simply uses binary cloud parameterization is that the monthly-averaged cloud fraction simulated from such GCMs still has reasonably good agreements with observations.

2.3.3 Further interpretation

Subsection 2.3.2 excludes cloud effective radius and cloud fraction as the major contributors to the discrepancies shown in the modeled and observed PC1s. Given the fact that the PC1s are mostly due to the variation of cloud, the other candidates would be:

- (1) Cloud water path (CWP). In both models, a prognostic cloud bulk microphysical scheme is used to predict CWP. Both the water vapor in the large-scale field and the water provided by the convection are closely related to the CWP. The schemes used in two models are similar, both rooted from cloud resolving models. It is highly unlikely that the two schemes would yield very different results if the input large-scale variables and the tendency of water from convection scheme are the same.
- (2) Cloud top height and cloud top temperature. For the optically thick clouds, if the variations of the cloud top height (temperature) are different between

models and observations, they can easily make discrepancies in the PC1s. The cloud top height and the cloud top temperature are closely related to the large-scale variables (for stratified clouds) and the convection (for convective clouds).

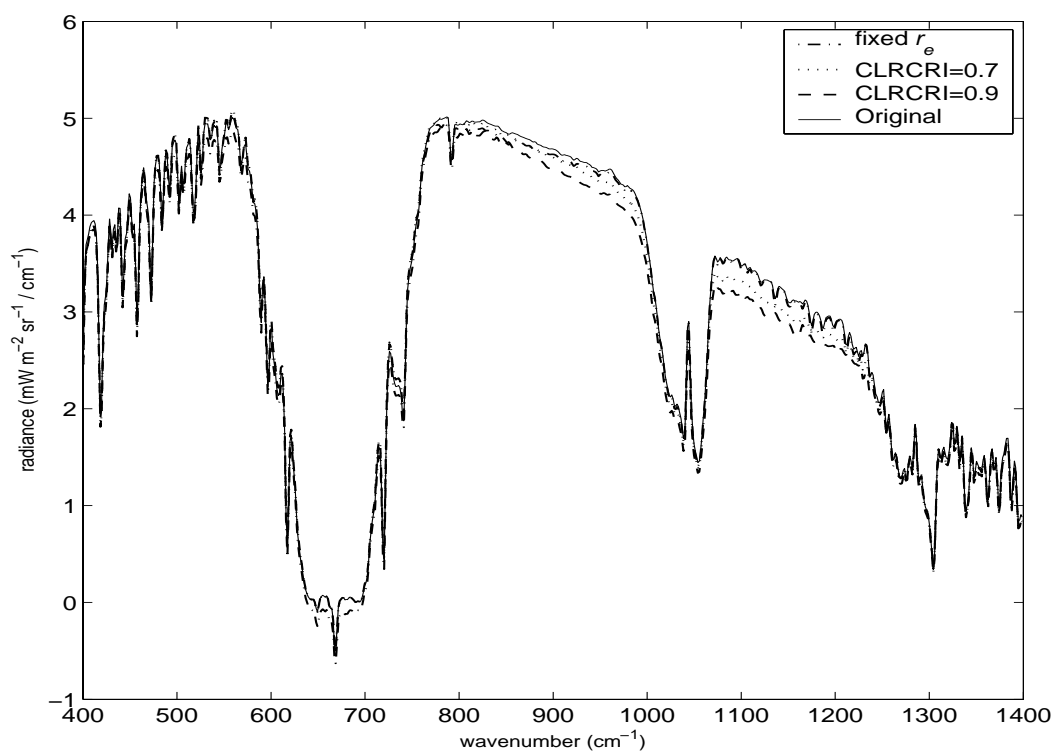


Figure 2.5 The PC1s at the central Pacific based on the output of the original CAM2 run (the solid line), the CAM2 run with fixed r_e (the dash-dotted line), the calculation using CLRCRI=0.7 (the dotted line) and CLRCRI=0.9 (the dash line).

With these considerations, the big discrepancies seen in Figure 2.3 are more likely due to the difference between the observed variability of large-scale circulation and the simulated counterpart and how well convection has been represented in the models. The circulation pattern dominant over the western Pacific and the central Pacific is the Walker Circulation driven by atmospheric heating processes [Bjerknes, 1969; Webster, 1983]. The major ascending branch of the Walker Circulation is over the western Pacific and maritime continent. The seasonal variation can shift the center of the ascending branch from around 100°E (January) to 150°E (July). The descending usually happens in the broad region of the eastern Pacific (150-90°W in January and 120-90°W in July) [Lau and Yang, 2003]. The seasonal variation of the Walker Circulation is modulated by MJO and the ENSO. El Nino events usually weaken the Walker Circulation with rising motion over the central and eastern Pacific while La Nina events usually enhance the Walker Circulation with well-defined ascending and descending branches.

Given that 1970-1971 is a moderate La Nina year, most part of the central Pacific (10°S-10°N, 180-130°W) should be within the descending branches. Occasionally the west side of it can be at the margin of the large-scale convective region (e.g., in a MJO cycle, convection system can move east to around 180°W). The major types of clouds in this region should be anvil clouds detached from convective cells and low clouds formed in the descending branches. The cloud variations in this region should be closely related to the variations of the strength of the Walker Circulation. The western Pacific (10°S-10°N, 90-150°E) is within the ascending branches almost all the time. So the convective clouds are the major types of cloud in the western Pacific. Therefore, both the convection and the Walker Circulation strength can have impact on the cloud variability in the

western Pacific. Given the nature of the Walker Circulation, how well convection can be simulated is closely related to the realistic simulation of the Walker Circulation. Therefore, a realistic simulation of convection variability is essential here to reduce the discrepancies between the modeled and the simulated PC1s.

Substantially underestimated variance in the tropics by GCM has been noted in previous studies. For example, Ricciardulli and Garcia [*Ricciardulli and Garcia, 2000*] used 3-hourly brightness temperature measurements at 11 μm as a proxy for deep convection activity and compared this proxy with simulated deep convection in NCAR CCM3, the predecessor of CAM2. They demonstrated that although the mean state simulated by CCM3 is similar to the observed one, the simulated variance is much less than the observed one. Part of the reason for such discrepancies is rooted in the way that convection is parameterized in GCMs: when the convection is parameterized in term of grid-level variables, the model implicitly assumes that the unresolved convection can be expressed in a sense of ensemble mean. Variability associated with convection activities cannot be represented by the ensemble mean but it effectively acts as a stochastic noise so it might have effects on grid-level variables as well. Recently several studies [*Lin and Neelin, 2002; Lin and Neelin, 2003; Naveau and Moncrieff, 2003*] showed that including the subgrid-scale convection variability in models by stochastic parameterization can significantly affect the variability at the intraseasonal or even longer time scale.

Yet the convection parameterization scheme cannot explain the unrealistic large amplitude of the CAM2 PC1 over the central Pacific. It would be instructive to compare the simulated (observed) cloud properties over the IRIS period with those derived from

the control run¹ (climatology) to see how well CAM2 can simulate the response of the cloud seasonal cycle to the interannual variation of SST. But unfortunately IRIS was early in the satellite era that no sophisticated observations about cloud during the IRIS period are available. Instead, we choose April 1988 to January 1989 as a surrogate period because this period had the similar phases of both seasonal cycle and ENSO as the IRIS period [Haskins *et al.*, 1997]. The ISCCP D2 data product over this surrogate period and the ISCCP D2 climatology are used as observational datasets². The comparisons are summarized in Table 2.4. Over the central Pacific, the variations of monthly-average cloud amount during the ISCCP surrogate period are larger than those from ISCCP climatology. CAM2 also has larger cloud variations during the IRIS period than its control run (fixed SST climatology). But the cloud variations in CAM2 are systematically larger than those of ISCCP. This indicates that CAM2 overestimates the mean seasonal variation of cloud over the central Pacific, which contributes partially to the discrepancies in the PC1s shown in Figure 2.3a. Over the western Pacific, the cloud variations derived from the CAM2 control run are also larger than those from ISCCP climatology. But the observed cloud variations during the surrogate period are larger than the climatological cloud variations while CAM2 produces smaller cloud variations during the IRIS period than the control run. So for the western Pacific not only is the mean seasonal variation not realistically simulated in CAM2, but also the simulated changes of the seasonal cycle with respect to the interannual SST variation are opposite to the observed changes derived from ISCCP.

¹ Control run refers to the run forced with climatological SST.

² ISCCP (International Satellite Cloud Climatology Project) is a project to retrieve cloud product from various satellite radiance measurements [Rossow, *W.B.*, and *R.A. Schiffer*, 1999], spanning from July 1983 to December 1999.

		CAM control run	CAM2 04/1970- 01/1971	ISCCP Climatology	ISCCP 04/1988 - 01/1989
The central Pacific	High cloud fraction	6.9%	9.6%	3.6%	3.9%
	Total cloud fraction	7.9%	10.0%	3.5%	5.9%
The western Pacific	High cloud fraction	5.6%	3.4%	4.0%	7.8%
	Total cloud fraction	5.9%	3.4%	3.4%	6.0%

Table 2.4 The standard deviations of monthly-averaged total cloud amount and high cloud amount derived from ISCCP products and CAM2 simulations.

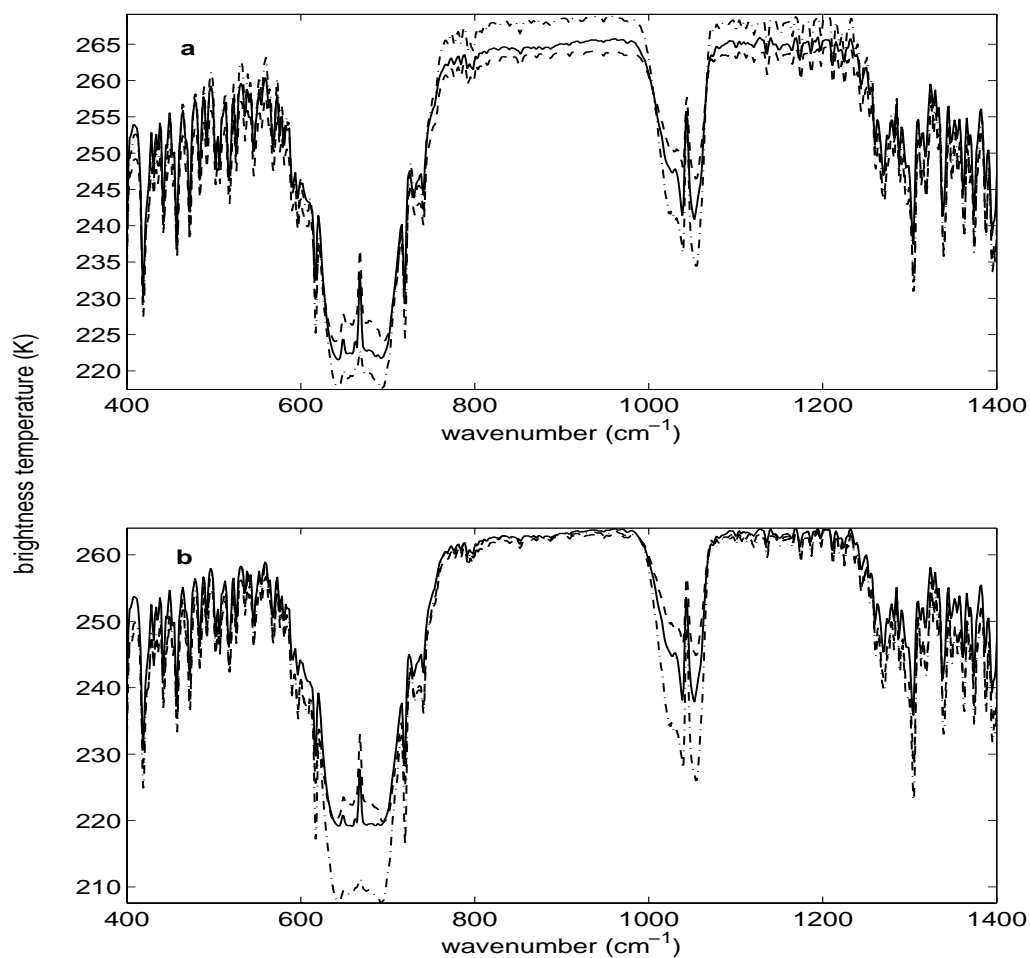


Figure 2.6 (a) The mean spectrum over the northern Pacific from April 1970 to December 1970 derived from IRIS observation (the solid line), computed based on CAM2 simulation (the dash line) and UCLA GCM simulation (the dash-dotted line). (b) Same as (a) except over the southern Pacific.

2.4 The midlatitude cases

This section describes the spectral EOF results over two midlatitude oceanic regions, the northern Pacific and the southern Pacific. Unlike the tropical cases in which the stratospheric variation is not important to the PC1s, the stratospheric temperature variations have clear imprints on the PC1s of the midlatitude cases. Given this fact, the stratospheric profiles simulated by UCLA GCM are used in computing individual spectra.

Figure 2.6 shows the mean spectra over the northern Pacific and the southern Pacific from IRIS observation and the two models. The CO_2 667cm^{-1} band shows that, for both regions, UCLA GCM has a colder stratosphere than IRIS while the stratosphere in CAM2 is slightly warmer than that of IRIS. At the window region, the UCLA GCM mean spectrum over the northern Pacific is higher than the IRIS counterpart by about 5K, indicating that on the onverage UCLA GCM has less cloud or lower cloud top than the IRIS observation. The CAM2 mean spectrum over the northern Pacific is slightly lower than the IRIS counterpart by about 1.5K at the window region. The mean spectra over the southern Pacific from the two GCMs agree very well with the IRIS counterpart at the window region.

2.4.1 Results from the spectral EOF analysis

Figure 2.7 plots the PC1s over the two regions derived from IRIS and two models. The fractions of variance explained by each PC1 and PC2 are listed in Table 2.5. Both UCLA GCM and CAM2 overestimate the fractions of variance explained by the PC1 at these two regions. For the PC1s over the northern Pacific shown in Figure 2.7a, the most striking difference is the mismatch of the spectral shapes at the CO_2 667 cm^{-1} band between IRIS and UCLA GCM. IRIS PC1 shows a sharp spike at the center of this CO_2

band center while UCLA GCM only has a small bump there. In the midlatitudes, the typical CO₂ spatial variation in the stratosphere is ~ 1.5 ppmv [Olsen and Randerson, 2004], which can only produce a change less than $0.1 \text{ mW m}^{-2} \text{ sr}^{-1} / \text{cm}^{-1}$ at the CO₂ 667cm^{-1} band. Therefore, as Haskins *et al.* [1999] correctly pointed out the sharp spike of IRIS PC1 is clearly due to the variation of the stratospheric temperature. The CAM2 PC1 is similar to IRIS PC1 in terms of the spectral shape but with a smaller spike at the CO₂ 667 cm^{-1} band. For the PC1 over the southern Pacific shown in Figure 2.7b, the sharp spectral features at the CO₂ 667 cm^{-1} band and two neighboring hot bands indicate the temperature variations in the stratosphere and the upper troposphere. The PC1s from both models underestimate the peaks at the CO₂ 667 cm^{-1} band.

But at the window region, the UCLA PC1s have larger amplitude than IRIS PC1s by a factor 1.5~2 over both the northern Pacific and the southern Pacific. This is opposite to the tropical cases where the UCLA PC1s have much smaller amplitudes at the window region than the IRIS PC1s. The CAM2 PC1 has larger (smaller) amplitude than the IRIS PC1 over the northern (southern) Pacific. For the PC1s over the southern Pacific, the small amplitude at the water vapor band indicates little contribution from the tropospheric water vapor.

The time series of each PC1 is shown in Figure 2.8, and the correlation coefficients are summarized in Table 2.6. Apparently for both the models and IRIS, the PC1 time series basically shows the seasonal cycle. As indicated by Figure 2.8 and the correlation coefficients shown in Table 2.6, both models can capture the phase changes of the seasonal cycle reasonably well.

The IRIS PC1 over the northern Pacific shows a different spectral shape from the IRIS PC1 over the southern Pacific. This difference can be understood in terms of the seasonal variations of cloud and temperature. The standard deviations of 25-day averaged temperatures at different pressure levels from NCEP reanalysis [Kalnay *et al.*, 1996] are shown in Figure 2.9. The near-surface temperature variations over the northern Pacific are larger than those over the southern Pacific, primarily due to the large land-ocean contrast in the northern midlatitudes. Marine stratus is the dominant cloud observed in these two areas [Klein and Hartmann, 1993]. Such cloud usually tops around 1km, which makes the thermal contrast between surface and cloud top small. Based on the new ISCCP D2 data, the standard deviation of monthly-averaged stratus amount is ~4% over the northern Pacific and 1.3% over the southern Pacific. Therefore, both the near-surface temperature variations and the stratus variations favor a bigger variability over the northern Pacific rather than over the southern Pacific. This explains the difference seen at the window region of the PC1s of the two areas. Figure 2.9 also shows that the stratospheric temperature variation over the southern Pacific is more pronounced than that over the northern Pacific. This explains why the IRIS PC1 over the southern Pacific has a larger spike at the CO₂ 667 cm⁻¹ band center than the IRIS PC1 over the northern Pacific.

In summary, over both areas, PC1s from IRIS and CAM2 capture the seasonal cycle of the stratospheric and near-surface temperature (low cloud top temperature). The PC1 over the northern Pacific from UCLA GCM captures little contribution from the stratosphere. The surface temperature and low cloud amount over the northern Pacific have larger variation than the counterparts over the southern Pacific, which is captured at

the window regions of the IRIS PC1s. For both areas, UCLA GCM overestimates the variability at the window regions. CAM2 overestimates (underestimates) the variability at the window regions over the northern (southern) Pacific.

	The northern Pacific		The southern Pacific	
	PC1	PC2	PC1	PC2
IRIS	87%	12%	65%	33%
CAM2	93%	6%	79%	18%
UCLA	97%	2.7%	97%	2.5%

Table 2.5 The percentage of the total variance explained by the PC1s and the PC2s over the northern Pacific and the southern Pacific.

	The northern Pacific	The southern Pacific
CAM2	0.77 (99%)	0.89 (99%)
UCLA GCM	0.90 (99%)	0.67 (97%)

Table 2.6 The correlation coefficients between the PC1 time series from each GCM and those from IRIS. The number in parenthesis is the significance derived from zero-hypothesis test.

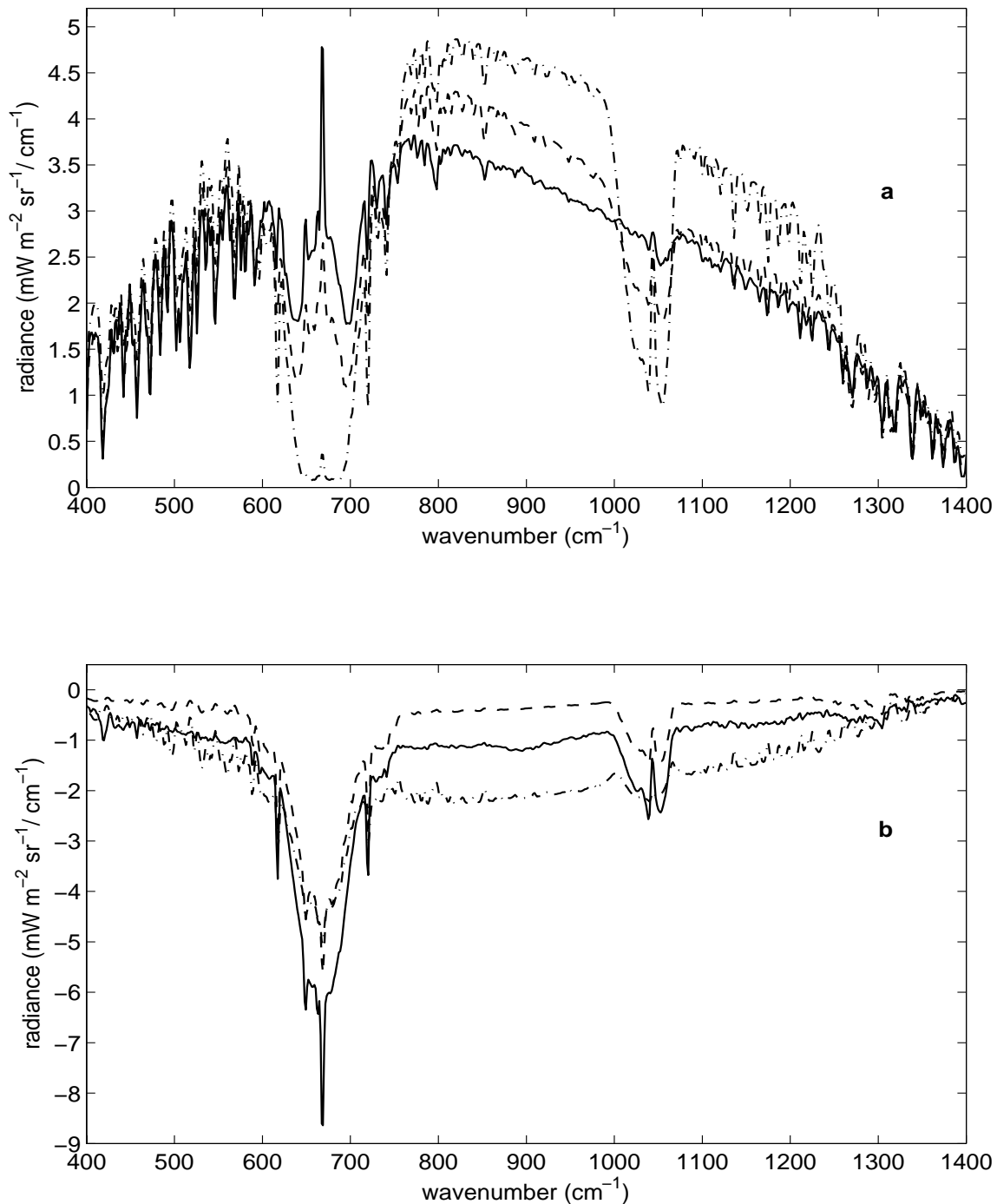


Figure 2.7. (a) The PC1 over the northern Pacific derived from 25-day averaged IRIS spectra (the solid line), from CAM2 (the dash line) and UCLA GCM (the dash-dotted line) simulations. (b) Same as (a) except over the western Pacific.

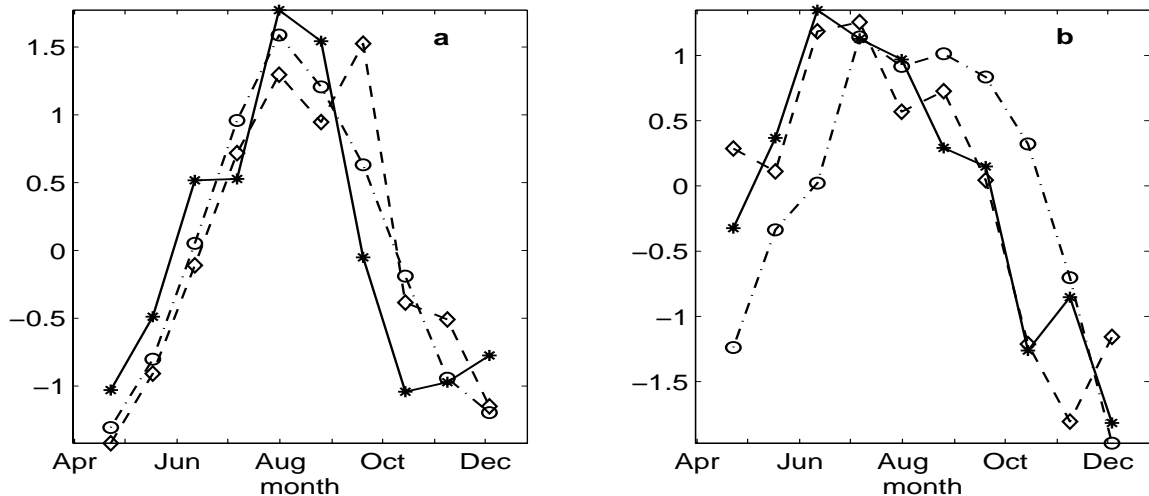


Figure 2.8 (a) The PC1 time series over the northern Pacific derived from IRIS (the solid line with star), CAM2 output (the dash line with diamond), UCLA GCM output (the dash-dotted line with circle). (b) Same as (a) except over the southern Pacific.

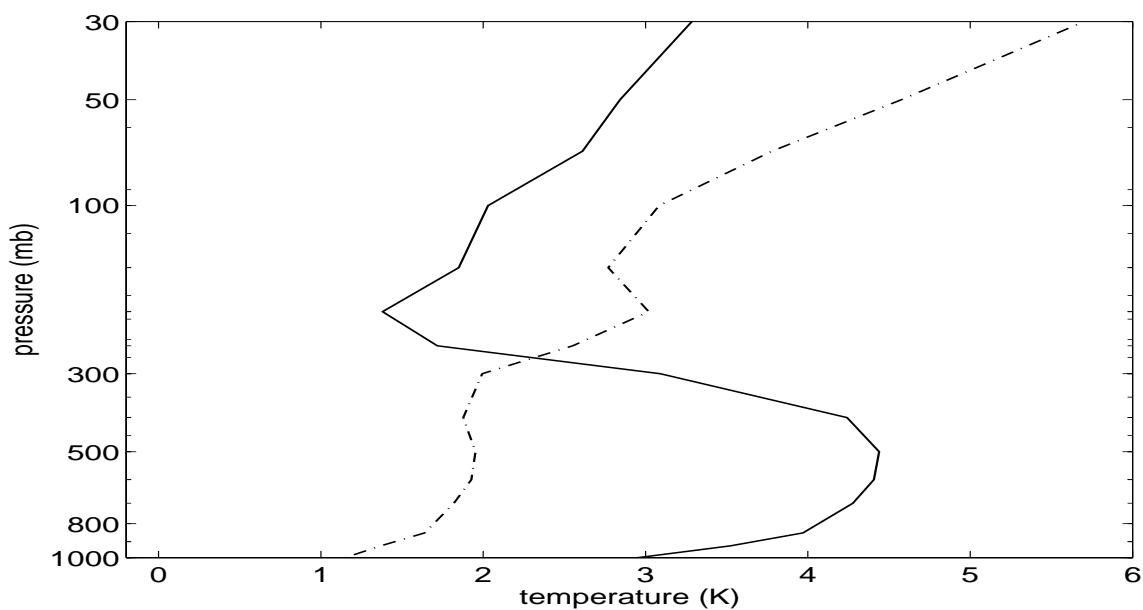


Figure 2.9 The standard deviations of 25-day averaged temperatures profiles over the northern Pacific (the solid line) and the southern Pacific (the dash line). The data are from NCEP reanalysis daily product.

2.4.2 Retrieval of PC1s

To quantitatively understand the causes of the PC1s shown in Figure 2.7, we use a retrieval algorithm to retrieve the temperature, humidity and cloud profiles from the PC1s. The retrieval algorithm is described in the appendix. The retrieved profiles are presented in Figure 2.10 (for the northern Pacific) and Figure 2.11 (for the southern Pacific).

Over the northern Pacific, the change of skin temperature retrieved from the PC1 of UCLA GCM is larger than that retrieved from the IRIS PC1 by 2.3K (out of 1σ uncertainty). The changes of skin temperature retrieved from the IRIS PC1 and the CAM PC1 are close to each other. In the free troposphere, the temperature changes retrieved from three PC1s are similar to each other. Retrieval from CAM2 PC1 shows a negative temperature change (~ 4 K) in the lower stratosphere while the UCLA PC1 and the IRIS PC1 show little temperature change there. Temperature changes above 50mb retrieved from the UCLA PC1 are significantly smaller than those from the IRIS PC1 and the CAM2 PC1. At 20mb, the retrieved temperature change from the UCLA PC1 is only 1K while it is around 8K from IRIS PC1 and CAM PC1. This explains the absence of a spike at the CO_2 667 cm^{-1} band in the PC1 of UCLA GCM. Above 10mb the temperature changes retrieved from the CAM PC1 are only half of those from the IRIS PC1, which explains why the CAM PC1 has a smaller spike at the CO_2 667 cm^{-1} band than the IRIS PC1. The low cloud change retrieved from the CAM (UCLA) PC1 is larger (smaller) than that from the IRIS PC1. There are discrepancies in retrieved tropospheric water vapor profiles too, but the uncertainty associated with IRIS retrieval is so large (especially in the low troposphere where cloud is present) that the retrieved water vapor profiles from the simulated PC1s are both within the uncertainty range.

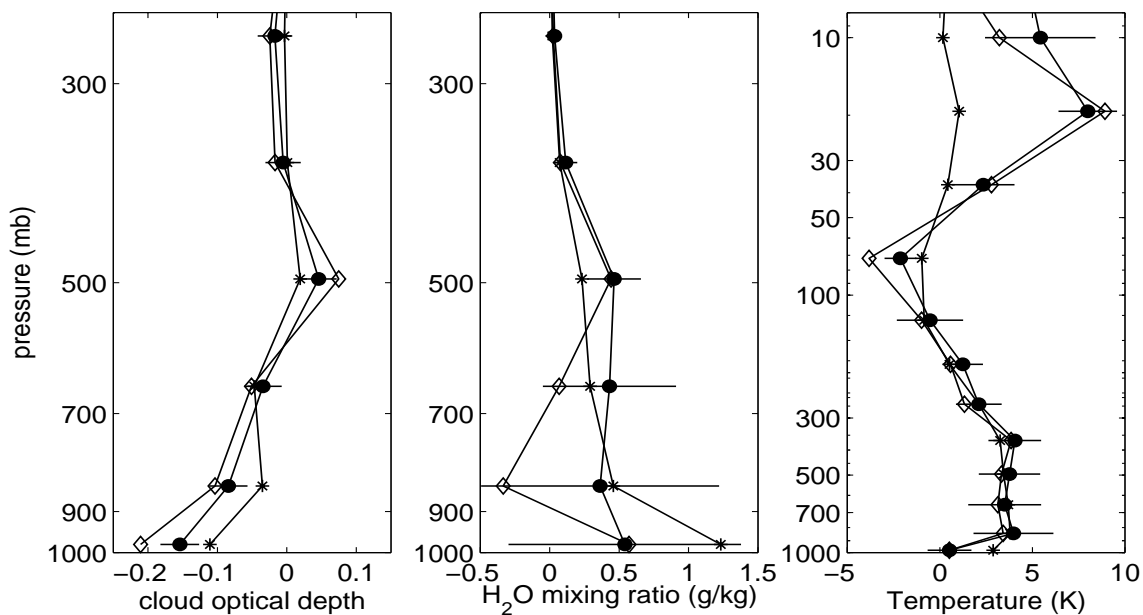


Figure 2.10 Retrieved profiles from the PC1s over the northern Pacific. The lines with filled circles are from the IRIS PC1, the lines with open diamonds from the CAM PC1, and the lines with stars from the UCLA PC1. Horizontal solid lines show the 1σ uncertainty of retrieved IRIS profiles.

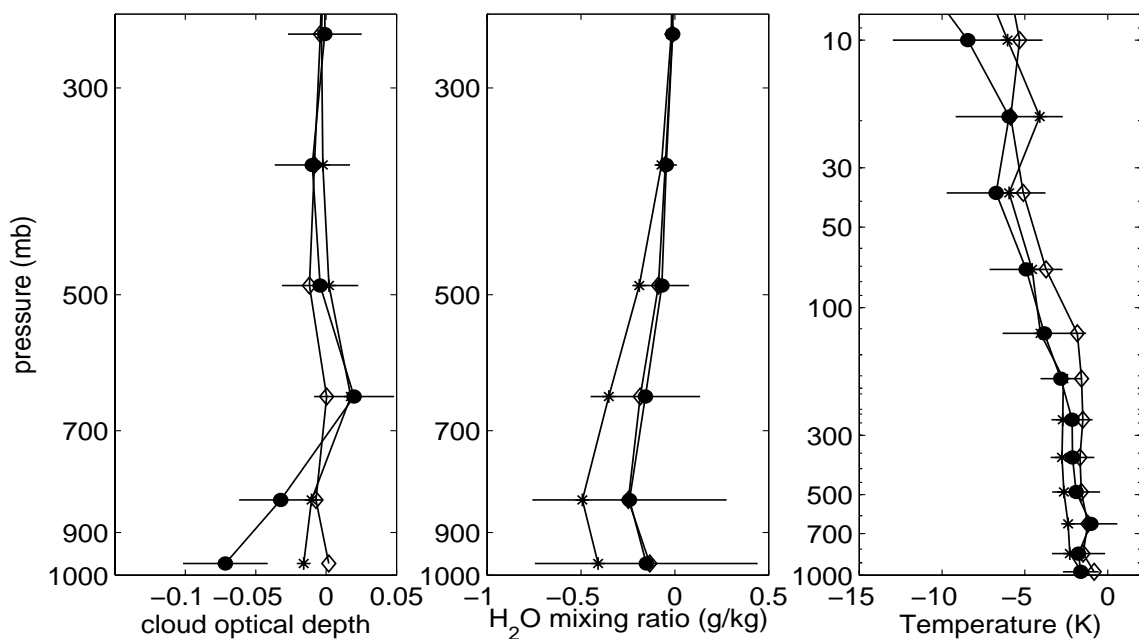


Figure 2.11 Same as Figure 2.10 except over the southern Pacific.

Over the southern Pacific, the changes of skin temperature retrieved from the UCLA PC1 and the IRIS PC1 are similar to each other and a little bit larger than that from the CAM PC1. The lower tropospheric temperature changes retrieved from the UCLA PC1 are systematically larger than those from the IRIS PC1, although the differences are still within 1σ retrieval uncertainty. Retrieved middle stratospheric temperature changes from the IRIS PC1 are larger than those from the UCLA PC1 and the CAM2 PC1, consistent with the sharper peak of the IRIS PC1 at the CO_2 667 cm^{-1} band compared to the modeled PC1s. Similar to the case of the northern Pacific, there is a significant difference in the retrieved low cloud optical depth between IRIS and two models. The retrieved humidity changes from the IRIS PC1 still associate with large uncertainty, but one thing to note is the good agreements between the humidity profiles retrieved from the CAM and IRIS PC1s.

Figure 2.12 shows the retrieved upper tropospheric water vapor changes from PC1s over two areas. Over the northern Pacific, the retrieved changes between 300mb and 100mb from the UCLA PC1 are systematically smaller than those from the IRIS PC1. The discrepancies are significant (out of 1σ uncertainty range) at all levels except 265mb where the difference between UCLA GCM and IRIS is a little bit smaller than the uncertainty. The changes of the upper tropospheric water vapor retrieved from the CAM2 PC1 over both areas are similar to those from the IRIS PC1.

The results presented here show that the discernible difference between the models and IRIS can be found from the retrieval of the PC1s. Although the two GCMs both overestimate the variations in the window region over the northern Pacific, retrieval shows that they might have different causes. The overestimation in UCLA GCM is more

likely due to the change of near-surface temperature and the overestimation in CAM2 is more likely due to the change of the low-cloud optical depth.

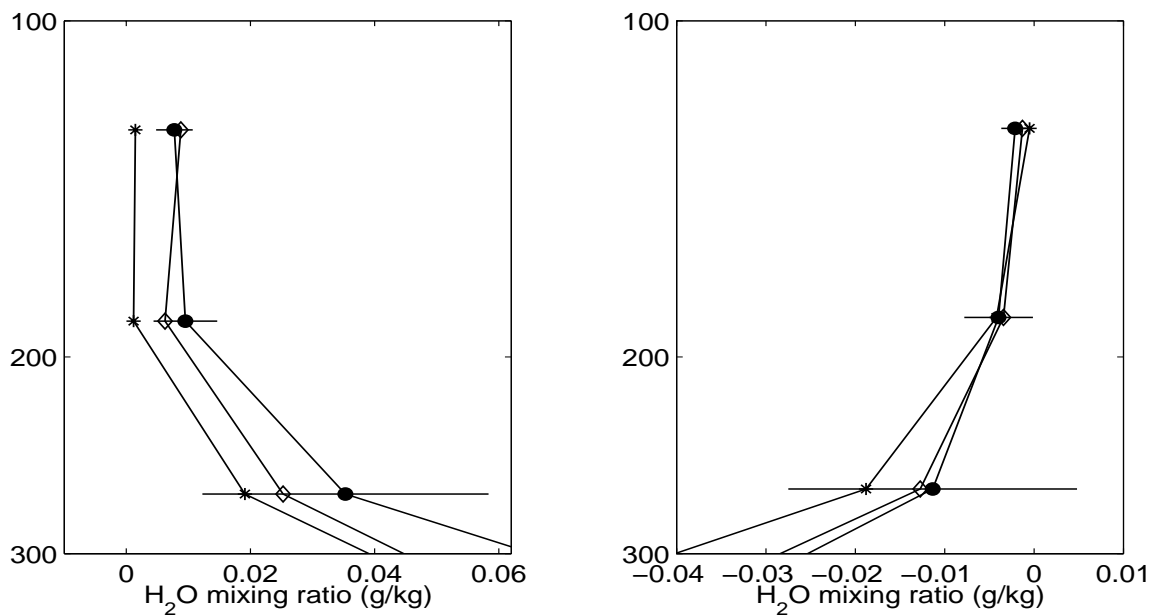


Figure 2.12 Left panel: the upper tropospheric water vapor mixing ratio retrieved from the IRIS PC1 (the line with filled circles), the CAM2 PC1 (the line with open diamonds), and the UCLA PC1 (the line with stars) over the northern Pacific. Right panel: same as left panel except over the southern Pacific.

2.5 Conclusion

Here we present a study of the temporal variability of the outgoing thermal IR spectra over two tropical ocean regions and two midlatitude ocean regions using IRIS data and the simulations from UCLA GCM and NCAR CAM2. Spectral EOF analysis is used to characterize the variability seen from the observed spectra and the synthetic spectra computed based on the GCM outputs. For the two tropical regions, cloud variability is the dominant contributor to the PC1 that accounts for more than 90% of the total variance. Compared to IRIS, UCLA GCM (CAM2) substantially underestimates (overestimates) the amplitude of the PC1 over the central Pacific and both GCMs significantly underestimate the amplitude of PC1 over the western Pacific. Further examinations show that the discrepancies between IRIS and the two models are insensitive to the parameterization schemes of cloud optical properties and cloud fraction used in the two models. The discrepancies over the western (central) Pacific are most likely caused by the deficiency in simulating the intraseasonal (seasonal) variation of the Walker circulation and the deep convection activities at the western Pacific.

For the two midlatitude regions, the PC1 is still the dominant contributor to the total variance and it captures seasonal variations from both the troposphere and the stratosphere. The PC1 over the northern Pacific has a different spectral shape from that over the southern Pacific. Compared to the IRIS observations over the northern Pacific, both UCLA GCM and CAM2 underestimate the variations at the CO₂ 667cm⁻¹ band and overestimate the variations at the window region. Using a retrieval scheme, we show that the discrepancies at the CO₂ band are due to a ~7K (4K) underestimation of the middle stratospheric temperature change by UCLA GCM (CAM2), and the discrepancies at

window regions are mainly due to an overestimation of the change of the skin temperature (the low cloud) by UCLA GCM (CAM2). Over the southern Pacific, the stratospheric temperature changes shown in the PC1s of two models are still smaller than those from IRIS PC1. Due to the difference in simulating the change of low cloud and the lower tropospheric temperature, the UCLA PC1 overestimates the variation at the window region and the CAM2 PC1 underestimates this variation.

The study presented here clearly demonstrates that the outgoing infrared spectra can be used to see the discrepancies between modeled and observed variability. The discrepancies can be understood with the help of various tools: sensitivity study of model parameterizations, analysis of model outputs, as well as retrieval. Compared to IRIS, the model can significantly overestimate the PC1 in one region but substantially underestimate it in another region. PC1s simulated by two models can be similar to each other in one region but very different in another region. Even when modeled PC1s are similar to each other, their error might be due to different changes in the vertical profiles (e.g. the northern Pacific case). All these show the promising potential of the outgoing thermal infrared spectra in validating GCMs.

2.6 Acknowledgement

We thank M. Gerstell, A. Ingersoll, Z. M. Kuang for helpful discussions. I am indebted to D. Noone for his help in learning CAM2 and S. S. Leroy for useful comments on technical issues. Computer resources for CAM2 simulation was kindly provided by NCAR Scientific Computing Division. UCLA GCM simulation was kindly provided by J. Farrara. IRIS data was kindly provided by L. Chen. Part of this research is supported by NOAA grant NA06EC0505 to the California Institute of Technology.

2.7 Appendix

The retrieval algorithm used in Section 2.4 is described in the following paragraphs.

The radiative transfer equation can be symbolically written as

$$\mathbf{R} = R(\mathbf{X}) \quad (2.4)$$

where \mathbf{R} is a vector of radiance, each element representing each frequency channel ν . \mathbf{X} is a vector of state variables (temperature, humidity, cloud) at different levels. $R(\mathbf{X})$ is the radiative transfer equation. Here, $R(\mathbf{X})$ is always MODTRAN 4.1, the same code used to generate synthetic spectra.

Linearizing equation (2.4), we have

$$\Delta\mathbf{R} = \mathbf{K}\Delta\mathbf{X}, \quad (2.5)$$

where $\mathbf{K} = \frac{\partial R_\nu}{\partial x_i}$ is usually called the Jacobian matrix. $\Delta\mathbf{R}$ is equivalent to the PC1

derived in this chapter and $\Delta\mathbf{X}$ is what we want to obtain. The difficulty of a direct inversion of (2.5) to obtain x_i lies in the fact that \mathbf{K} usually has a very large condition number so that the inversion of $\mathbf{K}^T\mathbf{K}$ is ill-posed. In order to achieve a reliable inversion, assumptions, statistical information, or both of them have to be used to “regularize” the Jacobian matrix, explicitly or implicitly.

The approach used here to regularize \mathbf{K} is similar to a commonly used approach, truncated singular value decomposition (SVD) of \mathbf{K} [Haskins *et al.*, 1999; Rodgers, 2000a]. It is based on an observation of the relation between the PC1 derived from the radiance space and the *principal components* of the vertical profiles of the state variables [Huang *et al.*, 2002] when only optically thin cloud is present. In detail,

(1) The area-averaged temperature profile, water vapor file, and cloud profile¹ are put together to make a vector of state variables \mathbf{X} .

(2) PCA is applied to an ensemble of vectors of state variables $[\mathbf{X}_{t1}, \mathbf{X}_{t2}, \dots]$ after normalizing them to unitary variance, so-called aggregated PCA [Bretherton, 2003].

(3) Take the first n leading *principal components* (PCs) which can explain the bulk of the total variance (at least >90%) and reversely scaled each element in PCs with the corresponding normalization factors used in (2) to make each element has same physical unit as it has in the original vector \mathbf{X} . Denote these scaled *principal components* as \mathbf{p}_i , where $i=1, 2, \dots, n$. Usually 7 or 8 leading PCs are enough to explain the bulk of the total variance.

(4) Evaluate radiance changes with respect to every scaled *principal components* obtained in (3)

$$\mathbf{dR}_i = \mathbf{R}(\bar{\mathbf{X}} + \mathbf{p}_i) - \mathbf{R}(\bar{\mathbf{X}}), \quad i = 1, 2, \dots, n \quad (2.6)$$

where $\bar{\mathbf{X}}$ is an vector containing ensemble-averaged state variables. Let

$$\mathbf{dR} = \begin{bmatrix} \mathbf{dR}_1 \\ \dots \\ \mathbf{dR}_n \end{bmatrix} \quad (2.7)$$

Matrix \mathbf{dR} is usually well-conditioned because the limited number of *principal components* used in step (4). So $\mathbf{dR}^T \mathbf{dR}$ can be directly inverted. Let

$$\mathbf{c} = (\mathbf{dR}^T \mathbf{dR})^{-1} \mathbf{dR}^T \Delta \mathbf{R} \quad (2.8)$$

Then the solution would be

¹ For the profile of cloud optical depth(τ), whenever the spatial average is needed, the average is done by $\bar{\tau} = -\ln\left(\frac{1}{N} \sum_{i=1}^N \exp(-\tau)\right)$ to take the strong nonlinearity between transmissivity and τ into account.

$$\Delta\mathbf{X} = \sum_{i=1}^N c_i \mathbf{p}_i \quad (2.9)$$

The residue is $[R(\bar{\mathbf{X}} + \Delta\mathbf{X}) - R(\bar{\mathbf{X}})] - \Delta\mathbf{R}$ and the error bar associated with the IRIS PC1 retrieval is estimated using information theory for the linear inverse problem, assuming that all probability distribution functions are Gaussian[Rodgers, 2000b]. The instrument noise of IRIS was estimated from *Hanel et al.* [1972]. Given the complexity involved in retrieving ozone profiles, the ozone band is not used in the retrieval.

The residual spectra for all the cases retrieved are shown in Figure 2.13. The statistics of these retrievals are summarized in Table 2.7. It can be seen that, for all cases, the fits are satisfactory.

	The northern Pacific			The southern Pacific		
	CAM2	IRIS	UCLA	CAM2	IRIS	UCLA
SSE	7.2	14.3	1.4	1.2	6.4	0.8
SST	814.9	577.4	1366.9	648.1	1158.9	618.2
R ²	0.991	0.975	0.999	0.998	0.994	0.999

Table 2.7 The goodness-of-fit statistics for each retrieval case. SSE is the Sum of Square due to Error, a measurement of total deviation of the fitted spectrum from the real one. SST is the total Sum of Square. R² measures how successful the fit is in explaining the variance of the spectrum.

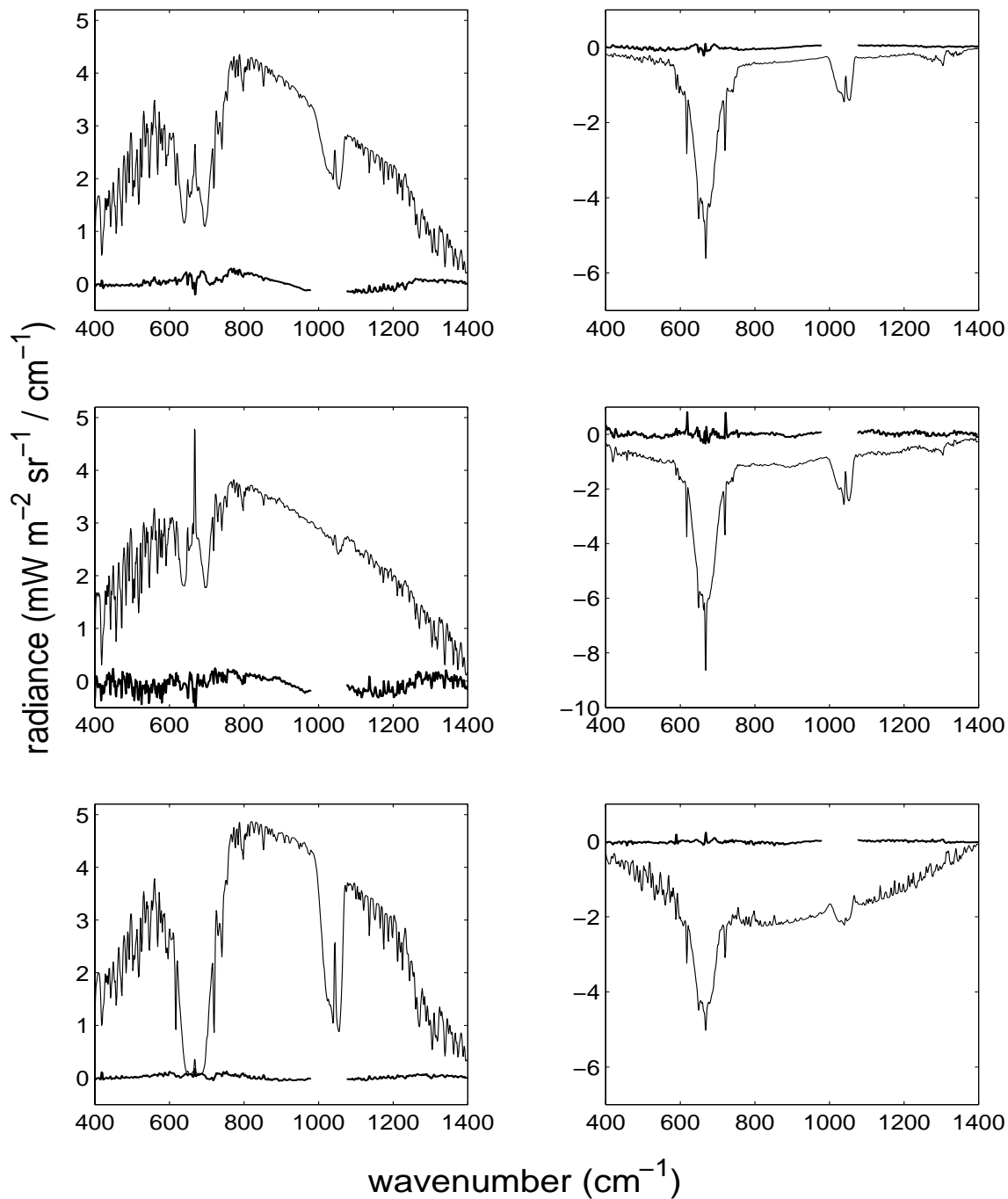


Figure 2.13 The PC1s (in thin solid lines) and the residual spectra after retrieval (in thick solid lines). Left panels are for the northern Pacific and right panels are for the southern Pacific. The upper ones are the CAM2 PC1s and their residuals. The middle ones are the IRIS PC1s and their residuals. The bottom ones are the UCLA PC1s and their residuals.

2.8 Reference

- Arakawa, A., and W. H. Schubert, Interaction of a cumulus cloud ensemble with large-scale environment .1, *Journal of the Atmospheric Sciences*, 31 (3), 674-701, 1974.
- Bergman, J. W., and M. L. Salby, Diurnal variations of cloud cover and their relationship to climatological conditions, *Journal of Climate*, 9, 2802-2820, 1996.
- Bergman, J. W., and M. L. Salby, The role of cloud diurnal variations in the time-mean energy budget, *Journal of Climate*, 10, 1114-1124, 1997.
- Bernstein, L. S., A. Berk, P. K. Acharya, D. C. Robertson, G. P. Anderson, J. H. Chetwynd, and L. M. Kimball, Very narrow band model calculations of atmospheric fluxes and cooling rates, *Journal of the Atmospheric Sciences*, 53 (20), 2887-2904, 1996.
- Bjerknes, J., Atmospheric teleconnections from the equatorial Pacific, *Monthly Weather Review*, 97 (3), 163-172, 1969.
- Bretherton, C.S., Empirical orthogonal functions and singular vectors, in *Encyclopedia of Atmospheric Sciences*, edited by J.R. Holton, J.A. Curry, and J.A. Pyle, pp. 620, Elsevier Science, London, 2003.
- Callaghan, P., A. Fusco, G. Francis, and M. Salby, A hough spectral model for three-dimensional studies of the middle atmosphere, *Journal of the Atmospheric Sciences*, 56 (11), 1461-1480, 1999
- Cheng, M. D., and A. Arakawa, Inclusion of rainwater budget and convective downdrafts in the Arakawa-Schubert cumulus parameterization, *Journal of the Atmospheric Sciences*, 54 (10), 1359-1378, 1997.

Collins, W. D., Parameterization of generalized cloud overlap for radiative calculations in general circulation models, *Journal of the Atmospheric Sciences*, 58 (21), 3224-3242, 2001.

Collins, W. D., J. K. Hackney, and D. P. Edwards, An updated parameterization for infrared emission and absorption by water vapor in the National Center for Atmospheric Research Community Atmosphere Model, *Journal of Geophysical Research-Atmospheres*, 107 (D22), art. no.-4664, 2002.

Gates, W. L., J. S. Boyle, C. Covey, C. G. Dease, C. M. Doutriaux, R. S. Drach, M. Fiorino, P. J. Gleckler, J. J. Hnilo, S. M. Marlais, T. J. Phillips, G. L. Potter, B. D. Santer, K. R. Sperber, K. E. Taylor, and D. N. Williams, An overview of the results of the Atmospheric Model Intercomparison Project (AMIP I), *Bulletin of the American Meteorological Society*, 80 (1), 29-55, 1999.

Goldberg, M. D., Y. N. Qu, L. M. McMillin, W. Wolf, L. H. Zhou, and M. Divakarla, AIRS near-real-time products and algorithms in support of operational numerical weather prediction, *IEEE Transactions on Geoscience and Remote Sensing*, 41 (2), 379-389, 2003.

Hanel, R. A., Salomons V, G. Wolford, I. Revah, Prabhaka.C, V.G. Kunde, and B.J. Conrath, Nimbus 4 infrared spectroscopy experiment .1. Calibrated thermal emission-spectra, *Journal of Geophysical Research*, 77 (15), 2629-2641, 1972.

Harshvardhan, D. A. Randall, T. G. Corsetti, and D. A. Dazlich, Earth radiation budget and cloudiness simulations with a General-Circulation Model, *Journal of the Atmospheric Sciences*, 46 (13), 1922-1942, 1989.

- Haskins, R., R. Goody, and L. Chen, Radiance covariance and climate models, *Journal of Climate*, 12 (5), 1409-1422, 1999.
- Haskins, R. D., R. M. Goody, and L. Chen, A statistical method for testing a general circulation model with spectrally resolved satellite data, *Journal of Geophysical Research-Atmospheres*, 102 (D14), 16563-16581, 1997.
- Hotelling, H., Analysis of a complex of statistical variables into principal components, *Journal of Educational Psychology*, 24, 417-498, 1933.
- Huang, H. L., and P. Antonelli, Application of principal component analysis to high-resolution infrared measurement compression and retrieval, *Journal of Applied Meteorology*, 40 (3), 365-388, 2001.
- Huang, X. L., D. Noone, J. Fararra, S. S. Leroy, Y. L. Yung, and R. M. Goody, The statistical characteristics of the outgoing spectra: inter-comparison between models and comparison between models and observations, in *2003 Fall AGU meeting*, Abstract A61C-0096, EOS Trans. AGU, 83 (47), San Francisco, 2002.
- Iacobellis, S. F., G. M. McFarquhar, D. L. Mitchell, and R. C. J. Somerville, The sensitivity of radiative fluxes to parameterized cloud microphysics, *Journal of Climate*, 16 (18), 2979-2996, 2003.
- Kalnay, E., M. Kanamitsu, R. Kistler, W. Collins, D. Deaven, L. Gandin, M. Iredell, S. Saha, G. White, J. Woollen, Y. Zhu, M. Chelliah, W. Ebisuzaki, W. Higgins, J. Janowiak, K. C. Mo, C. Ropelewski, J. Wang, A. Leetmaa, R. Reynolds, R. Jenne, and D. Joseph, The NCEP/NCAR 40-year reanalysis project, *Bulletin of the American Meteorological Society*, 77 (3), 437-471, 1996.

- Klein, S. A., and D. L. Hartmann, The seasonal cycle of low stratiform clouds, *Journal of Climate*, 6 (8), 1587-1606, 1993.
- Kohler, M., Explicit prediction of ice clouds in general circulation models, Ph.D. thesis, University of California, Los Angeles, Los Angeles, 1999.
- Lau, K.-M., and S. Yang, Walker circulation, in *Encyclopedia of atmospheric sciences*, edited by J.R. Holton, J.A. Curry, and J.A. Pyle, pp. 2505-2510, Elsevier Sciences, London, 2003.
- Lin, J. W. B., and J. D. Neelin, Considerations for stochastic convective parameterization, *Journal of the Atmospheric Sciences*, 59 (5), 959-975, 2002.
- Lin, J. W. B., and J. D. Neelin, Toward stochastic deep convective parameterization in general circulation models, *Geophysical Research Letters*, 30 (4), art. no.-1162, 2003.
- Madden, R. A., and P. R. Julian, Detection of a 40-50 day oscillation in zonal wind in tropical Pacific, *Journal of the Atmospheric Sciences*, 28 (5), 702-&, 1971.
- Madden, R. A., and P. R. Julian, Observations of the 40-50-day tropical oscillation - a review, *Monthly Weather Review*, 122 (5), 814-837, 1994.
- McFarquhar, G. M., S. Iacobellis, and R. C. J. Somerville, SCM simulations of tropical ice clouds using observationally based parameterizations of microphysics, *Journal of Climate*, 16 (11), 1643-1664, 2003.
- Naveau, P., and M. W. Moncrieff, A probabilistic description of convective mass fluxes and its relationship to extreme-value theory, *Quarterly Journal of the Royal Meteorological Society*, 129 (592), 2217-2232, 2003.

- Olsen, S. C., and J. T. Randerson, Differences between surface and column atmospheric CO₂ and implications for carbon cycle research, *Journal of Geophysical Research-Atmospheres*, 109 (D2), art. no.-D02301, 2004.
- Preisendorfer, R. W., *Principal component analysis in meteorology and oceanography*, 425 pp., Elsevier, New York, 1988.
- Rabbette, M., and P. Pilewskie, Multivariate analysis of solar spectral irradiance measurements, *Journal of Geophysical Research-Atmospheres*, 106 (D9), 9685-9696, 2001.
- Randall, D., M. Khairoutdinov, A. Arakawa, and W. Grabowski, Breaking the cloud parameterization deadlock, *Bulletin of the American Meteorological Society*, 84 (11), 1547-+, 2003.
- Rasch, P.J., and J. E. Kristjansson, A comparison of the CCM3 model climate using diagnosed and predicted condensate parameterizations, *Journal of Climate*, 11 (7), 1587-1614, 1998.
- Ricciardulli, L., and R. R. Garcia, The excitation of equatorial waves by deep convection in the NCAR Community Climate Model (CCM3), *Journal of the Atmospheric Sciences*, 57 (21), 3461-3487, 2000.
- Rodgers, C. D., Approximations, Short Cuts and Ad-hoc Methods, in *Inverse Methods for Atmospheric Sounding: Theory and Practice*, pp. 107-108, World Scientific Publishing, Singapore, 2000a.
- Rodgers, C. D., Information Aspects, in *Inverse Methods for Atmospheric Sounding: Theory and Practice*, pp. 24-26, World Scientific Publishing, Singapore, 2000b.

- Rossow, W. B., and R. A. Schiffer, Advances in understanding clouds from ISCCP, *Bulletin of the American Meteorological Society*, 80 (11), 2261-2287, 1999.
- Salby, M. L., Climate monitoring from space: Asynoptic sampling considerations, *Journal of Climate*, 2 (9), 1091-1106, 1989.
- Smith, J. A., and J. P. Taylor, Initial cloud detection using the EOF components of high-spectral-resolution infrared sounder data, *Journal of Applied Meteorology*, 43 (1), 196-210, 2004.
- Smith, W. L., and H. M. Woolf, Use of eigenvectors of statistical covariance matrices for Interpreting satellite sounding radiometer observations, *Journal of the Atmospheric Sciences*, 33 (7), 1127-1140, 1976.
- Wang, J. X., G. P. Anderson, H. E. Revercomb, and R. O. Knuteson, Validation of FASCOD3 and MODTRAN3: Comparison of model calculations with ground-based and airborne interferometer observations under clear-sky conditions, *Applied Optics*, 35 (30), 6028-6040, 1996.
- Webster, P. J., The large scale structure of the tropical atmosphere, in *Large-scale dynamical processes in the atmosphere*, edited by B.J. Hoskins, and P.R. P., pp. 235-275, Academic Press, London, 1983.
- Zhang, G. J., and N. A. McFarlane, Sensitivity of climate simulations to the parameterization of cumulus convection in the Canadian Climate Center General-Circulation Model, *Atmosphere-Ocean*, 33 (3), 407-446, 1995.
- Zhang, M. H., W. Y. Lin, C. S. Bretherton, J. J. Hack, and P. J. Rasch, A modified formulation of fractional stratiform condensation rate in the NCAR Community

Atmospheric Model (CAM2), *Journal of Geophysical Research-Atmospheres*,
108 (D1), art. no.-4035, 2003.

Chapter 3: Spatial variability of the outgoing
thermal IR spectra seen from AIRS data and
CAM2 simulations

3.1 Abstract

AIRS (Atmospheric Infrared Sounder) provides measurements of the outgoing thermal IR spectra with unprecedented data quality and dense coverage. Here we present a survey of the spatial variability in different climate zones seen from AIRS data using the spectral EOF analysis. Over the tropical and subtropical oceans, the first *principal component* (PC1) is mostly due to the thermal contrast between surface and optically-thick cold cloud top. The second *principal component* (PC2) is mainly due to the spatial variation of the lower tropospheric humidity (LTH) and the low clouds. Both the PC1 and the PC2 capture the variations in the upper tropospheric water vapor due to the forced orthogonality of EOF analysis. The third *principal component* (PC3) is mainly due to the spatial variation of the lower stratospheric temperature. Over the midlatitude oceans, the PC1 is still due to the thermal contrast of emission temperature. During wintertime, the PC2 is mainly due to the stratospheric temperature variations. In the summer, the PC2 over the northern-hemisphere midlatitude oceans is mainly due to the variations of the LTH and the low clouds; the PC2 over the southern-hemisphere midlatitude oceans is mainly due to the stratospheric temperature variations.

A parallel study using synthetic spectra based on a NCAR CAM2 simulation shows that the CAM2 simulation has a fairly good agreement with AIRS at both the tropical/subtropical and the midlatitude oceans. The major discrepancies between the simulation and AIRS are due to the incorrect locations of ITCZ over the western Pacific and the central Pacific, the underrepresented dust aerosol at the Arabian Sea and off the Atlantic Coast of North Africa, and the overestimated spatial variations of the lower stratospheric temperature over the midlatitude oceans in the CAM2 simulation.

3.2 AIRS and data manipulation

Atmospheric Infrared Sounder (AIRS) is an infrared grating array spectrometer aboard AQUA, a sun-synchronous satellite [Aumann *et al.*, 2003]. It acquires 2.9 million spectra everyday with 2378 channels across three bands¹ (3.74-4.61 μm , 6.20-8.22 μm , 8.8-15.4 μm). The resolving power ($\lambda/\Delta\lambda$) of AIRS is 1200. The instrument field of view is 1.1 degree, corresponding to a footprint of 13.5km on the surface. The scan angles vary from -49° to 49°. The global data coverage can be obtained in the course of 2 days. The in-flight calibrations show that the radiometric accuracy is $< 0.3\text{K}$ for a 250K brightness temperature target [Pagano *et al.*, 2003], and the spectral accuracy is $< 0.01\Delta\nu$ ($\Delta\nu$ is the full width of half maximum) [Gaiser *et al.*, 2003]. AIRS provides us an unprecedented data source of the outgoing thermal IR spectra with excellent calibration and good global coverage.

In this study, we mainly use 16 days of AIRS level-1B calibrated radiance from July 01 to July 16, 2003. The data from January 01 to January 16, 2003, will be used to illustrate the winter/summer contrast. Sixteen days is an orbital repeat cycle for AIRS so that a uniform spatial sampling pattern can be expected within this period. We limit our study to the spectra with scan angles (θ) between $\pm 5^\circ$ ($1 \leq 1/\cos\theta \leq 1.0039$) so that all spectra can be treated as nadir-view spectra and no geometry correction is necessary. Among 2378 AIRS frequency channels, some of them constantly suffer from the fluctuation of electronic noise (so-called “popcorn noise”) and some have bad spectral response functions. To avoid these channels, only channels recommended by the AIRS

¹ AIRS has 17 linear arrays arranged onto 12 modules on the focal plan. For some arrays, the end frequency has no overlap with the starting frequency of the next array. As a result, several gaps exist inside each band. This fact and the popcorn noise problem make degrading AIRS spectra very challenging.

team for level-2 retrieval purpose are used. Furthermore, spectra in 3.74-4.61 μm band are excluded due to a consideration of signal-to-noise ratio (SNR)¹. Besides these, we screen data with a fairly strict quality control procedure to exclude any possible bad spectra. It turns out that, on the average, only 2.4 out of per thousand spectra have to be thrown out after the quality control.

We divide the global surface into 3240 grid boxes, each being 4° in latitude and 5° in longitude. Inside each grid box, AIRS spectra collected at the ascending nodes and at the descending nodes within the 16-day period are equally weighted and averaged to obtain a mean spectrum for each grid box. Then we apply the spectral EOF analysis to these averaged spectra within a given climate zone to obtain the *principal components* and associated spatial patterns. The climate zones that we study are the tropical and the subtropical oceans (32°S - 32°N), the northern-hemisphere midlatitude oceans (hereafter, NHMO) (32°N-60°N) and the southern-hemisphere midlatitude oceans (hereafter, SHMO) (60°S-32°S).

Figure 3.1 shows, after quality control, the number of qualified spectra inside each grid box of the tropics and the subtropics from July 1 to July 16, 2003. It can be seen that the sampling is fairly uniform for both daytime and nighttime. For daytime and nighttime together, the averaged number of spectra in each grid box is 1604 and the standard deviation is 37. Several grid boxes in Africa and the southern ocean west of Australia have ~250 spectra less than the mean because of the two data outage periods on July 9 due to AIRS and MODIS internal calibrations. Several grid boxes in the tropical

¹ The SNR at 3.74-4.61 μm band is smaller than other bands, mostly due to the small signals in this band. Moreover, whether 3.74-4.61 μm band is included or not, the results of the spectral EOF analysis at the other two bands are almost identical to each other. This is mostly due to the fact that radiances at 3.74-4.61 μm band are smaller than those at the other two bands by one or two orders of magnitude.

Pacific also have ~ 100 spectra less than the mean because, from time to time, very cold cloud tops existed in these boxes and AIRS failed in generating correctly calibrated radiance for such scenes. If these grid boxes are excluded, the standard deviation is only 14. The uniform sampling pattern gives us more confidence in analyzing the spatial variability from these qualified spectra.

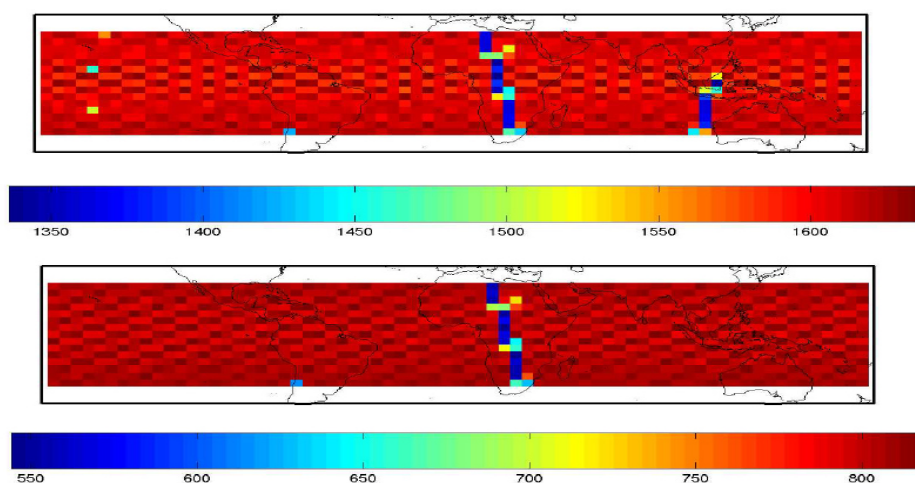


Figure 3.1 Upper panel: number of qualified daytime and nighttime spectra used for averaging in each grid box. Lower panel: number of qualified daytime spectra used for averaging.

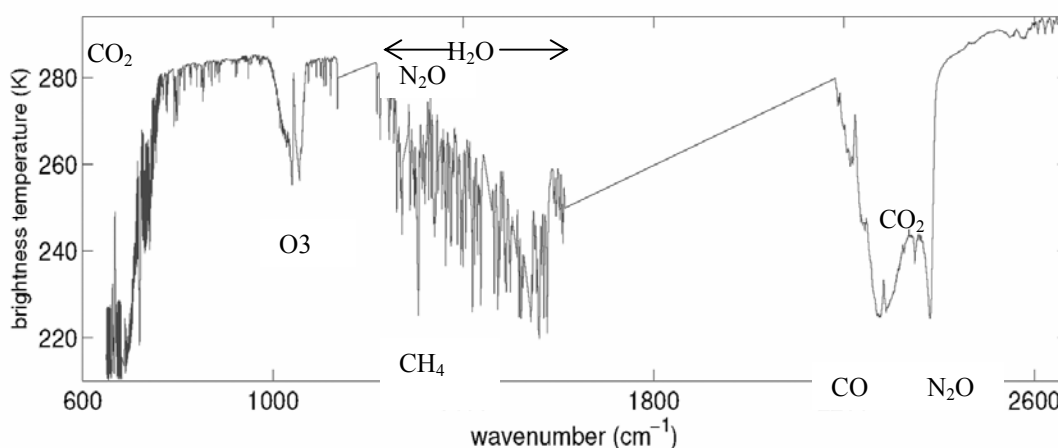


Figure 3.2 The mean AIRS spectrum over oceans within 32°S - 32°N from July 1-16, 2003. The major absorption features are labeled.

3.3 The tropical/subtropical oceans

3.3.1 Basic results and interpretations

The mean spectrum over the tropical and the subtropical oceans from July 1 to 16 of 2003 is presented in Figure 3.2. Compared to IRIS mean spectra shown in the last chapter, the spikes at the band centers of the CO₂ 667 cm⁻¹ band, the CO₂ 720 cm⁻¹ band, and the CH₄ 1306 cm⁻¹ band are more prominent due to the much higher spectral resolution of AIRS data.

Table 3.1 lists the fraction of variance explained by the three leading *principal components* when the spectral EOF analysis is applied to different subsets of AIRS data over the tropical/subtropical oceans. It turns out that, as far as the explainable fraction of variance is concerned, there is only a slight difference between the results from different subsets. The PC1 is absolutely dominant in all cases. For all subsets listed in Table 3.1, 99.5% of the variance can be explained by the first three PCs.

	Daytime + Nighttime spectra	Daytime spectra only	Nighttime spectra only
PC1	97.0% (97.3%)	97.5% (97.5%)	96.8% (96.8%)
PC2	2.2% (1.8%)	1.8% (1.75%)	2.3% (2.4%)
PC3	0.5% (0.5%)	0.4% (0.4%)	0.5% (0.4%)

Table 3.1 The percentage of the variance explained by the leading three PCs for different subsets of AIRS tropics/subtropics data. The numbers in parentheses are the results from the spectral EOF analysis to both the continental and the maritime data. Other numbers are from the analysis to the maritime data only.

The three leading PCs and their spatial maps ¹ derived from the tropical/subtropical maritime data are presented in Figure 3.3 and Figure 3.4, respectively. The PC1 (Figure 3.3a) is flat at the CO₂ 667cm⁻¹ band, indicating little contribution from the middle stratosphere to the PC1. The remaining part of the PC1 resembles the shape of the mean spectrum to a large extent. The minima in the PC1 spatial map (the upper panel

¹ As mentioned in Chapter 2, all spatial maps are normalized with zero mean and unitary standard deviation.

of Figure 3.4) overlap with summer ITCZ (Inter Tropical Convergence Zone). Over the Atlantic and the eastern Pacific oceans, ITCZ is usually narrow in latitude and lies just north of the equator. Over the Indian and the western Pacific oceans, ITCZ is broad in latitude. All these features of summer ITCZ [Waliser and Gautier, 1993] can be identified from the PC1 spatial map. Based on the spectral shape of the PC1 and its spatial map, it can be concluded that the PC1 is due to the contrast of emission temperatures between the cold cloud top in the presence of optically thick cloud and the warm surface where cloud is absent. When cloud is formed due to the deep convection, the cloud is so thick that essentially no radiation emitted from surface can penetrate the cloud. As a result, only emission from the cloud top or above can be seen from space. The PC1 here just sees the temperature difference between cold cloud top and warm surface. This interpretation can be confirmed by examining the correlation coefficient (r_{corr}) between the PC1 spatial map and the radiance map of each frequency channel. For some frequency channels in the window region, r_{corr} can be as high as 0.999. The good agreement between the PC1 spatial map and high cloud climatology of July (Figure 3.5a) derived from ISCCP D2 data [Rossow and Schiffer, 1999] also supports this interpretation.

The PC2 shown in Figure 3.3b is more complicated than the PC1. It exhibits several spectral features. The CO₂ 667cm⁻¹ band is not flat, indicating the contributions from the stratosphere. The CO₂ 720cm⁻¹ band peaks downward. The weak water vapor absorption lines in the window region peak upward. The center of the Q-branch of CH₄ fundamental band is close to zero. The water vapor ν_2 band (1595 cm⁻¹) is significantly nonzero, indicating the contributions from upper tropospheric water vapor. The

correlation coefficient between the PC2 spatial map and the radiance map of any frequency channel is within ± 0.6 . The PC2 spatial map (the middle panel of Figure 3.4) has local maxima off the coasts of California, Peru, and Namibia as well as over the Canary Islands and the southern ocean west of Australia. These are also regions well known for the high occurrence of low clouds, mostly marine stratus [Klein and Hartmann, 1993]. The PC2 spatial map matches the map of July low cloud climatology (Figure 3.5b) from ISCCP D2 data very well except over the Arabian Sea. When marine stratus is formed, the entrainment at the cloud top tends to dry the layer just above the cloud top [Houze, 1993]. Therefore, the maxima in low cloudiness usually correspond to the minima in the relative humidity of the layer above the low clouds. As a result, the minima in the map of 850mb relative humidity (Figure 3.5c) derived from NCEP daily reanalysis data [Kalnay *et al.*, 1996] consistently correspond to the maxima in the PC2 spatial map except over the Arabian Sea. These spatial features suggest that PC2 could be mostly due to the low cloud and the lower tropospheric humidity (LTH) variations. The PC2 also captures other variations because of the forced orthogonality to PC1. Further interpretation about the PC2 will be given in the next subsection.

The third *principal component*, PC3, accounts only for $\sim 0.4\%$ of the total variance. But its spectral shape and spatial map are still meaningful. Based on North's criterion [North *et al.*, 1982], sampling uncertainties do not have significant effects on PC3. The spectral features at the CO_2 667 cm^{-1} and 720 cm^{-1} bands and the O_3 1042 cm^{-1} band are significantly nonzero. For the other parts, it is close to zero. These mean that the PC3 is mainly due to the temperature variations in the stratosphere and the upper troposphere, to which the aforementioned three bands are sensitive. The PC3 spatial map

(the lower panel of Figure 3.4) is zonally uniform. The negative (positive) values in the PC3 spatial map mean colder (warm) brightness temperature at CO₂ 667cm⁻¹ band than the mean spectrum. This is consistent with the fact that the tropical lower stratosphere is colder than the subtropical counterpart. The maximum correlation coefficient between the PC3 spatial map and the radiance map of a given AIRS frequency channel is 0.9. The corresponding frequency channel is 651.3cm⁻¹, a frequency with the contribution function peaking at 117mb, further confirming the lower stratosphere and the upper troposphere as the major contributors to the PC3. The map of the NCEP upper tropospheric and lower stratospheric temperature averaged over the same period (Figure 3.5d) agrees with the PC3 spatial map to a large extent. This also supports the interpretation of the PC3.

If the continental data are included in the analysis, the spectral shapes of the PC1 and the PC2 are basically the same. But the amplitude of the PC1 is larger because of high surface temperature over continental deserts that makes the surface/cloud top thermal contrast even larger. The slopes at the window regions of the PC2 and the PC3 are different. The possible causes for this difference in slope are (1) the spectrally dependent surface emissivity in the window region can vary significantly for different types of land surface [Wilber *et al.*, 1999]; (2) the subtropical continental warm clouds usually have smaller effective radii than the subtropical maritime warm clouds due to the maritime-continental contrast of the number of CCN (cloud condensation nuclei) [Han *et al.*, 1994], and the different cloud effective radii can affect the slope at the window region even when the cloud optical depths are the same [King *et al.*, 1992; Prabhakara *et al.*, 1988]. The spatial maps of the three leading PCs derived from all data over the tropics/subtropics are consistent with the maps shown in Figure 3.4.

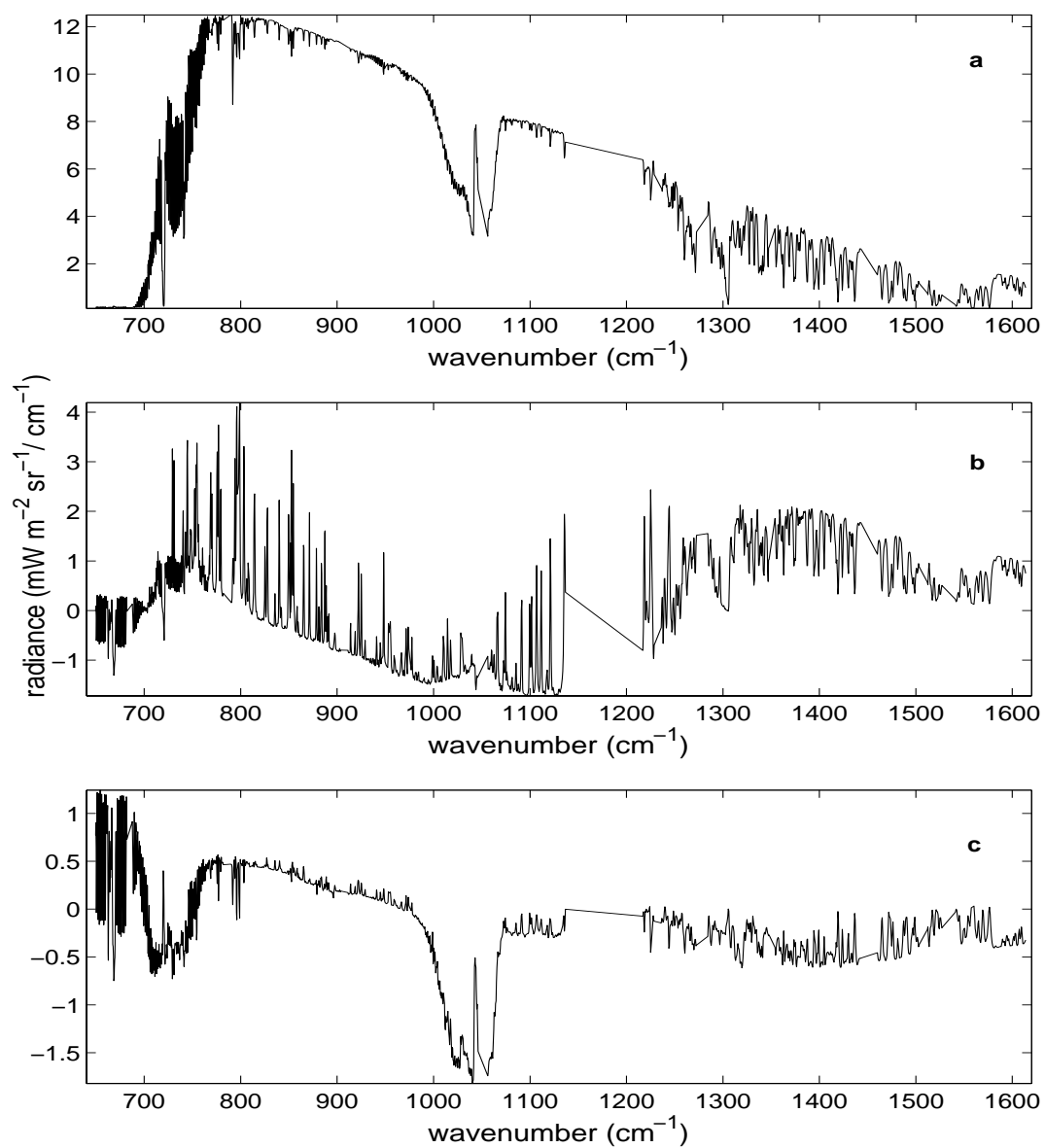


Figure 3.3 (a) The PC1 over the tropical/subtropical oceans between 32°S and 32°N derived from AIRS spectra collected during July 01-16, 2003. (b) The PC2. (c) The PC3.

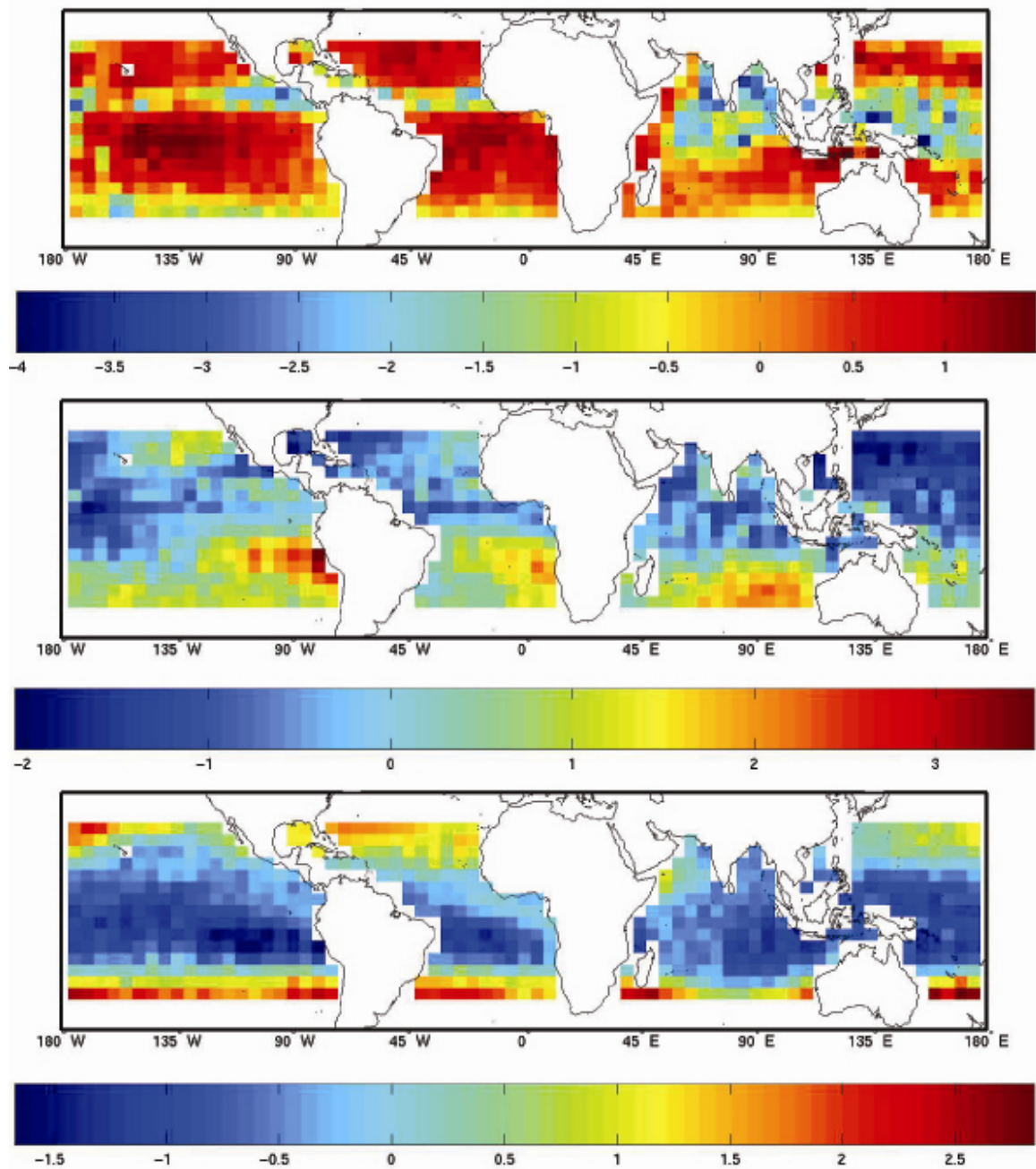


Figure 3.4 Upper panel: the spatial map of the PC1 shown in Figure 3.3a. Middle panel: the spatial map of the PC2 shown in Figure 3.3b. Lower panel: the spatial map of the PC3 shown in Figure 3.3c.

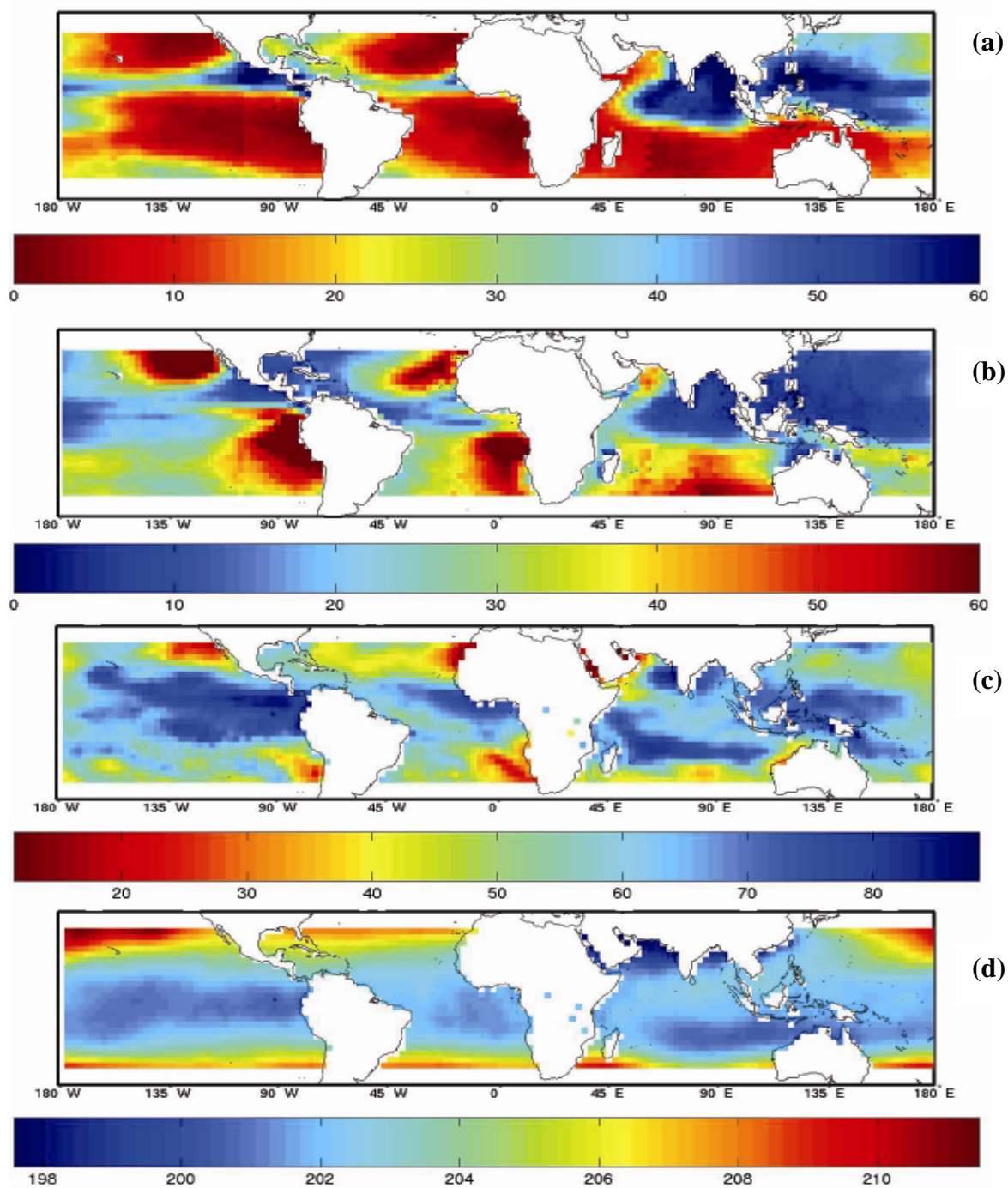


Figure 3.5 (a) The climatological high cloud amount in July from ISCCP D2 dataset. (b) The climatological low cloud amount in July from ISCCP D2 dataset. (c) The 850mb relative humidity averaged over July 01 - July 16, 2003 from NCEP daily reanalysis product. (d) The temperature in the layer of 150mb-70mb averaged over July 01-July 16, 2003, also from NCEP.

Examining AIRS data over the tropical and the subtropical oceans from January 01 to January 16 of 2003 with the spatial-spectral EOF technique yields similar results. The PC1 spatial map shows minima overlapped with the wintertime ITCZ, the PC2 spatial map is consistent with the January low cloud climatology, and the PC3 spatial map shows patterns resembling the upper tropospheric and the lower stratospheric temperature variations.

3.3.2 Further interpretation of the PC2

The PC2 spatial map shows features consistent with the map of low cloud amount, but its spectra shape shows contributions from the stratosphere (the nonzero CO₂ 667 cm⁻¹ band) and the upper tropospheric water vapor (the nonzero water vapor 1596 cm⁻¹ band) as well. This can be understood in terms of the forced orthogonality between each principal component and its predecessors. Figure 3.6 is a schematic plot showing a system with several factors contributing to the variability of the system. These factors might be neither independent (“orthogonal”) nor totally dependent (“parallel”) on each other. For example, at the ascending branches of the Hadley Circulation or the Walker Circulation, high cloud would form and upper troposphere humidity (UTH) would be enriched due to the convection; at the descending branches, the upper troposphere would be dehydrated and a temperature inversion layer would form in the lower troposphere that helps the formation of marine stratus [Houze, 1993]. Therefore, the variation in UTH is correlated with the changes of both high cloud and low cloud. Meanwhile, if one of these factors contributes to the variance much more than any other factors do, the PC1 from the EOF analysis would be similar to the imprint of this dominant factor. But the PC1 would not be identical to the imprint of this dominant factor because, as long as these factors are

not “orthogonal” to each other, the PC1 always tries to capture projections from other factors so that it can maximize the explainable fraction of variance. Therefore, the PC1 would be slightly different from the imprint of the dominant factor. Given the fact that the PC2 is forced to be orthogonal to the PC1, these factors would have projections onto the PC2 too. The one having the largest projection onto the PC2 (the factor “nearest” to the PC2) would be seen from the PC2 spatial map more easily than any other factors. In this case, LTH and the low cloud, two factors which are closely related to each other, should be the factors “nearest” to the PC2, as sketched in Figure 3.6. Therefore, the PC2 spatial map has good agreement with the spatial map of LTH and the low cloud. Meanwhile, the PC2 also has projections from the upper tropospheric humidity and the stratosphere, which are shown in its spectral shape.

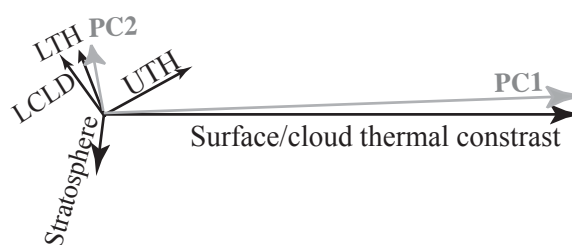


Figure 3.6 A schematic plot to conceptually demonstrate the results of EOF analysis to a system with correlated factors. LCLD refers to the low cloud. LTH and UTH refer to the lower and upper tropospheric humidity, respectively.

To further understand the effect of cloud on the PC2, we carry out two simple simulations with NCEP daily reanalysis data from July 01 to July 16, 2003 and ISCCP July climatology of cloud distribution and cloud optical depth. The first simulation (hereafter, clear-sky case) computes the spectra based on NCEP 16-day average of temperature and humidity profiles over each 4° by 5° grid box with no cloud information included. The second simulation (hereafter, cloudy case) computes the spectra based on

both NCEP data and ISCCP July climatology of cloud amount, cloud height, as well as cloud optical depth over each grid box. Both simulations are done using MODTRAN¹. We apply spectral EOF analysis to these two sets of synthetic spectra in the same way as we apply it to AIRS data. For the clear-sky case, the PC1 and the PC2 can explain 88% and 10% of the total variance, respectively. This is because the PC1 of the clear-sky case is mainly due to the emission surface temperature contrast between different regions and this contrast is significantly smaller than the contrast between surface and cold cloud top. The PC2 spatial map of the clear-sky case has a correlation coefficient of 0.996 with the radiance map at 1244 cm^{-1} , a channel which is sensitive to water vapor and has a weighting function peaking at $\sim 550\text{mb}$. In the thermal IR region, the nadir-view weighting function usually has a broad width [Goody and Yung, 1989]. Therefore, this good correlation means that the PC2 is essentially due to the variation of the column water vapor density. This explanation is supported by examining the PC2 spatial map of the clear-sky case shown in Figure 3.7a. The minima in this map correspond to regions rich in water vapor: ITCZ and margins of midlatitude cyclone systems where water vapor is supplied through the lower-level convergence. The maxima in this map correspond to regions poor in water vapor: primarily the descending branches of the Hadley circulation in the subtropics where the atmosphere has been dried out. Therefore, the first two PCs for the clear-sky case are mainly due to the variation of surface temperature and the variation of column water abundance, respectively.

¹ The highest spectral resolution (FWHM) that MODTRAN can correctly generate is 2cm^{-1} . For AIRS, its resolution varies with frequencies and is about $0.5\sim 1.0\text{cm}^{-1}$ in the spectral range that we look at. This difference in spectral resolution should have little impact on the EOF results. More detailed discussion is given in section 3.5.

For the cloudy case, the PC2 spatial map is not highly correlated with the radiance map of any channel: all correlation coefficients are within ± 0.77 , similar to the situation of the AIRS PC2. Moreover, the spatial map as shown in Figure 3.7b has a very good agreement with the low cloud amount map used in this simulation (Figure 3.5b). Therefore, when cloud is included, the variation of cloud top (mostly high cloud top) is “aliased” to the PC1 and the variation of low cloud is “aliased” to the PC2.

Traditionally visible reflectance is used to observe low cloud because of its high albedo in the visible range. The relatively small thermal contrast between surface and low cloud top makes direct observation of low cloud from IR window channels of meteorological satellites difficult. Here we show that, using spatial-spectral EOF as a way to decompose thermal IR spectra, the variation of low cloud and associated LTH in the tropical and subtropical oceans can be clearly seen in the PC2 and its spatial map.

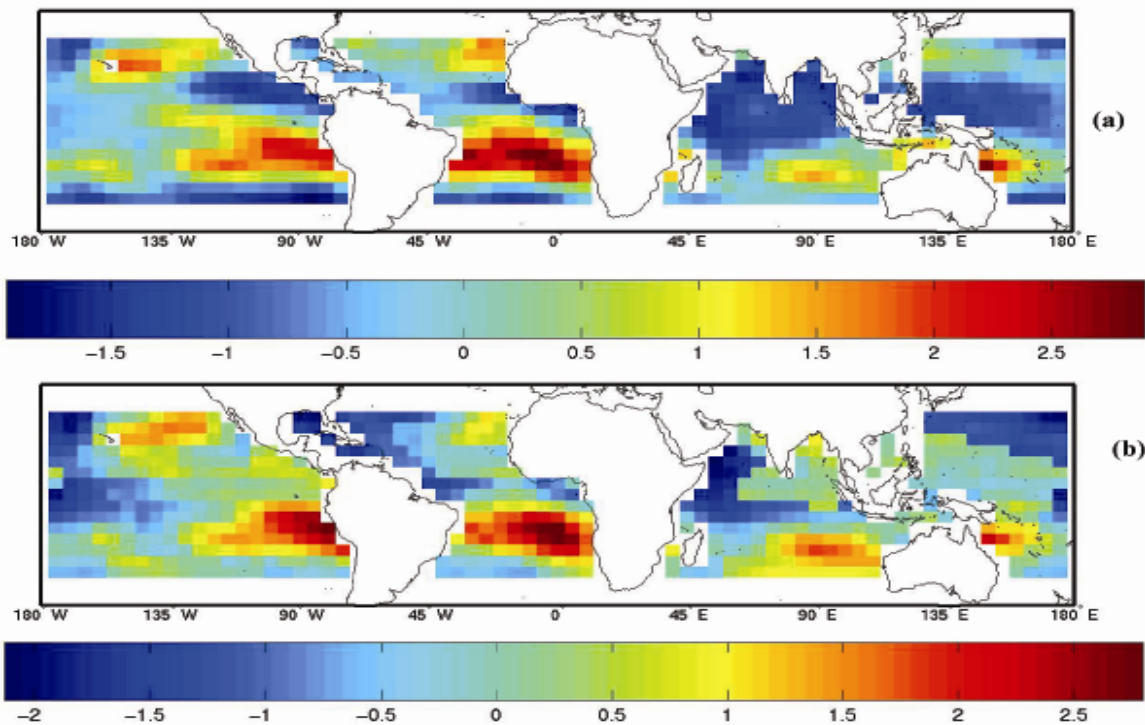


Figure 3.7 (a) The PC2 spatial map of the simulated clear-sky case (b) The PC2 spatial map of the simulated cloudy case. Refer to the context for the definitions of the clear-sky case and the cloudy case.

3.4. The midlatitude oceans

Table 3.2 summarizes the fraction of variance explained by three leading PCs over the northern hemisphere midlatitude oceans (32°N-60°N) and the southern hemisphere midlatitude oceans (32°S-60°S) (for brevity, hereafter NHMO and SHMO, respectively). Similar to the case of the tropical/subtropical oceans, the PC1 is absolutely dominant here and three leading PCs together can explain more than 99.5% of the variance.

	PC1	PC2	PC3
32°N-60°N	97.7%	1.7%	0.5%
32°S-60°S	97.3%	1.8%	0.6%

Table 3.2 The percentage of variance explained by three leading PCs over NHMO and SHMO.

The spectral shapes of the PC1s over the NHMO and the SHMO (shown in Figure 3.8a and 3.8c) are similar to that of the PC1 over the tropical/subtropical oceans except that both midlatitude PC1s capture a small contribution from the stratosphere shown in the CO_2 667cm^{-1} band. PC1s here are still mainly due to the contrast of emission temperatures, including the poleward variation in surface temperature and the temperature contrast between surface and cloud top.

The PC2 over the NHMO (Figure 3.8b) shows spectral features at the CO_2 667cm^{-1} band as well as weak water vapor absorption lines at the window regions. Near the center of the water vapor 1596cm^{-1} band, it is fairly flat and close to zero. The spatial map of PC2 over the NHMO (Figure 3.9a) has maxima over the North Pacific, the North Atlantic and near the west coast of North America, consistent with ISCCP July low cloud climatology (Figure 3.9b). The interpretation of this PC2 is similar to the PC2 over the tropical/subtropical oceans: it is mainly due to the variation of LTH and low cloud but captures the variation from the stratospheric temperature as well due to the forced orthogonality by EOF analysis.

The PC2 over the SHMO (Figure 3.8d) has two sharp spikes at the centers of the CO_2 667cm^{-1} and 720cm^{-1} bands. Besides these two CO_2 bands and the O_3 band, the PC2 is rather flat and close to zero. This clearly indicates that the PC2 is due to the temperature changes in the stratosphere and the upper troposphere. The spatial map of PC2 shown in Figure 3.9c has maxima (corresponding to a cold stratosphere) at the margin of the polar vortex and minima (corresponding to a warm stratosphere) over the midlatitude southern ocean, consistent with the 100mb temperature map (Figure 3.9d) derived from NCEP daily reanalysis product over the same period.

Applying spectral EOF analysis to the synthetic spectra over the NHMO and the SHMO based on NCEP reanalysis daily product over the same period and ISCCP climatology in July (hereafter, NCEP+ISCCP case), we can obtain similar results. Figure 3.10 shows the PC2s and their spatial maps from such analysis. It can be seen that, for both the spectral features and the spatial maps, the PC2s from this NCEP+ISCCP case agree with the AIRS PC2s reasonably well except for the CO₂ 667 cm⁻¹ band of the PC2 over the NHMO. The spatial map of the PC2 over the NHMO (Figure 3.10c) shows maxima at those areas frequently covered by low clouds, consistent with the low cloud climatology used in this simulation (Figure 3.9b). The spatial map of the PC2 over the SHMO (Figure 3.10d) is consistent with the spatial distribution of NCEP upper tropospheric and lower stratospheric temperature variations (Figure 3.9d).

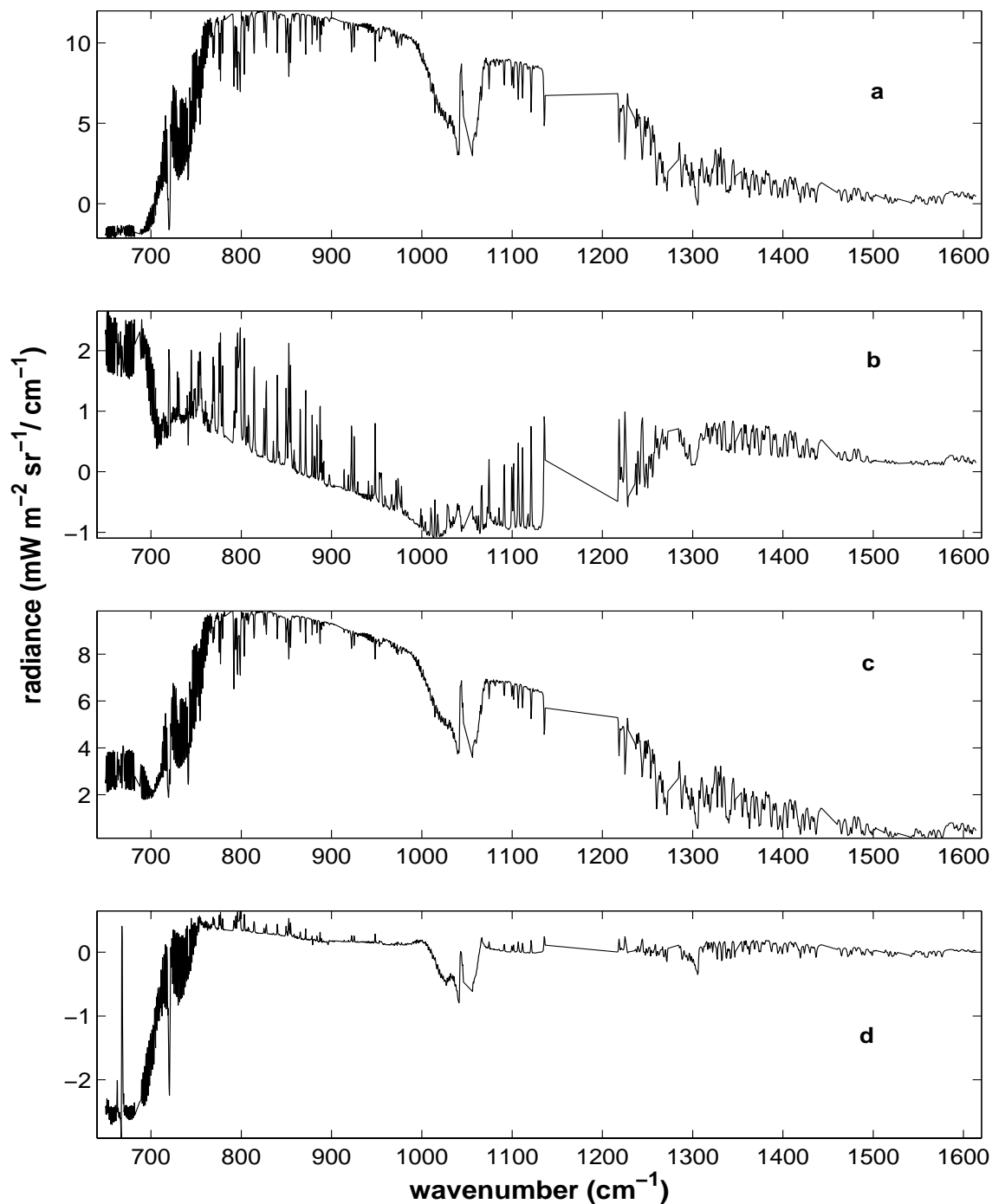


Figure 3.8 The PC1s and PC2s over the NHMO and the SHMO. (a) the PC1 over the NHMO. (b) the PC2 over the NHMO. (c) Same as (a) except at the SHMO. (d) Same as (b) except over the SHMO.

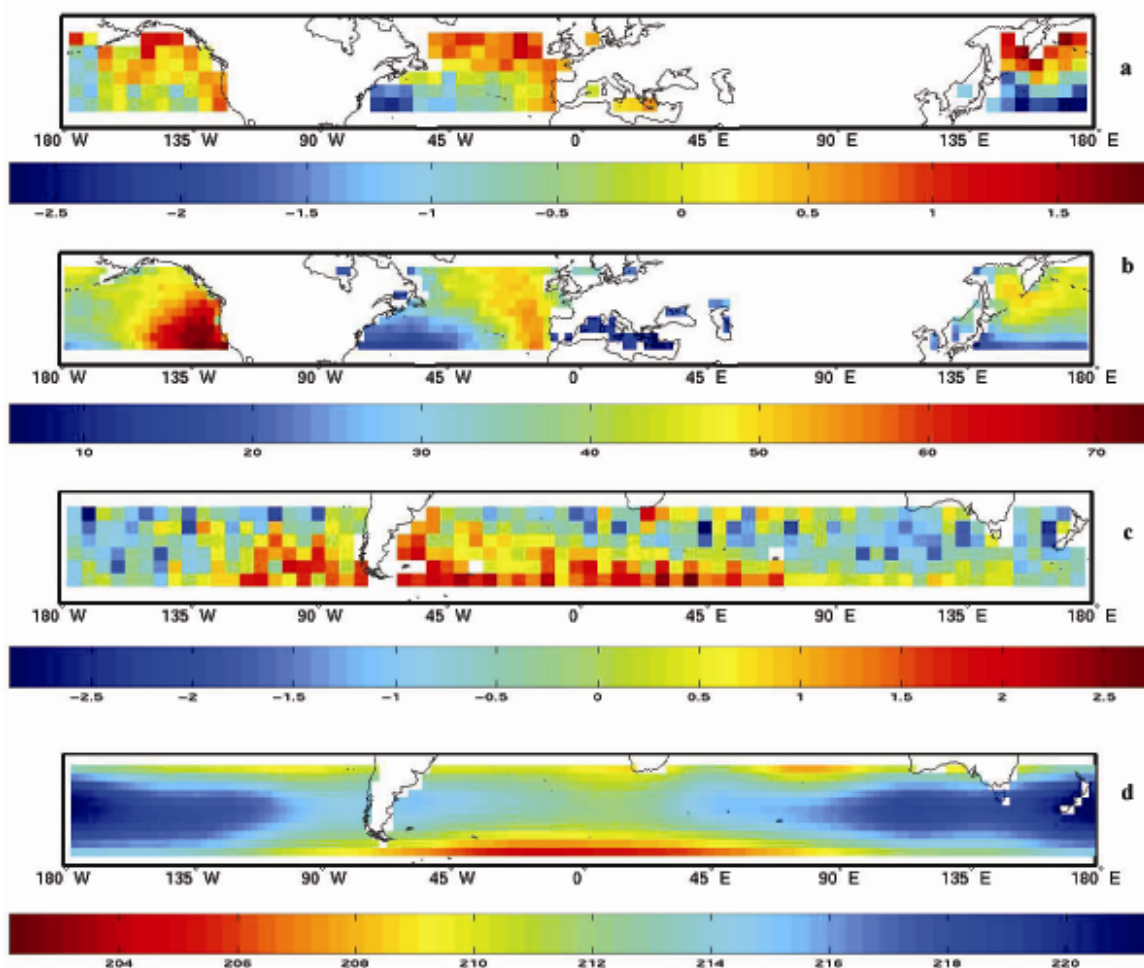


Figure 3.9 (a) The PC2 spatial map over the NHMO. (b) The ISCCP climatological low cloud amount of July over the same regions as (a). (c) The PC2 spatial map over SHMO. (d) The NCEP 16-day (July 01-16, 2003) average of 100mb temperature over the same regions as (c).

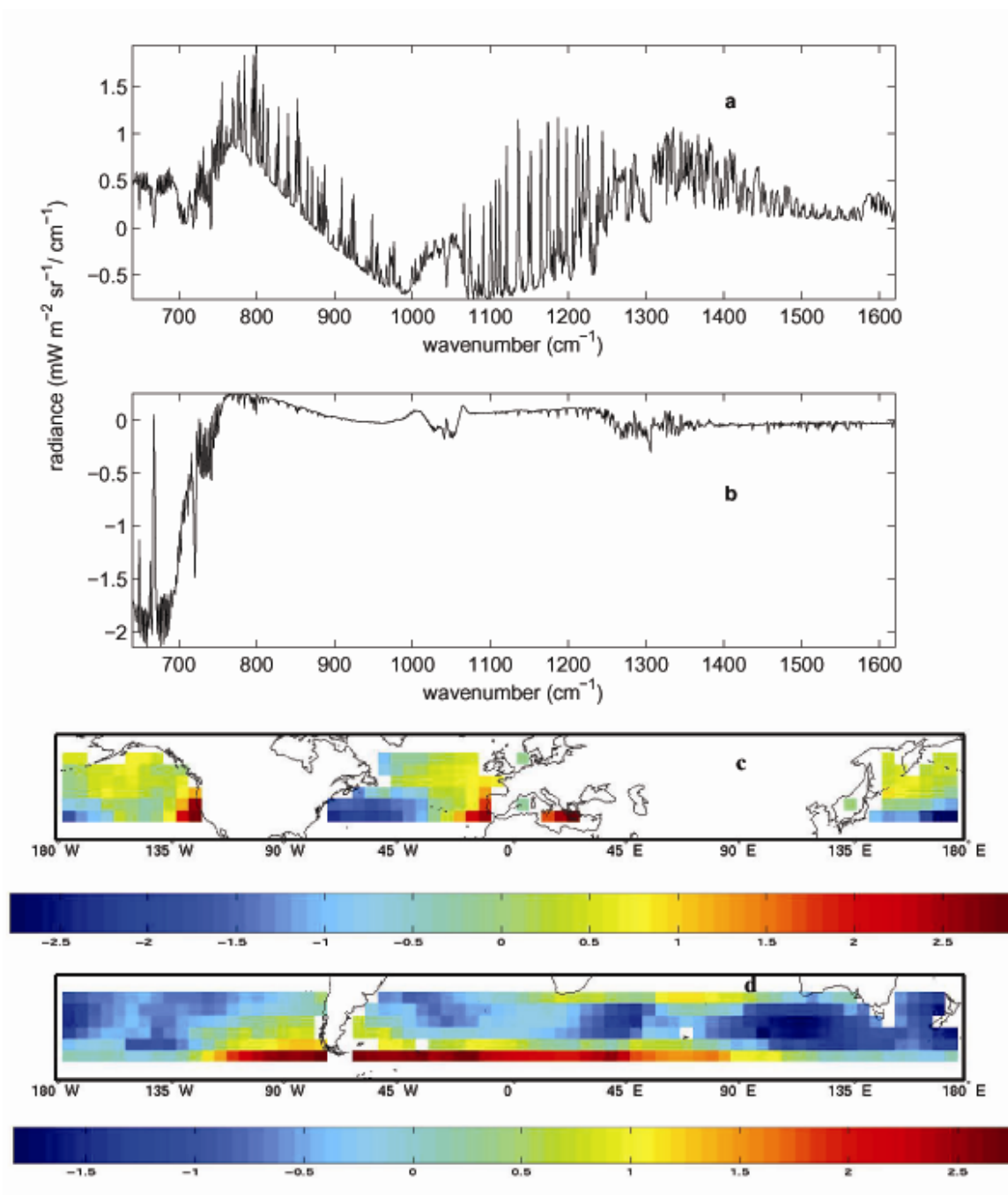


Figure 3.10 (a) The PC2 over the NHMO derived from the NCEP+ISCCP case. (b) The PC2 over the SHMO derived from the NCEP+ISCCP case. (c) The spatial map associated with the PC2 in (a). (d) The spatial map associated with the PC2 in (b).

From the above paragraph, the PC2 over the SHMO has a different spectral shape and a different explanation from that over the NHMO. This is partially due to the summer-winter contrast between the NHMO and the SHMO. To further understand these differences, it would be instructive to examine the PC2s from January AIRS data. The PC2s over the NHMO and the SHMO derived from AIRS data for January 01-16, 2003 are shown in Figure 3.11. The PC2 over the NHMO in January (Figure 3.11a) resembles the PC2 over the SHMO in July, both having two sharp spikes at the centers of two CO₂ bands and relatively flat window region and water vapor band. However, the PC2 over the SHMO in January (Figure 3.11b) is not similar to the PC2 over the NHMO in July: it mainly shows the stratospheric contributions although it captures the variations in the weak water vapor absorption lines in the window region.

The similarity between the wintertime PC2s over the NHMO and the SHMO is due to the strong disturbance of the stratosphere in winter by the vertical propagation of the planetary waves originated in the troposphere [Holton, 1983]. As a result, the spatial variation of the stratospheric temperature is so large that its contribution to the variance of spectra is second only to the emission temperature contrast. In the summertime, the stratosphere is relatively undisturbed due to the existence of the critical surface (zero zonal wind) in the lower stratosphere [Charney and Drazin, 1961; Holton, 1983]. Meanwhile, owing to the more prominent land-sea contrast in the northern hemisphere than in the southern hemisphere, the lower tropospheric humidity and the low cloud at the summertime NHMO exhibit larger spatial variations than those at the summertime SHMO. As a result, the PC2 over the summertime NHMO is “biased” to the variations of

the LTH and the low cloud and the PC2 over the summertime SHMO is still mostly due to the variation of the stratospheric temperature.

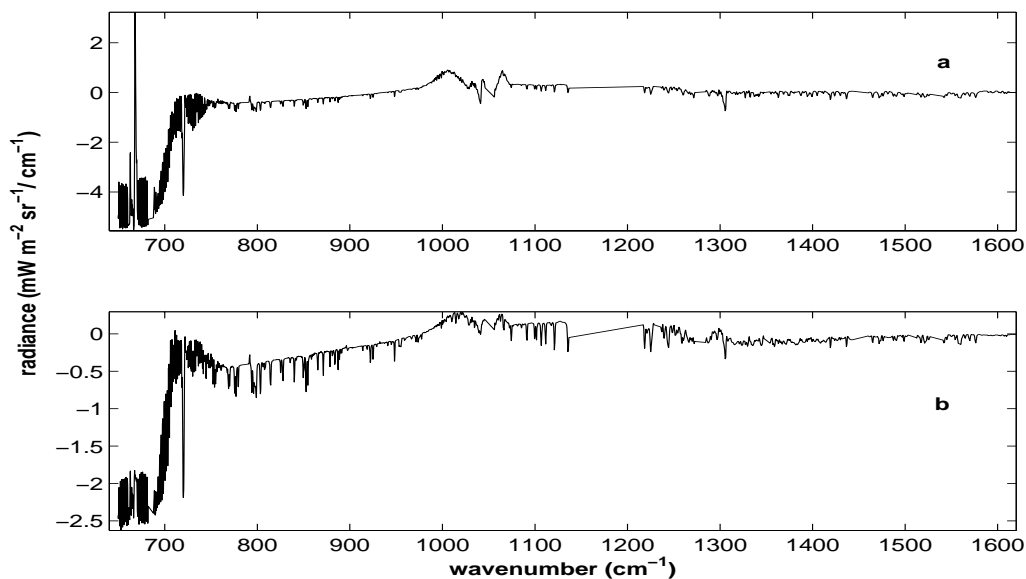


Figure 3.11 The PC2s from the spatial-spectral EOF analysis of AIRS data over January 01-16, 2003. (a) The PC2 over the NHMO. (b) The PC2 over the SHMO.

3.5 Results from CAM2 simulation

To see how well GCM can simulate these features shown in the spatial-spectral EOF analysis presented in the previous two sections, an eight-year CAM2 run with realistic SST forcing from 1996 to 2003 is carried out. The twice-per-day output from July 01-16 of 2003 is fed into MODTRAN to generate synthetic spectra and these spectra are resampled to AIRS spectral sampling points, then spatial-spectral EOF analysis is applied to these synthetic spectra.

One issue to note is that the spectral resolution of AIRS data is varying with the frequency ($\sim 0.5\text{-}1.3\text{ cm}^{-1}$ for the spectral range of interest) but MODTRAN band model generates spectra at a 1 cm^{-1} interval. We conduct a sensitivity study to investigate the effect of the different spectral resolution on the spectral EOF analysis results. First, we use spectra generated by MODTRAN at a 1 cm^{-1} interval to do the EOF analysis

(hereafter, case 1). Second, we degrade the spectra to 2 cm^{-1} resolution and apply the EOF analysis to these coarse-resolution spectra (hereafter, case 2). There is little difference between the EOF results from the two cases. If we degrade the PC1 from the case 1 to the same resolution as the spectra used in the case 2 and plot it with the PC1 from the case 2 (Figure 3.12a), they are not distinguishable. The difference between the two PC2s is also tiny (Figure 3.12b). The differences in the spatial maps of the PCs and the fractions of variance explained by the PCs between the two cases are also small. Therefore, we conclude that the different spectral resolutions between the synthetic spectra and the AIRS spectra should have little impact on the EOF analysis results.

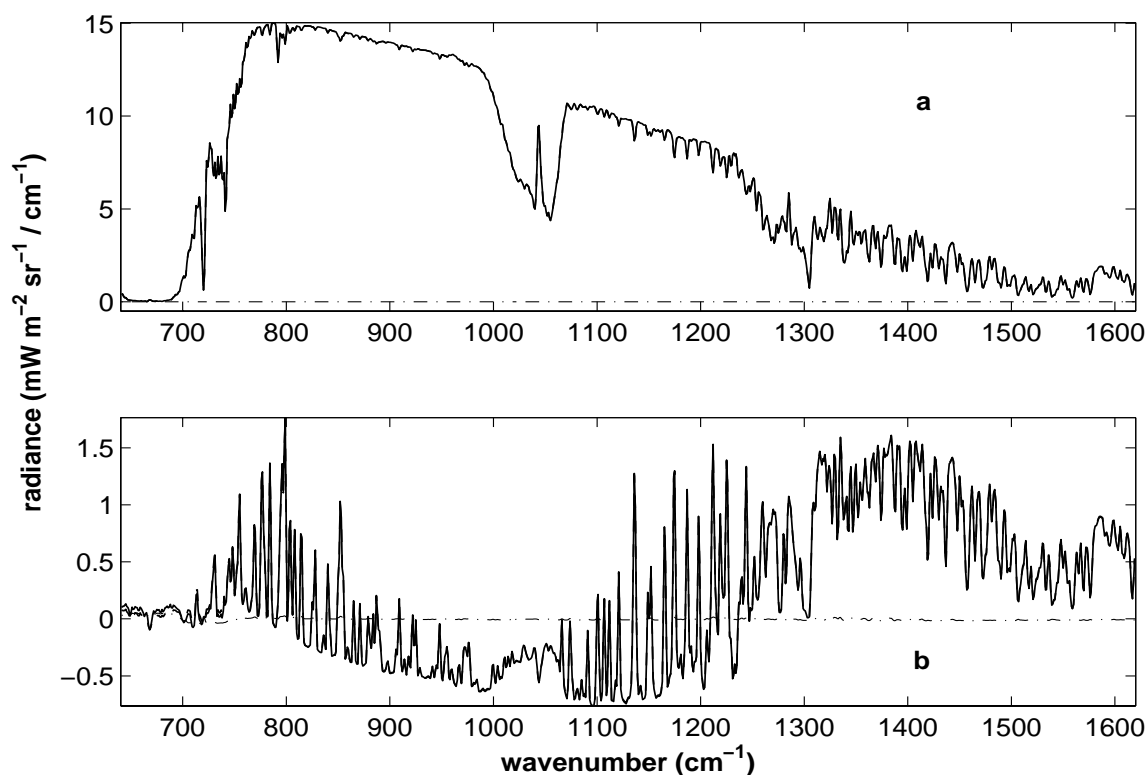


Figure 3.12 (a) The solid line is the PC1 (degraded to 2 cm^{-1} resolution) from EOF analysis to the original MODTRAN spectra, the case 1. The dash line is the PC1 from the EOF analysis to the degraded MODTRAN spectra with 2 cm^{-1} resolution, the case 2. The dash-dotted line is the difference between these two PC1s. (b) Same as (a) except for the PC2s.

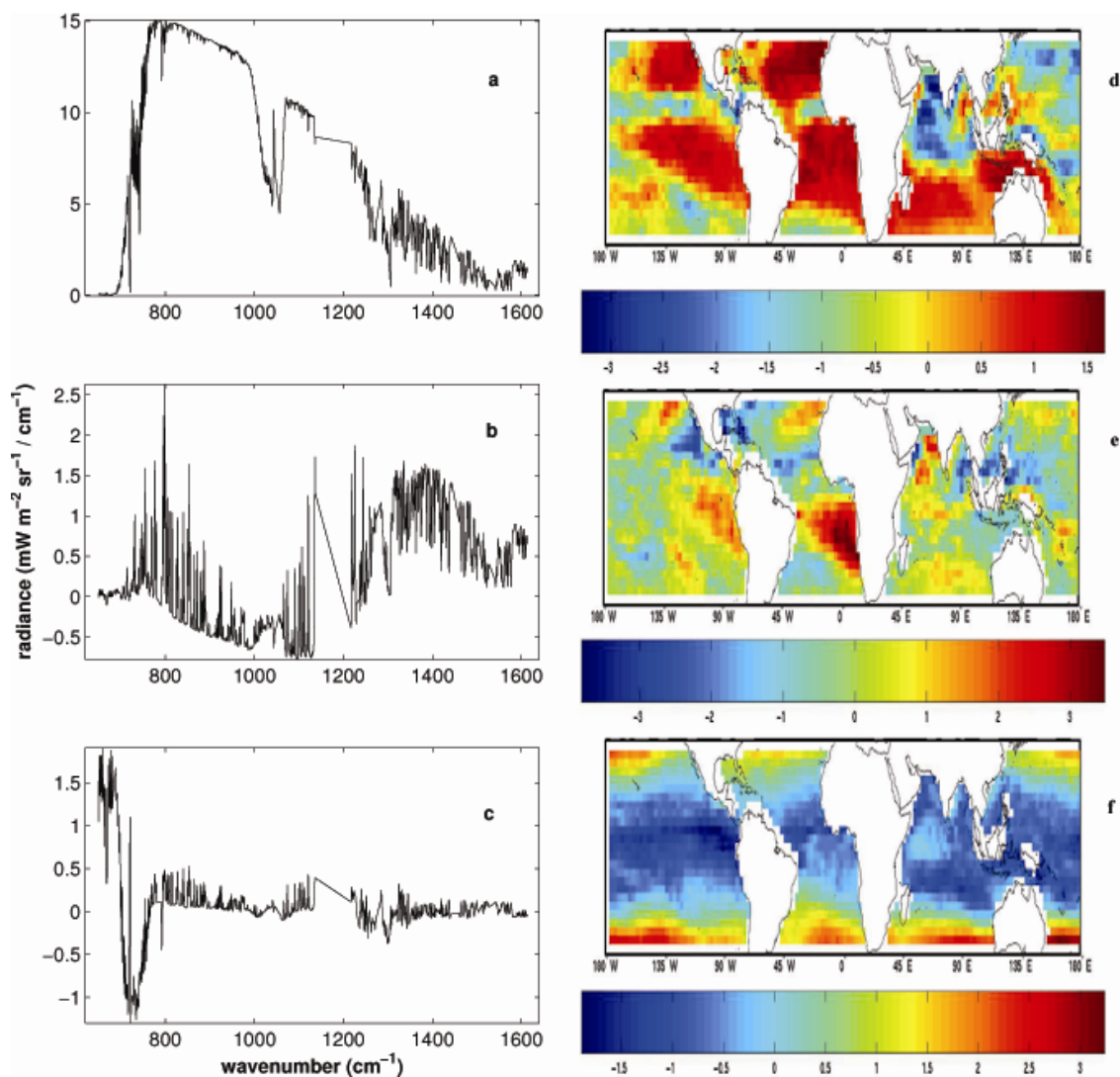


Figure 3.13 (a) The PC1 at the tropical/subtropical oceans based on the CAM2 simulation. (b) The PC2. (c) The PC3. (d) The PC1 spatial map. (e) The PC2 spatial map. (f) The PC3 spatial map.

	PC1	PC2	PC3
Tropical/subtropical oceans	98.9%	0.5%	0.3%
NHMO	98.4%	1.0%	0.3%
SHMO	96.1%	3.6%	0.2%

Table 3.3 The fraction of variance explained by three leading CAM2 PCs over climate zones examined.

3.5.1 The tropical/subtropical oceans

The three leading PCs (hereafter, CAM2 PCs) at this climate zone and their spatial maps are shown in Figure 3.13. The fraction of variance explained by each PC is listed in Table 3.3. The spectral features of these PCs agree well with those of AIRS PCs shown in Figure 3.3 except that the spectral features at the O₃ band are missing in the CAM2 PC3. The spatial maps also agree reasonably well with those derived from AIRS spectra (Figure 3.4). The major discrepancies are

(1) Between 135°E to 180°E, the CAM2 PC1 spatial map indicates little high cloud cover around the equator and substantial high cloud cover over the northern-hemisphere subtropics. In the AIRS PC1 spatial map, the situation is just the opposite. The OLR and the precipitation from NCEP reanalysis are consistent with the AIRS PC1 spatial map.

(2) The CAM2 PC1 spatial map shows a more prominent “double ITCZ” in the central Pacific than the AIRS PC1 spatial map.

(3) In the CAM2 PC2 spatial map, there are local maxima over the Arabian Sea and off the Atlantic Coast of the North Africa, comparable to the maxima at other regions known for high occurrence of low cloud. In the AIRS PC2 spatial map, there is a local minimum over the Arabian Sea and the local maximum off the Atlantic Coast of North Africa is much smaller than those maxima at other regions frequently covered by low cloud.

Apparently (1) and (2) show the deficiency of CAM2 in simulating the location of ITCZ. The latitudinal preference of ITCZ could be regulated by many physical mechanisms. The spatial distributions of SST and low-level convergences are thought to

play major roles in regulating the location of ITCZ [Bjerknes *et al.*, 1969; Holton *et al.*, 1971] and these ideas are supported by many numerical studies [Goswami *et al.*, 1984; Manabe *et al.*, 1974; Waliser and Somerville, 1994]. Recently it has been suggested that the cross-equatorial pressure gradients [Tomas and Webster, 1997] and radiative-convective instability [Raymond, 2000] could also strongly affect the location of tropical convection. In term of the simulation of ITCZ by GCMs, several studies show the high sensitivity of the latitudinal preference of ITCZ to the convection parameterization scheme used in GCMs [Chao, 2000; Chao and Chen, 2001; Hess *et al.*, 1993].

Comparing to the NCEP long-term mean of OLR (precipitation) in July, the OLR (precipitation) in July 2003 has negative (positive) anomaly over the tropical Pacific between 135°E-180°E and positive (negative) anomaly over the northern-hemisphere subtropical Pacific between 135°E-180°E (Figure 3.14a. and 3.14b). This is consistent with the AIRS PC1 spatial map: very cold emission temperature at the tropical Pacific between 135°E-180°E and warm emission temperature at the northern-hemisphere subtropical Pacific between 135°E-180°E. If we compare the OLR of July 2003 simulated by CAM2 to the long-term mean OLR of July simulated by CAM2 control run, it shows slightly positive anomaly at both regions (Figure 3.14c). This suggests that the discrepancies (1) and (2) might result from the incorrect simulation of the response of convective activities to SST anomaly, consistent with the conclusion in Section 2.3 in the previous chapter.

As for (3), the local maxima over the Arabian Sea and off the Atlantic coast of North Africa in the CAM2 PC2 spatial map overlap with the local maxima of ISCCP climatological low cloud amount in July at these two areas (Figure 3.5b). In July, dust

aerosols are usually heavily loaded in the atmosphere of these two regions with the visible optical depth around 0.4-0.8, a phenomenon seen by several satellite instruments such as AVHRR [Husar *et al.*, 1997], MODIS [King *et al.*, 2003], and TOMS [Herman *et al.*, 1997; Prospero *et al.*, 2002], as well as surface observations [Ackerman and Cox, 1989; Middleton, 1986]. Dust (both carbonate and mineral) has absorption bands in the thermal IR. In CAM2, only a uniform (both space and time) boundary layer aerosol is included. Therefore, discrepancy (3) is most likely due to the underrepresented dust aerosol in that area. Moreover, when the spectra EOF analysis is applied to AIRS data collected during January 01-16, 2003, a period with little dust aerosol over the Arabian Sea, the PC2 spatial map shows a local maximum over the Arabian Sea. This is consistent with the low cloud climatology in January. This further supports the explanation of the discrepancy (3).

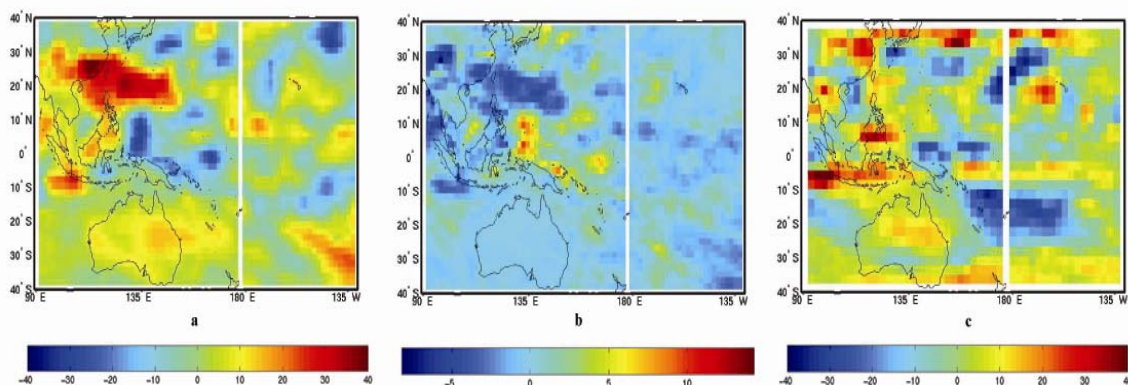


Figure 3.14 (a) The NCEP OLR anomaly of July 2003 compared to NCEP 1968-1996 climatology. (b) The NCEP precipitation rate anomaly of July 2003. (c) The CAM2 OLR anomaly of July 2003 compared to the CAM2 climatology derived from a 10-year control run. The unit of OLR is W m^{-2} and the unit of precipitation rate is $\text{kg m}^{-2} \text{s}^{-1}$.

Previous observational study [Ackerman, 1997] shows that, for the thermal IR radiances collected in the presence of a dust storm over the Arabian Sea, the brightness

temperature difference between 8 μm and 11 μm (hereafter, ΔBT_{8-11}) tends to be negative because most common elemental components of dust have maximal absorptions around 8 μm and minimal absorptions around 11 μm . In contrast, existence of low cloud (liquid water cloud) tends to make ΔBT_{8-11} positive because water has a larger absorption coefficient at 11 μm than at 8 μm [Ackerman *et al.*, 1990]. In other words, the dust aerosol and the low cloud have opposite effects on the slope of the window region. Meanwhile, several studies [Li and Ramanathan, 2002; Prospero *et al.*, 2002; Tindale and Pease, 1999] suggest that dust is transported in the middle troposphere (above 700mb) from the Arabian Peninsula to the Arabian Sea. Therefore dust aerosol is most likely above the low cloud and can be first seen from a satellite IR sounder. These facts physically explain why the heavy load of dust at the Arabian Sea in July can “smear out” the imprint of low cloud in the PC2 and even reverse it from a local maximum to a local minimum.

3.5.2 The midlatitude oceans

The fractions of variances explained by the three leading CAM2 PCs at NHMO and SHMO over the period of July 01-16 of 2003 are listed in Table 3.3. The fraction of variance explained by the CAM2 PC2 at SHMO is larger than that by the AIRS PC2 at same region by a factor of 2, indicating an unrealistic large spatial variation of the stratospheric temperature simulated by CAM2 at that region.

The CAM2 PC1s and their spatial maps over the two regions (which are not shown here) have good agreement with the AIRS counterparts. The CAM2 PC2s and their spatial maps are shown in Figure 3.15. The spatial maps have very good agreement with the AIRS counterparts (Figure 3.9a and Figure 3.9c). To a large extent, the CAM2

PC2s also have good agreement with the AIRS PC2s (Figure 3.8b and 3.8d). The major discrepancies are (1) over the NHMO, the CAM2 PC2 (Figure 3.15a) shows a larger radiance change at the CO₂ 667 cm⁻¹ band and smaller radiance changes at those weak water vapor absorption lines than AIRS PC2 (Figure 3.8b); (2) over the SHMO, the CAM2 PC2 (Figure 3.15c) shows a larger radiance change at the CO₂ 667 cm⁻¹ band than the AIRS PC2 (Figure 3.8d) by a factor of ~2. Both discrepancies disclose that the model has larger spatial variation of the midlatitude stratospheric temperature in both hemispheres than the reality.

CAM2, as well as other GCMs, is designed to simulate the general circulation in the troposphere. The stratosphere in these GCMs is usually not as well resolved as the troposphere. The top boundary of these GCMs is usually around the stratopause (~50km). Therefore, it is understandable that the stratosphere is not well simulated in such GCMs. But to what extent the unrealistic simulation of the stratosphere can be tolerated is still under debate. The stratosphere can affect the troposphere radiatively by changing the amount of solar flux that can reach the troposphere and the amount of downwelling longwave radiation emitted from the stratosphere [Forster *et al.*, 1997; Hansen *et al.*, 1997]. It can also affect the troposphere dynamically by downward propagation of zonal-mean anomalies, so-called “downward control” [Haynes *et al.*, 1991]. Recently observational [Ambaum and Hoskins, 2002; Baldwin and Dunkerton, 2001; Baldwin *et al.*, 2003; Thompson *et al.*, 2002] and modeling studies [Scott and Polvani, 2004; Shindell *et al.*, 2001; Taguchi and Yoden, 2002] increasingly demonstrate that the stratosphere is an active player in the tropospheric climate and weather. Given these facts, the deficiency of CAM2 in simulating the spatial variations of the stratospheric temperature revealed in

the comparison between the CAM2 PC2s and the AIRS PC2s might be worthy of further investigation.

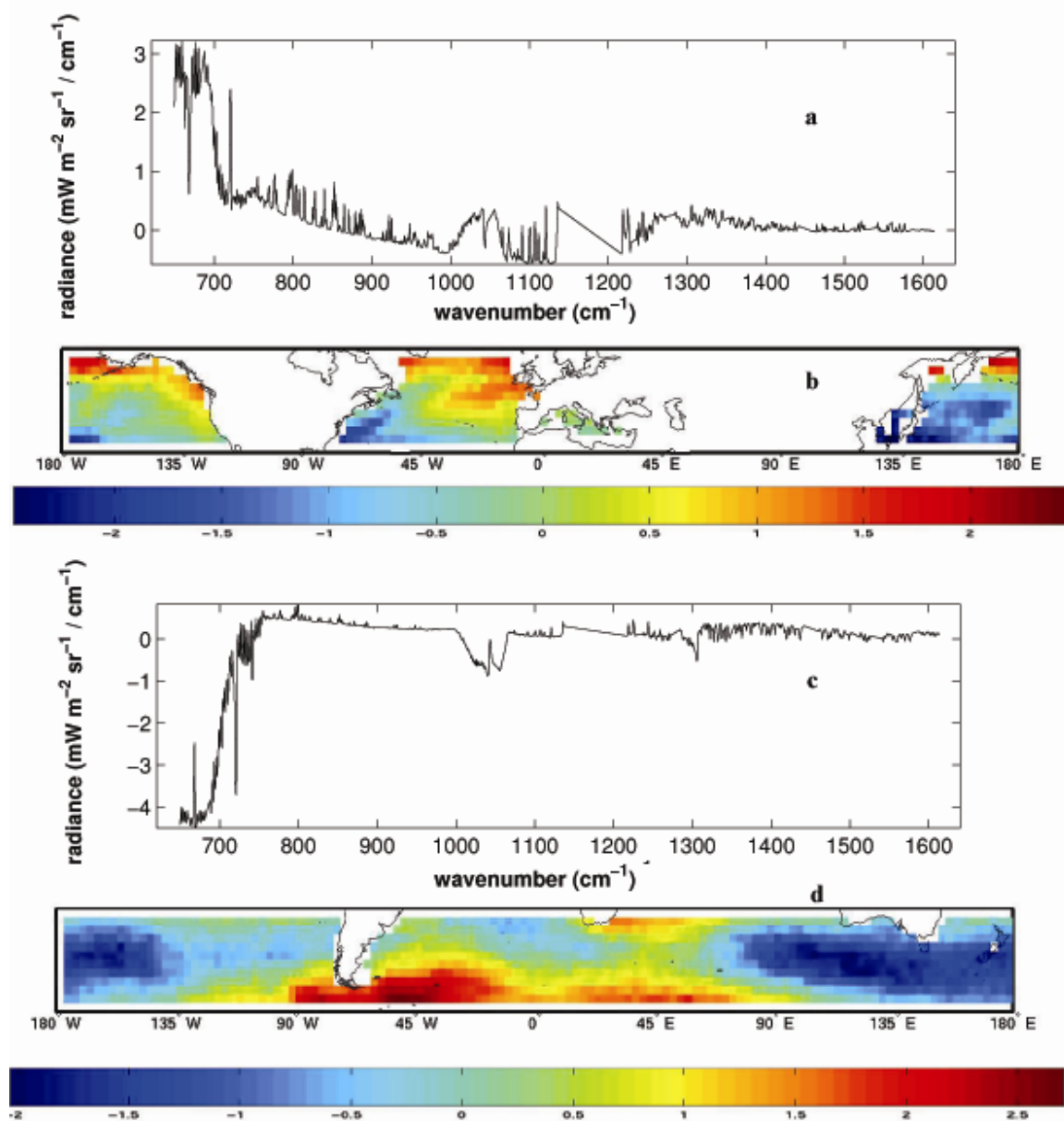


Figure 3.15 (a) The PC2 over the NHMO based on CAM2 simulation during July 01-16, 2003. (b) The spatial map of the PC2 in (a). (c) Same as (a) except over the SHMO. (d) Same as (b) except over the SHMO.

3.6 Conclusion and discussion

In this chapter, we present a survey of the spatial variability seen from AIRS data at the tropical/subtropical oceans and the midlatitude oceans and compare the results with the counterparts derived from a CAM2 simulation, with a focus on boreal summer. Although the forced orthogonality by EOF analysis makes the interpretation of the higher order PCs difficult, the three leading PCs over the tropical/subtropical oceans and the two leading PCs over the midlatitude oceans still have relatively simple interpretations by examining their spectral features and the associated spatial patterns. For all three climate zones examined, the PC1 is due to the contrast between surface temperatures and the contrast between surface temperatures and cold cloud top temperatures. The PC2s over the tropical/subtropical oceans and the summertime NHMO are mainly due to the spatial variation of the LTH and the low clouds and capture the variations in the stratosphere and the upper troposphere as well. The PC2s over the SHMO (both the wintertime and summertime) and the wintertime NHMO and the PC3 over the tropical/subtropical oceans are mainly due to the temperature variations in the upper troposphere and the lower stratosphere. The north-south contrast shown in the PC2s over the NHMO and the SHMO is mainly due to a relatively “quieter” summer troposphere in the southern hemisphere midlatitudes than in the northern hemisphere midlatitudes.

The spectral EOF results based on CAM2 simulation over the same period show generally good agreement with AIRS results. The major discrepancies are the position of ITCZ over the western Pacific and the central Pacific, the underrepresented dust aerosol over the Arabian Sea and off the Atlantic Coast of North Africa, and the overestimated spatial variations of the lower stratospheric temperature at midlatitudes. The close

connection of ITCZ with mesoscale tropical convective activities limits the capability of GCMs in realistically simulating the latitudinal preference of ITCZ. The heavy load of dust aerosol in certain regions seen from the PC2 demands a more realistic treatment of dust aerosol in the GCMs. The consistent overestimation of the stratosphere temperature changes at the midlatitudes might also need further investigation given the potential influence of the stratosphere on the tropospheric climate and weather.

The study presented in this chapter, together with the study in the previous chapter, demonstrate that various meaningful results can be obtained by looking at a single dataset, the outgoing thermal IR spectra. It is conceivable that, combined with other datasets, it would have more potential in climate studies and climate model development. This year, CLOUDSAT and AURA will join AQUA (the carrier of AIRS) as well as several other satellites to form the gorgeous A-train to observe clouds and other atmospheric variables [*Stephens et al.*, 2002]. This new epoch of satellite observations will open a new era in climate studies and the validation of climate models.

3.7 Acknowledgement

The AIRS data are obtained from GES Distributed Active Archive Center¹. The computer resources for CAM2 simulation are kindly provided by NCAR Scientific Computing Division. The author is indebted to D. Noone for learning CAM2 and G. Aumann for pointing out the 16-day orbital repeat cycle of AQUA.

¹ http://daac.gsfc.nasa.gov/data/datapool/AIRS_DP/

3.8 References

- Ackerman, S. A., Remote sensing aerosols using satellite infrared observations, *Journal of Geophysical Research-Atmospheres*, 102 (D14), 17069-17079, 1997.
- Ackerman, S. A., and S. K. Cox, Surface weather observations of atmospheric dust over the southwest summer monsoon region, *Meteorology and Atmospheric Physics*, 41 (1), 19-34, 1989.
- Ackerman, S. A., W. L. Smith, J. D. Spinhirne, and H. E. Revercomb, The 27-28 October 1986 FIRE IFO Cirrus case-study: Spectral properties of cirrus clouds in the 8-12 μm window, *Monthly Weather Review*, 118 (11), 2377-2388, 1990.
- Ambaum, M. H. P., and B. J. Hoskins, The NAO troposphere-stratosphere connection, *Journal of Climate*, 15 (14), 1969-1978, 2002.
- Aumann, H. H., M. T. Chahine, C. Gautier, M. D. Goldberg, E. Kalnay, L. M. McMillin, H. Revercomb, P. W. Rosenkranz, W. L. Smith, D. H. Staelin, L. L. Strow, and J. Susskind, AIRS/AMSU/HSB on the aqua mission: Design, science objectives, data products, and processing systems, *IEEE Transactions on Geoscience and Remote Sensing*, 41 (2), 253-264, 2003.
- Baldwin, M. P., and T. J. Dunkerton, Stratospheric harbingers of anomalous weather regimes, *Science*, 294 (5542), 581-584, 2001.
- Baldwin, M. P., D. B. Stephenson, D. W. J. Thompson, T. J. Dunkerton, A. J. Charlton, and A. O'Neill, Stratospheric memory and skill of extended-range weather forecasts, *Science*, 301 (5633), 636-640, 2003.

- Bjerknes, J., L. J. Allison, E. R. Kreins, F. A. Godshall, and G. Warnecke, Satellite mapping of Pacific tropical cloudiness, *Bulletin of the American Meteorological Society*, 50 (5), 313-&, 1969.
- Chao, W. C., Multiple quasi equilibria of the ITCZ and the origin of monsoon onset, *Journal of the Atmospheric Sciences*, 57 (5), 641-651, 2000.
- Chao, W. C., and B. D. Chen, Multiple quasi equilibria of the ITCZ and the origin of monsoon onset. Part II: Rotational ITCZ attractors, *Journal of the Atmospheric Sciences*, 58 (18), 2820-2831, 2001.
- Charney, J. G., and P. G. Drazin, Propagation of planetary scale disturbances from the lower into the upper atmosphere, *Journal of Geophysical Research*, 66, 83-109, 1961.
- Forster, P. M. D., R. S. Freckleton, and K. P. Shine, On aspects of the concept of radiative forcing, *Climate Dynamics*, 13 (7-8), 547-560, 1997.
- Gaiser, S. L., H. H. Aumann, L. L. Strow, S. E. Hannon, and M. Weiler, In-flight spectral calibration of the atmospheric infrared sounder, *IEEE Transactions on Geoscience and Remote Sensing*, 41 (2), 287-297, 2003.
- Goody, R. M., and Y. L. Yung, *Atmospheric radiation : theoretical basis*, 519 pp., Oxford University Press, New York, 1989.
- Goswami, B. N., J. Shukla, E. K. Schneider, and Y. C. Sud, Study of the dynamics of the Intertropical Convergence Zone with a symmetric version of the GLAS Climate Model, *Journal of the Atmospheric Sciences*, 41 (1), 5-19, 1984.
- Han, Q.Y., W.B. Rossow, and A.A. Lacis, Near-global survey of effective droplet radii in liquid water clouds using ISCCP data, *Journal of Climate*, 7 (4), 465-497, 1994.

- Hansen, J., M. Sato, and R. Ruedy, Radiative forcing and climate response, *Journal of Geophysical Research-Atmospheres*, 102 (D6), 6831-6864, 1997.
- Haynes, P. H., C. J. Marks, M. E. McIntyre, T. G. Shepherd, and K. P. Shine, On the downward control of extratropical diabatic circulations by eddy-induced mean zonal forces, *Journal of the Atmospheric Sciences*, 48 (4), 651-679, 1991.
- Herman, J. R., P. K. Bhartia, O. Torres, C. Hsu, C. Seftor, and E. Celarier, Global distribution of UV-absorbing aerosols from Nimbus 7/TOMS data, *Journal of Geophysical Research-Atmospheres*, 102 (D14), 16911-16922, 1997.
- Hess, P. G., D. S. Battisti, and P. J. Rasch, Maintenance of the Intertropical Convergence Zones and the large-scale tropical circulation on a water-covered earth, *Journal of the Atmospheric Sciences*, 50 (5), 691-713, 1993.
- Holton, J. R., The stratosphere and its links to the troposphere, in *Large-scale Dynamical Processes in the Atmosphere*, edited by B.J. Hoskins, and R.P. Pearce, pp. 397, Academic Press, London, 1983.
- Holton, J. T., J. M. Wallace, and J. A. Young, Boundary layer dynamics and ITCZ, *Journal of the Atmospheric Sciences*, 28 (2), 275-&, 1971.
- Houze, R. A., *Cloud Dynamics*, 573 pp., Academic Press, San Diego, 1993.
- Husar, R. B., J. M. Prospero, and L. L. Stowe, Characterization of tropospheric aerosols over the oceans with the NOAA advanced very high resolution radiometer optical thickness operational product, *Journal of Geophysical Research-Atmospheres*, 102 (D14), 16889-16909, 1997.
- Kalnay, E., M. Kanamitsu, R. Kistler, W. Collins, D. Deaven, L. Gandin, M. Iredell, S. Saha, G. White, J. Woollen, Y. Zhu, M. Chelliah, W. Ebisuzaki, W. Higgins, J.

- Janowiak, K.C. Mo, C. Ropelewski, J. Wang, A. Leetmaa, R. Reynolds, R. Jenne, and D. Joseph, The NCEP/NCAR 40-year reanalysis project, *Bulletin of the American Meteorological Society*, 77 (3), 437-471, 1996.
- King, M. D., Y. J. Kaufman, W. P. Menzel, and D. Tanre, Remote-sensing of cloud, aerosol, and water-vapor properties from the Moderate Resolution Imaging Spectrometer (MODIS), *IEEE Transactions on Geoscience and Remote Sensing*, 30 (1), 2-27, 1992.
- King, M. D., W. P. Menzel, Y. J. Kaufman, D. Tanre, B. C. Gao, S. Platnick, S. A. Ackerman, L. A. Remer, R. Pincus, and P. A. Hubanks, Cloud and aerosol properties, precipitable water, and profiles of temperature and water vapor from MODIS, *IEEE Transactions on Geoscience and Remote Sensing*, 41 (2), 442-458, 2003.
- Klein, S. A., and D. L. Hartmann, The seasonal cycle of low stratiform clouds, *Journal of Climate*, 6 (8), 1587-1606, 1993.
- Li, F., and V. Ramanathan, Winter to summer monsoon variation of aerosol optical depth over the tropical Indian Ocean, *Journal of Geophysical Research-Atmospheres*, 107 (D16), art. no.-4284, 2002.
- Manabe, S., D. G. Hahn, and J. L. Holloway, Seasonal-variation of tropical circulation as simulated by a global model of atmosphere, *Journal of the Atmospheric Sciences*, 31 (1), 43-83, 1974.
- Middleton, N. J., Dust storms in the Middle-East, *Journal of Arid Environments*, 10 (2), 83-96, 1986.

- North, G. R., T. L. Bell, R. F. Cahalan, and F. J. Moeng, Sampling errors in the estimation of Empirical Orthogonal Functions, *Monthly Weather Review*, 110 (7), 699-706, 1982.
- Pagano, T. S., H. H. Aumann, D. E. Hagan, and K. Overoye, Prelaunch and in-flight radiometric calibration of the Atmospheric Infrared Sounder (AIRS), *IEEE Transactions on Geoscience and Remote Sensing*, 41 (2), 265-273, 2003.
- Prabhakara, C., R. S. Fraser, G. Dalu, M. L. C. Wu, R. J. Curran, and T. Styles, Thin cirrus clouds - Seasonal distribution over oceans deduced from Nimbus-4 IRIS, *Journal of Applied Meteorology*, 27 (4), 379-399, 1988.
- Prospero, J. M., P. Ginoux, O. Torres, S. E. Nicholson, and T. E. Gill, Environmental characterization of global sources of atmospheric soil dust identified with the Nimbus 7 Total Ozone Mapping Spectrometer (TOMS) absorbing aerosol product, *Reviews of Geophysics*, 40 (1), art. no.-1002, 2002.
- Raymond, D. J., The Hadley circulation as a radiative-convective instability, *Journal of the Atmospheric Sciences*, 57 (9), 1286-1297, 2000.
- Rossow, W. B., and R. A. Schiffer, Advances in understanding clouds from ISCCP, *Bulletin of the American Meteorological Society*, 80 (11), 2261-2287, 1999.
- Scott, R. K., and L. M. Polvani, Stratospheric control of upward wave flux near the tropopause, *Geophysical Research Letters*, 31 (2), art. no.-L02115, 2004.
- Shindell, D. T., G. A. Schmidt, R. L. Miller, and D. Rind, Northern Hemisphere winter climate response to greenhouse gas, ozone, solar, and volcanic forcing, *Journal of Geophysical Research-Atmospheres*, 106 (D7), 7193-7210, 2001.

- Stephens, G. L., D. G. Vane, R. J. Boain, G. G. Mace, K. Sassen, Z. E. Wang, A. J. Illingworth, E. J. O'Connor, W. B. Rossow, S. L. Durden, S. D. Miller, R. T. Austin, A. Benedetti, and C. Mitrescu, The CLOUDSAT mission and the A-train: A new dimension of space-based observations of clouds and precipitation, *Bulletin of the American Meteorological Society*, 83 (12), 1771-1790, 2002.
- Taguchi, M., and S. Yoden, Internal interannual variability of the troposphere-stratosphere coupled system in a simple global circulation model. Part I: Parameter sweep experiment, *Journal of the Atmospheric Sciences*, 59 (21), 3021-3036, 2002.
- Thompson, D. W. J., M. P. Baldwin, and J. M. Wallace, Stratospheric connection to Northern Hemisphere wintertime weather: Implications for prediction, *Journal of Climate*, 15 (12), 1421-1428, 2002.
- Tindale, N. W., and P. P. Pease, Aerosols over the Arabian Sea: Atmospheric transport pathways and concentrations of dust and sea salt, *Deep-Sea Research Part II-Topical Studies in Oceanography*, 46 (8-9), 1577-1595, 1999.
- Tomas, R. A., and P. J. Webster, The role of inertial instability in determining the location and strength of near-equatorial convection, *Quarterly Journal of the Royal Meteorological Society*, 123 (542), 1445-1482, 1997.
- Waliser, D. E., and C. Gautier, A satellite-derived climatology of the ITCZ, *Journal of Climate*, 6 (11), 2162-2174, 1993.
- Waliser, D. E., and R. C. J. Somerville, Preferred latitudes of the Intertropical Convergence Zone, *Journal of the Atmospheric Sciences*, 51 (12), 1619-1639, 1994.

Wilber, A.C., D.P. Kratz, and S.K. Gupta, Surface emissivity maps for use in satellite retrievals of longwave radiation, pp. 35, NASA, 1999.

Chapter 4: The spatial and temporal variability of the Martian outgoing thermal IR spectra seen from MGS-TES data

Xianglei Huang, Junjun Liu, Yuk L. Yung

*Division of Geological and Planetary Sciences, California Institute of
Technology, Pasadena, CA 91125*

The majority of this chapter, together with Chapter 6, was published in:

Huang, X.L., J.J. Liu, and Y. L. Yung, Analysis of Thermal Emission Spectrometer Data
Using Spectral EOF and Tri-spectral Methods, *Icarus*, 165(2), pp.301-314, October 2003

4.1 Abstract

As a comparative study to the previous two chapters, here we present a study of the variability in the Martian outgoing thermal IR spectra using MGS-TES data. The case study with TES 20°S -20°N data shows that, for both the spatial-spectral and the temporal-spectral EOF analysis, the first principal component (PC1) dominates the total variance and is associated with surface or near-surface brightness temperature variations. The PC2 of the spatial-spectral EOF analysis is associated with atmospheric variability mainly caused by the topography, and a negative correlation between dust and ice absorptions can be clearly seen over many regions. The annual cycle is a major component of the PC1 temporal patterns. The negative correlation between dust and ice absorption can also be seen in the PC2 of the temporal-spectral EOF analysis. The fingerprint of the dust storm can be clearly seen in the PC2 temporal patterns in most areas except the highlands.

4.2 Introduction and data manipulation

Unlike the Earth's atmosphere in which the major gases (N_2 , O_2 , Ar) are all lack of infrared vibration or rotation spectra, the major gas of the Martian atmosphere, CO_2 , has two fundamental bands and several overtone bands at thermal IR. But on the other hand, the Martian atmosphere is more transparent than our atmosphere. Except for several CO_2 bands, weak water vapor lines, spectral features related to occasional water ice clouds and dust storms, the emission from the Martian surface can be observed over wide spectral ranges. For our Earth, the surface emission can only be seen in the three window regions ($\sim 800\text{-}1000\text{ cm}^{-1}$, $1080\text{-}1240\text{ cm}^{-1}$, and $2500\text{-}2800\text{ cm}^{-1}$) because of the wide range of water vapor absorption and the absorptions from other greenhouse gases. Another important difference is the larger topography contrast on the Mars than the Earth which makes the variations of CO_2 column abundance from the lowlands to the highland not negligible.

The Thermal Emission Spectrometer (TES) aboard the Mars Global Surveyor (MGS) spacecraft was designed to study the Martian surface and atmosphere using thermal infrared emission spectroscopy [*Christensen et al.*, 2001]. It has a Michelson interferometer to obtain spectra from 200 to 1650 cm^{-1} with 5 or 10 cm^{-1} resolution. For a typical spectrum sampled around local 2PM, the signal to noise ratio (SNR) is about 350 at the mid-point of the spectrum and degrades to less than 100 at the endpoints. The interferometer has six detectors arranged in a 3 by 2 array, each with an instantaneous field of view (FOV) of 8 mrad , corresponding to 3 km from the 380 km orbit of MGS. Two versions of the processed TES data are available online. Version 1 covers March

1999 to March 2001 (no data during solar conjunction). Version 2 covers April 2001 to January 2002.

The TES data provide an unprecedented resource for studying the thermal emission from Mars [Bandfield *et al.*, 2000; Pearl *et al.*, 2001; Smith *et al.*, 2002; Smith *et al.*, 2001]. Sophisticated retrieval algorithms have been developed by the TES team to retrieve surface as well as atmospheric properties [Conrath *et al.*, 2000; Smith *et al.*, 2000a; Smith *et al.*, 2000b]. Meanwhile, factor analysis has also been applied to TES data to recover the atmospheric dust and water-ice cloud spectra shapes (Bandfield *et al.*, 2000b).

Here, we analyze TES data using the same technique used in the Chapter 2 and Chapter 3 to disclose the variability seen from the Martian outgoing thermal IR spectra. We will focus on the tropical region (20°S-20°N) and the period from solar longitude (hereafter, Ls) 104° of the first MGS mapping year to Ls 99° of the second MGS mapping year (TES data volume mgst0100 to mgst0214). We use 10 cm⁻¹ data sampled around 2PM by all 6 detectors with emission angle less than 10°. Since the SNR gradually decreases toward both ends of the spectra, we use only the radiances from 265 to 1538 cm⁻¹ in 117 spectral bins. This range contains the major Martian emission and absorption features. Because of the asynoptic sampling patterns of the sun-synchronous satellite, it is more meaningful to apply spectral EOF to the ensemble-averaged spectra over certain periods and regions than to apply directly it to all observed spectra. We do the temporal average over every 10° solar longitudes beginning at Ls=100° and the spatial average over every 10° latitude by 20° longitude box. As a result, we have averaged spectra over 72 spatial bins and 36 temporal bins. For a given time interval (a temporal bin over 10°

Ls), we can apply spatial-spectral EOF analysis to these spectra averaged over different spatial bins. Similarly, for a given area (a spatial bin over 10° latitude by 20° longitude box), we can apply temporal-spectral EOF analysis to the 36 spectra, one for each of the temporal bins. To ensure the statistical significance of the ensemble average, we discard any temporal bins in which the total number of spectra is less than 1000. Thus, for example, in all spatial bins, the temporal bin 10° - 20° Ls in the second MGS mapping year is discarded because of solar conjunction.

4.3 The spatial-spectral variability seen from TES tropical data

We study the spectral EOFs and their associated spatial patterns in three different periods: 110 - 120° Ls, 230 - 240° Ls and 350 - 360° Ls of the first MGS mapping year. They correspond to northern hemisphere summer, southern hemisphere summer (also a dust storm period), and northern hemisphere spring, respectively. The first two principal components (hereafter, PC1 and PC2) over each period are presented in Figure 4.1. The associated spatial patterns (the normalized ECs) are presented in Figure 4.2. The fractions of total variance explained by the PC1s and the PC2s are summarized in Table 4.1. It can be seen from Table 4.1 that for all three periods the bulk of the variance (over 90%) is explained by PC1. Compared with the mean spectrum, the PC1 over 110 - 120° Ls (Figure 4.1a) corresponds to around 6.5K brightness temperature change over all frequencies except at the CO_2 strong absorption band. The corresponding brightness temperature change is very close to zero at the CO_2 strong absorption band center (667cm^{-1}) and monotonically increases to 6.5K in each wing of this band. Such a spectral shape shows that this PC1 is strongly related to surface brightness temperature change. The associated spatial pattern (Figure 4.2a) shows higher temperatures in the northern tropics and lower

temperatures in the southern tropics. Such a pattern is typical for northern hemisphere summer. For 230-240°Ls, the shape of PC1 shows that it is closely related to the surface brightness temperature change. The corresponding surface brightness temperature change is around 10 K. The associated spatial pattern (Figure 4.2c) also clearly shows the temperature contrast between northern and southern tropics. For 350-360°Ls, the brightness temperature change corresponding to the PC1 is 4 K over all frequencies except the CO₂ strong absorption band. Inside the CO₂ strong absorption band, the corresponding brightness temperature change is zero at the line center, reaches the maximum value (6 K) near 610 and 700 cm⁻¹, and then gradually decreases to 4 K in the far wing regions. Based on the contribution functions of TES in nadir-view [Conrath *et al.*, 2000], the radiances at 610 and 700cm⁻¹ are most sensitive to the temperature changes in the planetary boundary layer (PBL) and the lower atmosphere layer just above the PBL. Therefore, this PC1 is related more to variations in the PBL and the lower atmosphere layer just above the PBL than to the surface temperature changes. Since this period is close to the vernal equinox, the temperature contrast between north and south is not obvious in the associated spatial patterns. Instead, we see some wave-like pattern (Figure 4. 2e).

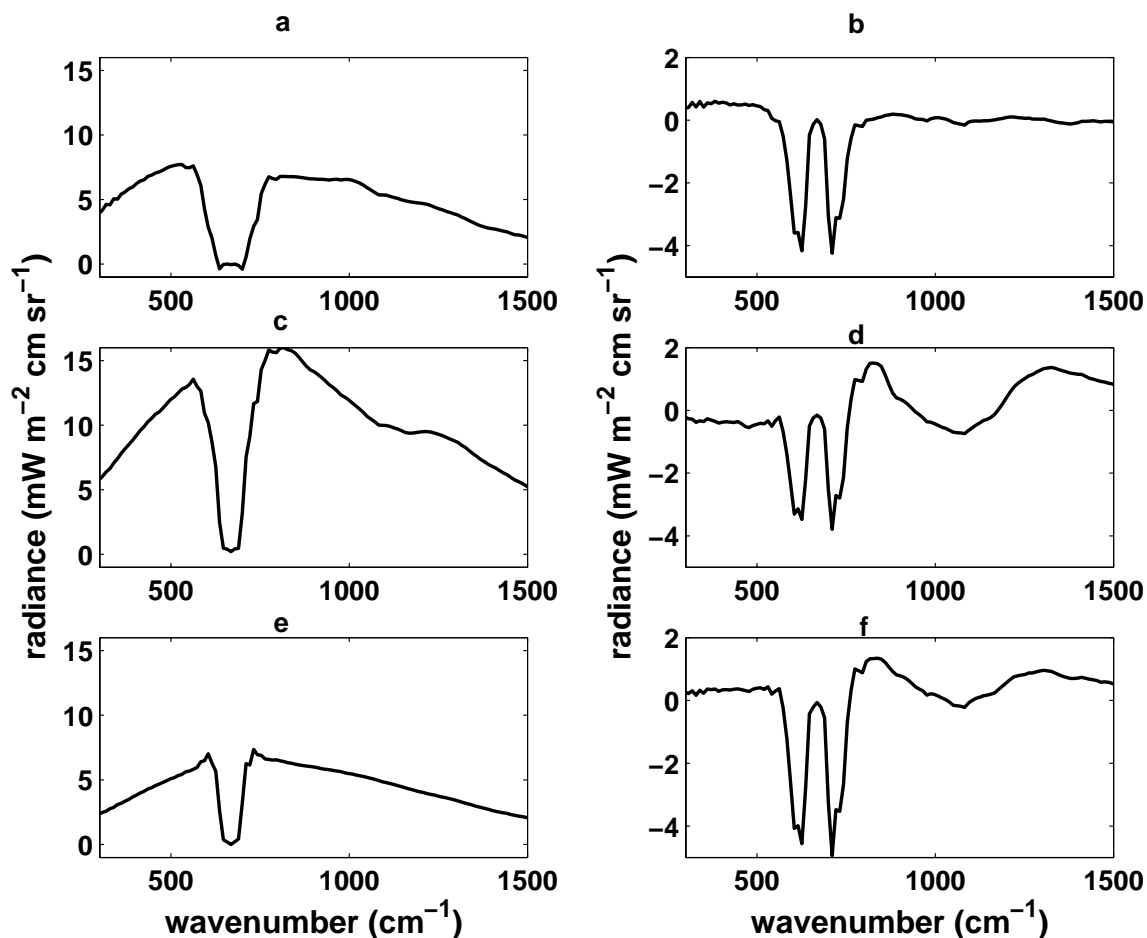


Figure 4.1 (a) The PC1 derived from spectra averaged over 10° latitude by 20° longitude bins during $110\text{-}120^\circ\text{Ls}$ of the first MGS mapping year. The spatial coverage is from 20°S to 20°N . (b) Same as (a) except that it is PC2. (c) Same as (a) except that the period is $230\text{-}240^\circ\text{Ls}$ of the first MGS mapping year. (d) Same as (c) except that it is. (e) Same as (a) except that the period is $350\text{-}360^\circ\text{Ls}$ of the first MGS mapping. (f) Same as (e) except that it is PC2.

	PC1	PC2
$110\text{-}120^\circ\text{Ls}$	93.3%	3.5%
$230\text{-}240^\circ\text{Ls}$	98.5%	1.2%
$350\text{-}360^\circ\text{Ls}$	91.3%	6.3%

Table 4.1 Summary of the fraction of total variance explained by PC1s and PC2s obtained from the spectral EOF analysis over $20^\circ\text{S}\text{-}20^\circ\text{N}$ band for three different periods in the first MGS mapping year

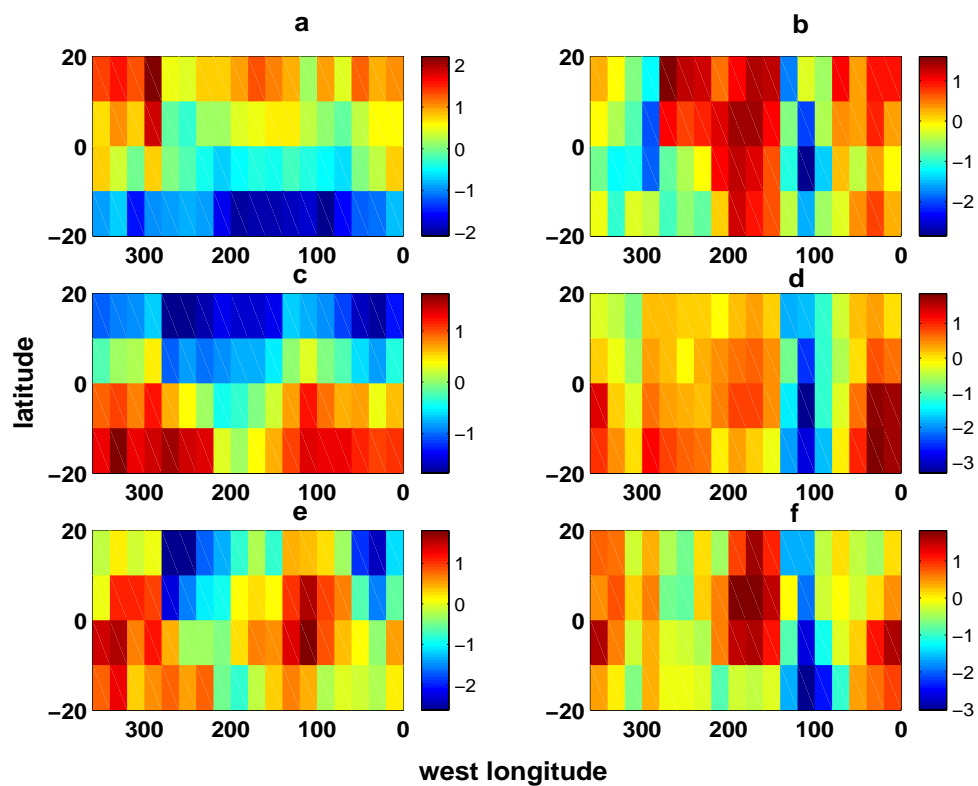


Figure 4.2 (a) - (f) are the spatial patterns associated with the principal components shown in Figure 4.1(a) - (f), respectively.

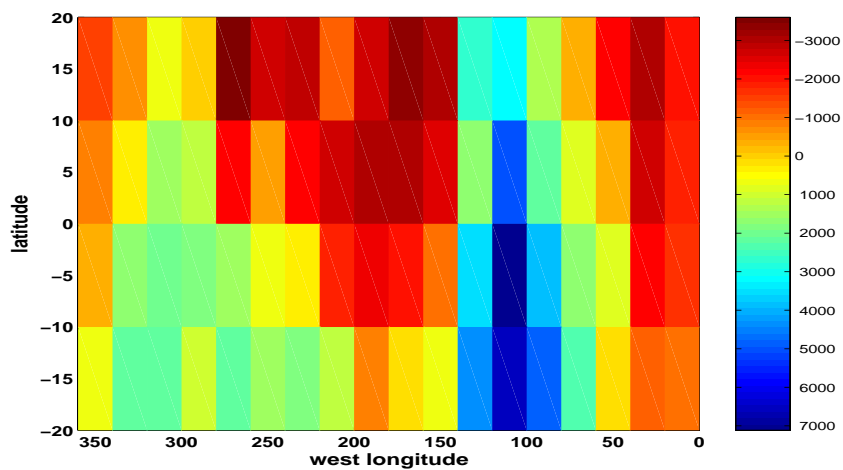


Figure 4.3 Topography of Mars smoothed over 10° latitude by 20° longitude spatial bin from 20°S to 20°N . The elevation unit is meters.

The PC2 is flat and close to zero during 110-120°Ls (Figure 4.1b), except in the CO₂ absorption band. Inside the CO₂ band, it has two minima at 625 and 710 cm⁻¹. Based on the contribution functions of TES in nadir-view [Conrath *et al.*, 2000], the maxima of the contribution functions at these two frequencies occur around 5mb (2km above the datum). The spatial pattern of this PC2 (Figure 4.2b) is well correlated with topography (see Figure 4.3), negative in the highlands and positive in the lowlands. This can be understood in terms of the variation of the CO₂ path length due to topography. The total path length of CO₂ in the lowlands is longer than that in the highlands. This has little effect on CO₂ band center where the CO₂ opacity is already very large. This has also little effect outside CO₂ band because no CO₂ absorption occurs there. In the wing regions of the band, this has a big effect because the CO₂ opacity there is small and the radiances in these regions are sensitive to the path length changes in the lower atmosphere. Therefore, we see two minima at 625 and 710 cm⁻¹ and the spatial pattern resembles topography: positive values in the lowlands (Figure 4.2b) represent more CO₂ absorption than the average and negative values in the highlands represent less CO₂ absorption than the average. For the PC2 during 230-240°Ls (Figure 4.1d), two troughs in the CO₂ band are still present, while the most striking differences from the previous PC2 are the local minimum at the dust absorption band (~1100 cm⁻¹) and local maximum at the ice absorption band (~800 cm⁻¹). The spatial pattern of this PC2 is also well correlated with topography (Figure 4.3): negative values in the highlands and positive values in the lowlands. Given the spectral characteristics of the PC2, the negative values over certain spatial bins indicate that there are more ice absorptions and less CO₂ and dust absorption in these bins than in the average over all areas. The positive values over certain spatial

bins mean CO₂ and dust absorptions in these bins are stronger than the average over all areas and ice absorptions in these bins are weaker than the average over all areas. The argument about the variation of the CO₂ path length still holds for this PC2 and associated spatial pattern. Moreover, the correlation between the spatial pattern of the PC2 and Martian topography is also consistent with previous knowledge that tropical water-ice clouds are usually observed in the highlands [Zurek *et al.*, 1992] and dust opacity is highly correlated with topography (large dust opacity in the lowlands and small dust opacity in the highlands). The dust and ice features can still be seen in PC2 over 350-360°Ls with a smaller amplitude than over 230-240° Ls, because the former is a period after a dust storm. The spatial pattern (Figure 4.2f) is well correlated with topography as described above.

4.4 The temporal-spectral variability seen from TES tropical data

Next, as we described in the Section 4.1, we choose certain spatial bins and apply spectral EOF to time averaged spectra to study the temporal behavior of the outgoing spectra. The first spatial bin is from 10°S to 0° S and 100°-120° west. This is a highland region (the Tharsis region including the flanks of Arsia Mons and Pavonis Mons) with surface elevation varying from 6km to 10km. The results are summarized in Figure 4.4 and Figure 4.5. The fractions of total variance explained by the two leading principal components are summarized in Table 2. The PC1 (Figure 4.4a) is dominant and accounts for over 99% of the total variance. The spectral shape of the PC1 shows that it is related to surface brightness temperature variations. It corresponds to 12K brightness temperature change. The PC1 time series (Figure 4.4b) shows an annual cycle with amplitude of 2.5 (corresponding to 30K) with maximum occurring at 305°Ls. These are

consistent with the time series of the averaged target temperature shown in Figure 4.4c. The target temperature is a quantity provided by the TES team, roughly equivalent to the surface temperature in nadir-view mode. The PC2 (Figure 4.5a) is still related to atmospheric temperature and aerosol variations. Again, the ice and dust absorption features are negatively correlated. The PC2 time series (Figure 4.5b) shows that the largest negative value (corresponding to strong dust absorption) occurs around 235°Ls. This is consistent with the knowledge that the two largest dust storms in the first MGS mapping year occurred between 225°Ls and 245°Ls [Pearl *et al.*, 2001]. There is another trough around 345°Ls, which is consistent with previous observations that a moderate regional dust storm near the equator began at 321°Ls and lasted for over a month [Pearl *et al.*, 2001].

The second spatial bin that we choose is 0-10°N and 180-200° west. This is a lowland region with surface elevation varying from -3.5km to -2.5km. As in the previous case, the PC1 (Figure 4.4d) is dominant. The time series of PC1 (Figure 4.4e) clearly contains an annual cycle component. But two local minima can be seen around the dust storm peak periods. The time series agrees very well with the time series of the averaged target temperature (Figure 4.4f). The PC2 shows negative correlation between ice and dust absorptions (Figure 4.5c), and local minima related to dust storms are also clearly seen in its time series (Figure 4.5d). For both spatial bins, PC3 (not shown here) accounts for no more than 1% of the total variance and still contains dust and ice absorption features. Just as in PC2s, the dust and ice absorption features show negative correlation in PC3s.

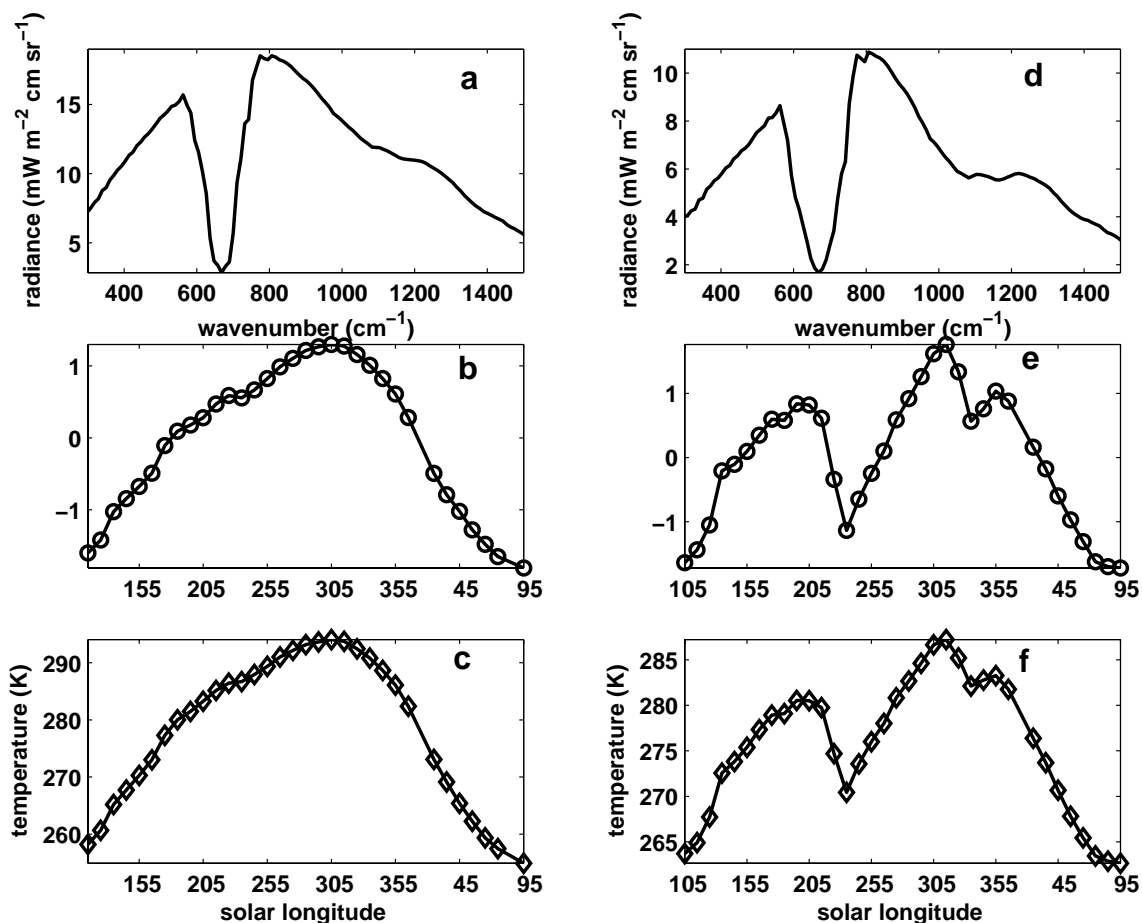


Figure 4.4 (a) The PC1 derived from spectra averaged over the area of 10°- 0° S and 100-120° west longitude and 10°Ls bins from 104°Ls of the first MGS mapping year to 99°Ls of the second MGS mapping year. (b) The time series associated with the PC1 in (a). (c) The time series of the average target-temperature (a quantity provided in TES product) over the same area as (a). (d) Same as (a), except that it is over 0-10°N and 180-200° west longitude. (e) The time series associated with the PC1 in (d). (f) The time series of the average target-temperature over the same area as (d).

	PC1	PC2
10-0°S, 100-120°west longitude	99.2%	0.4%
0-10°N, 180-200°west longitude	94.5%	4.2%

Table 4.2 Summary of the fraction of total variance explained by PC1s and PC2s obtained from the spectral EOF analysis for two different regions. The temporal coverage is from 104° Ls of the first MGS mapping year to 99° Ls of the second MGS mapping year.

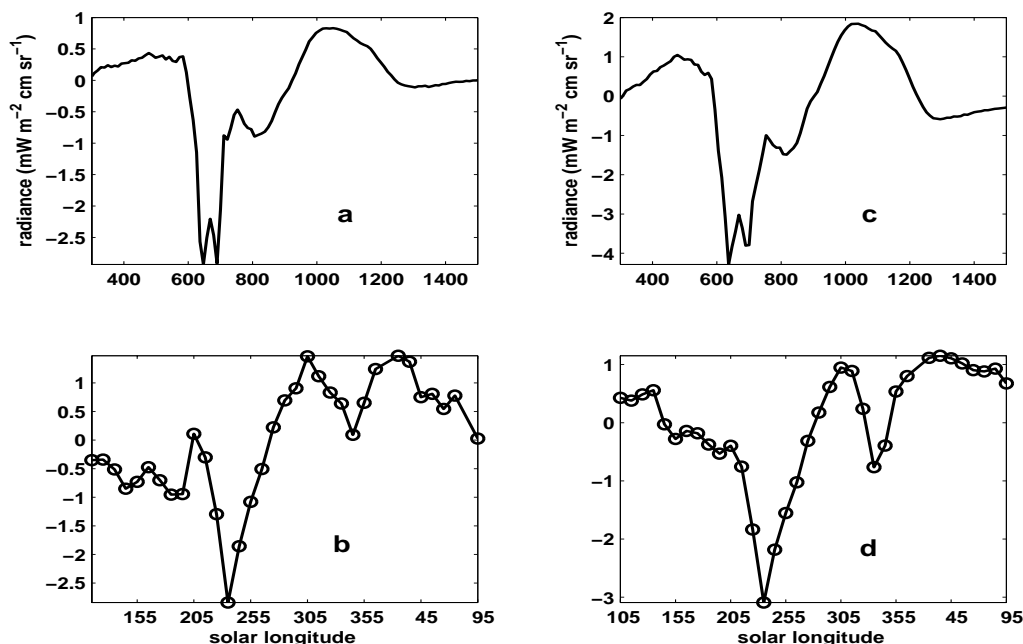


Figure 4.5 (a) Same as Figure 4.4a except that it is PC2. (b) The time series associated with the PC2 in (a). (c) Same as Figure 4.4d except that it is PC2. (d) The time series associated with the PC2 in (c).

For the above spectral EOF analysis, given the dominance of PC1s in explaining the total variance, the significance of PC2s may be questioned. But the spectral shapes of PC2s show certain realistic physical features. The time series and the spatial patterns of PC2s are consistent with our previous knowledge. Moreover, similar spectral shapes for PC2 and similar time series are seen in most spatial bins that we have looked at. Therefore, we conclude that the temporal and spatial patterns of PC2s are physically meaningful.

4.5 Summary

In this paper, we try to show the potential of spectral EOF in analyzing data like those from TES and comparing them with GCM simulations in the future. Using a case study of TES data from 10°S to 10°N for almost one Martian year, we show that the PC1 is related to the surface or near-surface brightness temperature variations while the PC2 is related more to the changes of CO_2 and dust opacities, which are correlated with

topography. The negative correlations between ice and dust absorption features in PC2s seen in EOF studies over many different regions and periods suggest that, to some extent, ice and dust are mutually exclusive in the atmosphere. When spectral EOF analysis is performed over different regions, the PC1 spatial pattern shows the temperature contrast between summer and winter hemispheres while the PC2 spatial pattern is correlated with topography. When spectral EOF analysis is performed over different periods, the annual cycle is clearly seen in the PC1 time series. The PC2 time series shows its minimum around the dust storm peak period. These spectral EOF results can be compared with their counterparts from Martian GCM simulations to test the variability of the model. Such comparisons would be valuable because the information contained in the spectra might help to identify the reason for any discrepancy between observations and modeling.

An interesting spectral EOF result is the negative correlation between dust and ice absorption. Physically it is possible. For example, when water-ice clouds are present in the atmosphere first and dusts appear later, the strong solar absorption effect of dust could heat the atmosphere [*Gierasch and Goody, 1972; Zurek et al., 1992*], leading to the sublimation of water ice. When dusts are present in the atmosphere first and water vapor in the air reaches the saturation level, heterogeneous nucleation over dust is a more efficient way to form water-ice cloud than homogeneous nucleation over ice itself. As a result, dust would be coated by ice or scavenged by aggregation and precipitation. A recent modeling study by Rodin *et al.* [*Rodin et al., 1999*] showed that when the interaction between radiation transfer, microphysics of the Martian atmosphere aerosols, and eddy transport are included in the model, the feedback due to water ice cloud formation may affect the dust and temperature vertical profiles within several days. How

dust and ice may be mutually exclusive in the Martian atmosphere is an interesting question and worth further exploration.

4.6 Acknowledgement

We thank S. Byrne, M. Gerstell, A. Ingersoll, and M. Richardson for helpful discussions. We are greatly indebted to M. Richardson for his help in accessing TES data. We also thank two referees, including J. L. Bandfield for greatly improving the paper. This research was supported by NASA grant NAGS-10724 to the California Institute of Technology.

4.7 References

- Bandfield, J. L., V. E. Hamilton, and P. R. Christensen, A global view of Martian surface compositions from MGS-TES, *Science*, 287 (5458), 1626-1630, 2000.
- Christensen, P.R., J. L. Bandfield, V. E. Hamilton, S. W. Ruff, H. H. Kieffer, T. N. Titus, M. C. Malin, R. V. Morris, M. D. Lane, R. L. Clark, B. M. Jakosky, M. T. Mellon, J. C. Pearl, B. J. Conrath, M.D. Smith, R. T. Clancy, R. O. Kuzmin, T. Roush, G. L. Mehall, N. Gorelick, K. Bender, K. Murray, S. Dason, E. Greene, S. Silverman, and M. Greenfield, Mars Global Surveyor Thermal Emission Spectrometer experiment: Investigation description and surface science results, *Journal of Geophysical Research-Planets*, 106 (E10), 23823-23871, 2001.
- Conrath, B. J., J. C. Pearl, M. D. Smith, W. C. Maguire, P. R. Christensen, S. Dason, and M.S. Kaelberer, Mars Global Surveyor Thermal Emission Spectrometer (TES) observations: Atmospheric temperatures during aerobraking and science phasing, *Journal of Geophysical Research-Planets*, 105 (E4), 9509-9519, 2000.

- Gierasch, P. J., and R. M. Goody, Effect of dust on temperature of Martian atmosphere, *Journal of the Atmospheric Sciences*, 29 (2), 400-410, 1972.
- Pearl, J. C., M. D. Smith, B. J. Conrath, J. L. Bandfield, and P. R. Christensen, Observations of Martian ice clouds by the Mars Global Surveyor Thermal Emission Spectrometer: The first Martian year, *Journal of Geophysical Research-Planets*, 106 (E6), 12325-12338, 2001.
- Rodin, A. V., R. T. Clancy, and R. J. Wilson, Dynamical properties of Mars water ice clouds and their interactions with atmospheric dust and radiation, in *Planetary Atmospheres*, pp. 1577-1585, 1999.
- Smith, M. D., J. L. Bandfield, and P. R. Christensen, Separation of atmospheric and surface spectral features in Mars Global Surveyor Thermal Emission Spectrometer (TES) spectra, *Journal of Geophysical Research-Planets*, 105 (E4), 9589-9607, 2000a.
- Smith, M. D., R. J. Conrath, J. C. Pearl, and P. R. Christensen, Thermal Emission Spectrometer observations of Martian planet-encircling dust storm 2001A, *Icarus*, 157 (1), 259-263, 2002.
- Smith, M. D., J. C. Pearl, B. J. Conrath, and P. R. Christensen, Mars Global Surveyor Thermal Emission Spectrometer (TES) observations of dust opacity during aerobraking and science phasing, *Journal of Geophysical Research-Planets*, 105 (E4), 9539-9552, 2000b.
- Smith, M. D., J. C. Pearl, B. J. Conrath, and P. R. Christensen, Thermal Emission Spectrometer results: Mars atmospheric thermal structure and aerosol distribution, *Journal of Geophysical Research-Planets*, 106 (E10), 23929-23945, 2001.

Zurek, R. W., J.R. Barnes, R. Haberle, J. B. Pollack, J. E. Tillman, and C. Leovy,
Dynamics of the atmosphere of Mars, in *MARS*, edited by H. H. Kieffer, B. M.
Jakosky, C. W. Snyder, and M. S. Matthews, pp. 860, The University of Arizona
Press, Tucson & London, 1992.

Part II: The detection of cirrus/dust aerosol from the thermal IR spectra

Chapter 5: High-resolution thermal IR detection and characterization of cirrus from the retrieval point of view

Xianglei Huang¹, Yuk L. Yung¹, Jack S. Margolis²

*1. Division of Geological and Planetary Sciences, California Institute of
Technology, Pasadena, CA 91125*

2. Remote Sensing Analysis Systems, Inc., Pasadena, CA 91001

This chapter was published in:

Huang, X.L., Y.L. Yung, J.S. Margolis, Use of High-Resolution Measurements for the Retrieval of Temperature and Gas-Concentration Profiles from Outgoing Infrared Spectra in the Presence of Cirrus Clouds, *Applied Optics*, 42(12), pp. 2155-2165, April 2003.

5.1 Abstract

We explore how high spectral resolution measurements could aid the retrieval of atmospheric temperature and gas concentration profiles from outgoing IR spectra when optically thin cirrus is present. Simulated outgoing spectra, containing cirrus, are fitted with spectra not containing cirrus and the residuals are examined. For those lines with weighting functions peaking around the same altitude as the thin cirrus, unique features are observed in the residuals. These unique features are very sensitive to the resolution of the instrumental line shape (ILS). For thin cirrus these residual features are narrow ($\leq 0.1 \text{ cm}^{-1}$) so high spectral resolution is required for unambiguous observation. The magnitudes of these unique features are larger than the noise of modern instruments. The sensitivities of these features to cloud height and cloud optical depth are also discussed. Our sensitivity studies show that when the errors in the estimation of temperature profiles are not very large, the dominant contribution to the residuals is the misinterpretation of cirrus. An analysis from the point of view of the information content is also presented. An understanding of the magnitude of the effect and the dependence on spectral resolution as well as spectral region is important for retrieving spacecraft data and designing future infrared instruments for weather forecasting and greenhouse gases monitoring.

5.2 Introduction

In the last two decades, atmospheric measurements from NOAA polar orbiting satellite systems, such as measurements by MSU (the Microwave Sounding Unit) and HIRS (the High-resolution Infrared Sounder) on TOVS (the Television and Infrared Observation Satellite (TIROS)-N Operational Vertical Sounder) [Smith *et al.*, 1979] have been extensively assimilated into operational Numerical Weather Prediction (NWP) models. In 1987, after evaluating the impact of the first ten years of such measurements on NWP accuracy, the World Meteorological Organization (WMO) concluded that significantly improving NWP would require global temperature and moisture soundings with radiosonde accuracy [WMO, 1987]. That is equivalent to temperature profiles with 1K accuracy in 1 km thick layers and humidity profiles with 10% accuracy in the troposphere. To achieve these requirements, a high spectral resolution infrared sounder with high signal to noise ratio (SNR) is needed. Meanwhile, the precise monitoring of the greenhouse gases and their interaction with other gases in the troposphere requires an even higher spectral resolution infrared sounder to resolve absorption lines. As a result, in this decade, several high spectral resolution infrared sounders will be in operation, such as AIRS (the Atmospheric Infrared Sounder) [Aumann and Pagano, 1994], TES (the Tropospheric Emission Spectrometer) [Beer *et al.*, 2001] and IASI (the Infrared Atmospheric Sounding Interferometer) [Diebel *et al.*, 1997].

In order to achieve the goals mentioned above, at least two subtasks must be successfully performed. The first one is to design and build such high spectral resolution infrared sounder with the required SNR and spectral coverage. The second is to develop an effective retrieval algorithm to invert the observed spectra. In reality, cloud is one of

the most difficult problems standing in the way of the second subtask. The atmosphere below an optically thick cloud is invisible to a nadir viewing sounder. Optically thin clouds or patchy clouds also interfere with the retrieval effort. Therefore, we must identify cloud signatures from spectra and retrieve relevant quantities from cloudy spectra.

One brute force approach to the retrieval of cloudy spectra is to simultaneously retrieve temperature and humidity profiles, as well as cloud properties, such as cloud top and cloud optical depth using a radiative transfer model including scattering. However, this approach would require tremendous computational power because multiple scattering has to be taken into account. Moreover, retrieving geophysical parameters even from clear-sky spectra is often an ill-posed problem. To include cloud parameters in the retrieval list will make the retrieval problem more complicated and, most likely, increase the non-linearity of the problem. Therefore, if we could identify cloudy spectra and obtain some *a priori* information about the clouds from the spectra, it would facilitate the retrieval effort of cloudy spectra and simplify the computations in those instances when scattering is not effectively present.

A widely used method to detect and retrieve cirrus from infrared spectra is the tri-spectral technique [Ackerman *et al.*, 1990; Takano *et al.*, 1992]. The basic idea behind this technique is that both ice and liquid water absorb strongly in the infrared window region (8-12 μm) but they peak at different frequencies. Meanwhile, a weak absorption water-vapor band is also presented in the window region. As a result, it is possible to discriminate cirrus, liquid water cloud and clear sky by the brightness temperature differences (ΔBT) between different bands (e.g., $\Delta\text{BT}_{8\mu\text{m}-11\mu\text{m}}$ versus $\Delta\text{BT}_{11\mu\text{m}-12\mu\text{m}}$ are

widely used) in a scatter-plot. Also, Hutchison *et al.* [1999; 1996; 1995] conducted a series of studies to show how to use NOAA's AVHRR (Advanced Very High Resolution Radiometer) and other coincident measurements to detect optically thin cirrus. They used the brightness temperature differences between AVHRR channel 3 (3.7 μm) and channel 5 (12 μm) with information of total integrated water vapor to detect optically thin cirrus clouds in nighttime AVHRR measurements [Hutchison *et al.*, 1995]. With the help of coincident 1.38 μm imagery from AVIRIS (Airborne Visible/Infrared Imaging Spectrometer), they demonstrated how to detect thin cirrus from daytime AVHRR image over land surfaces [Hutchison and Choe, 1996]. With imagery from the recent launched AVHRR/3 and information from HIRS, they also developed an algorithm to detect thin cirrus and specific cloud-top phase [Hutchison, 1999]. All above techniques are narrowband approaches, where high spectral resolution is not necessary. Moreover, to apply these techniques, measurements at certain specified spectral ranges must be taken. When the resolution is high enough to resolve the individual absorption lines, the information content is much greater than that of narrowband measurements. As a result, it might be possible to detect cirrus even when measurements are not taken at above specified spectral ranges. Several researchers are exploring how to extract useful information about cloud from high spectral resolution measurements. Turner and Ackerman [2002] explored the possibility to determine cloud phase by using downwelling brightness temperature at 9, 12 and 18 μm measured by ground-based AERI (the Atmospheric Emitted Radiance Interferometer). Ackerman *et al.* [2002] also studied cloud retrieval using upwelling radiance observed by HIS (the High-spectral resolution Infrared Sounder). Bantges *et al.* [1999] used statistical approaches to explore the

possible best combinations of spectral ranges for the retrieval of cirrus cloud optical properties from the next generation spaceborne high-resolution spectrometer such as IASI. A statistical approach is also used by Schlüssel and Goldberg [2002] to study the retrieval of temperature and humidity profiles from future IASI measurements in partly cloudy situations.

In this paper, we concentrate on optically thin cirrus clouds (optical depth of cloud ~ 0.1 or even less, hereafter, thin cirrus) clouds. From the retrieval point of view, we explore the possibility of using the information in the high-resolution spectra to extract some information about cirrus clouds. Cirrus clouds regularly cover about 13% of the globe [*Rossow and Schiffer, 1999*]. Therefore, the probability of obtaining a spectrum contaminated by cirrus is not low. Meanwhile, thin cirrus clouds usually affect the brightness temperature in the window region only up to several degrees. As a result, sometimes the effect of thin cirrus is misinterpreted as the effect of surface emission and this misinterpretation further misleads the retrieval process. So it is meaningful to explore the issue of thin cirrus.

In Section 5.3, we use a simplified three-layer model to demonstrate that a cloud can have different “spectral signatures” in different absorption lines and elucidate the physics of the process. In Section 5.4, by applying a line-by-line radiative transfer model with multiple scattering to standard model atmospheric profiles, we show that the expected “spectral signatures” for cirrus can also be seen. Sensitivity studies are also presented Section 5.4. Additional concerns about the “spectral signatures” for realistic retrievals will be discussed in Section 5.5. A summary is given in Section 5.6.



Figure 5.1 Schematic of three-layer atmosphere model. The surface temperature is T_s . The temperatures of three layers (from top to bottom) are T_T , T_m , T_s respectively. The optical depth at the interface between top layer and middle layer is τ_2 . The optical depth at the interface between middle layer and bottom layer is τ_1 . The optical depth at the surface is τ_0 .

5.3 A simplified analytic model

Here we use a simplified model to show what “spectral signatures” thin cirrus would leave in the residual spectra if thin cirrus spectra were misinterpreted as clear-sky spectra.

Consider a three-layer atmosphere with the planet’s surface and the bottom layer at the same temperature T_s ; the temperature for the middle layer is T_m and that for the top layer is T_T . The corresponding blackbody emissions for these three layers are B_s , B_m , and B_T respectively. We denote the optical depth at the surface by τ_0 , at the interface between bottom and middle layer by τ_1 and at the interface between middle and top layer by τ_2 . Figure 5.1 is a schematic plot of this three-layer atmosphere. The radiative transfer equation in a plane parallel atmosphere in the absence of scattering is given by

$$\mu \frac{dI(\nu)}{d\tau} = I(\nu) - B(\nu) \quad (5.1)$$

where $\mu = \cos\theta$ and θ is the zenith angle, $B(\nu)$ is the blackbody emission at frequency ν . Solving (1) with our three-layer atmosphere configuration for the radiance at the top of atmosphere at zero zenith angle, we obtain

$$\begin{aligned} I_{TOA}(\nu) &= B_s(\nu) \exp(-\tau_0(\nu)) - \int_0^{\tau_2(\nu)} B_T(\nu) \exp(-\tau) d\tau \\ &\quad - \int_{\tau_2(\nu)}^{\tau_1(\nu)} B_m(\nu) \exp(-\tau) d\tau - \int_{\tau_1(\nu)}^{\tau_0(\nu)} B_s(\nu) \exp(-\tau) d\tau \\ &= B_s(\nu) \exp(-\tau_1(\nu)) + B_m(\nu) [\exp(-\tau_2(\nu)) - \exp(-\tau_1(\nu))] \\ &\quad + B_T(\nu) [1 - \exp(-\tau_2(\nu))] \end{aligned} \quad (5.2)$$

Also assuming that the mixing ratio of the absorbing gas is uniform in all layers and the same Lorentz line shape is applied to all layers for analytical simplicity, we have

$$\tau_2(\nu - \nu_0) = \rho H_T S_T \frac{\alpha_L}{\pi[(\nu - \nu_0)^2 + \alpha_L^2]} \quad (5.3)$$

where ν_0 is the frequency at the center of the absorption line, ρ is the density of the absorption gas, H_T is the vertical thickness of top layer, S_T is the line strength for the top layer, and α_L is the half-width of the Lorentz line shape for the top layer. Define $x = (\nu - \nu_0) / \alpha_L$ and rewrite (3) as

$$\tau_2(x) = \frac{C_2}{x^2 + 1} \quad (5.4)$$

where the constant $C_2 = \rho H_T S(\alpha_L \pi)^{-1}$. If we assume the change of α_L from layer to layer is negligible, then τ_1 can be expressed as

$$\begin{aligned}\tau_1(x) &= \rho H_T S_T \frac{\alpha_L}{\pi[(v-v_0)^2 + \alpha_L^2]} + \rho H_m S_m \frac{\alpha_L}{\pi[(v-v_0)^2 + \alpha_L^2]} \\ &= \frac{C_1}{x^2 + 1}\end{aligned}\quad (5.5)$$

where H_m is the thickness of the middle layer and S_m is the line strength for the middle layer. Clearly, we always have $C_1 > C_2$. Similarly, we have $\tau_0(x) = C_0/(x^2 + 1)$ where $C_0 > C_1$.

Now we assume there is a thin cirrus cloud in the middle layer and only cloud absorption is considered. For any single absorption line, the cloud optical depth varies little from the center of line to the wing of the line. Therefore, we can assume the cloud optical depth τ_c is independent of x . Given that the Planck function also varies very slowly from the wing to the center of the line, we can also assume B_s, B_m, B_T are not dependent on x . The radiance at the top of atmosphere at zero zenith angle is now given by

$$I_{TOA}(x) = \exp(-\tau_c) \left\{ B_s \exp\left(-\frac{C_1}{x^2 + 1}\right) + B_m \left[\exp\left(-\frac{C_2}{x^2 + 1}\right) - \exp\left(-\frac{C_1}{x^2 + 1}\right) \right] \right\} + B_T \left[1 - \exp\left(-\frac{C_2}{x^2 + 1}\right) \right] \quad (5.6)$$

Let us designate the regions that are located at the far wings of any absorption lines and transparent to the surface emission as “micro window regions”. In these regions, when cloud is present, we have $I_{TOA} \approx \exp(-\tau_c) B_s$.

Now let us examine the case of a thin cirrus cloud for which $\tau_c \ll 1$ holds. If in the retrieval we misinterpret the radiances in micro window regions as if they are measured under the clear-sky situation, then we obtain an incorrect surface emission B'_s

$$B'_s = B_s \exp(-\tau_c) \quad (5.7)$$

Substituting (5.7) back into (5.1), we get

$$I'_{TOA}(x) = B_s \exp(-\tau_c) \exp\left(-\frac{C_1}{x^2+1}\right) + B_m \left[\exp\left(-\frac{C_2}{x^2+1}\right) - \exp\left(-\frac{C_1}{x^2+1}\right) \right] + B_T \left[1 - \exp\left(-\frac{C_2}{x^2+1}\right) \right] \quad (5.8)$$

So the difference between the “retrieved” radiance (5.8) and the real radiance (5.6) is

$$R(x) = I'_{TOA} - I_{TOA} = [1 - \exp(-\tau_c)] B_m \left[\exp\left(-\frac{C_2}{x^2+1}\right) - \exp\left(-\frac{C_1}{x^2+1}\right) \right] \propto L(x) \quad (5.9)$$

where

$$L(x) = \left[\exp\left(-\frac{C_2}{x^2+1}\right) - \exp\left(-\frac{C_1}{x^2+1}\right) \right] \quad (5.10)$$

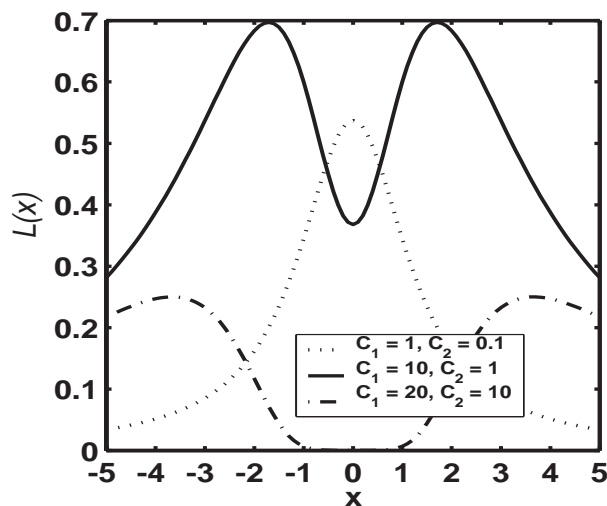


Figure 5.2. Plots of $L(x) = \exp\left(-\frac{C_2}{x^2+1}\right) - \exp\left(-\frac{C_1}{x^2+1}\right)$ with three different combinations of C_2 and C_1 . Here $x=0$ is the line center; $x=1$ corresponds to the half width of the Lorentz line shape. The dotted line corresponds to a case of weak absorption. The solid and dash-dotted lines correspond to cases of medium and very strong absorptions, respectively.

Figure 5.2 shows how the shape of $L(x)$ changes with respect to different combinations of C_1 and C_2 . For a case of weak absorption (Figure 5.2 dotted line), $L(x)$ has one upward pointing peak centered at the line center. For a case of medium absorption (Figure 5.2 solid line), $L(x)$ has two peaks symmetrical to the line center and one narrow valley. For a case of very strong absorption (Figure 5.2 dash-dotted line), $L(x)$ has a broad valley centered at the line center. These results can be understood in terms of the weighting functions [Goody and Yung, 1989]. We know the peak of the weighting function for nadir viewing is approximately located at the altitude where $\tau \approx 1$. So, for the weak absorption case, the peak of the weighting functions of the line center is in the bottom layer and close to the surface. As a result, when the change of surface temperature makes the same contribution to the micro window as the cirrus in the middle layer, the contribution of surface temperature change to absorption at line center is larger than the contribution of the cirrus in the middle layer. So the difference at the line center is positive and the difference decreases from center to wing. For the very strong absorption case, the weighting function of the line center peaks somewhere much higher than the cirrus and the surface. Therefore, the absorption at the line center is insensitive to both cloud in the middle layer and the surface temperature change, so the difference around the center is almost zero. For the medium absorption case, the weighting function of the line center peaks at the altitude close to the cloud height. Therefore the difference shows a “transition” shape from the shape of weak absorption to that of very strong absorption.

From above discussion, we schematically show that if we misinterpret thin cirrus as clear sky, then for different absorption lines the shapes of the residuals are significantly different. When the weighting function is peaked at an altitude similar to the

cloud height, the residual will show a narrow feature (referred as unique feature in the abstract). This leads us to investigate the possibility of using the residual spectra to detect and obtain some information about thin cirrus and feed such information back to the retrieval process.

Although the above schematic model is illustrative of the method, it is too simple for realistic retrieval. In next section, we use a much more realistic radiative transfer model and temperature/trace gas profiles to study this problem.

5.4 Line-by-line model and sensitivity studies

We use our own Line-By-Line Code for Atmospheric Radiative Transfer with Scattering (LBLCARTS) to study the spectral signatures of cirrus clouds in the high-resolution spectra. It is a line-by-line radiative transfer model coupled with the DISORT [Stamnes *et al.*, 1988] code (version 1.3)¹ for multiple scattering. 16 streams are used in DISORT. A Voigt line profile is used in LBLCARTS and the molecular spectroscopy properties are taken from HITRAN 2K [Rothman *et al.*, 1998]. Our LBLCARTS has been calibrated against FASCODE 3P [Wang *et al.*, 1996] for the clear-sky calculation. The differences between these two models are less than 1%. As for the cloud, we assume the modified gamma distribution for the cirrus particle size distribution. Then, based on the spectral-dependent reflection index of ice compiled by Warren [1984], we calculate the optical properties of cirrus using a Mie scattering code [Hansen and Travis, 1974]. The temperature profile used in LBLCARTS is taken from US 1976 standard atmosphere

¹ DISORT version 1.3 was released in March 2000 and can be obtained from ftp://climate.gsfc.nasa.gov/pub/wiscombe/Multiple_Scatt/

profile up to 60 km [Anderson *et al.*, 1986] in 57 layers. For all the calculations, we assume a surface albedo of 0.02 and a constant CO₂ mass mixing ratio of 5.0×10^{-4} .

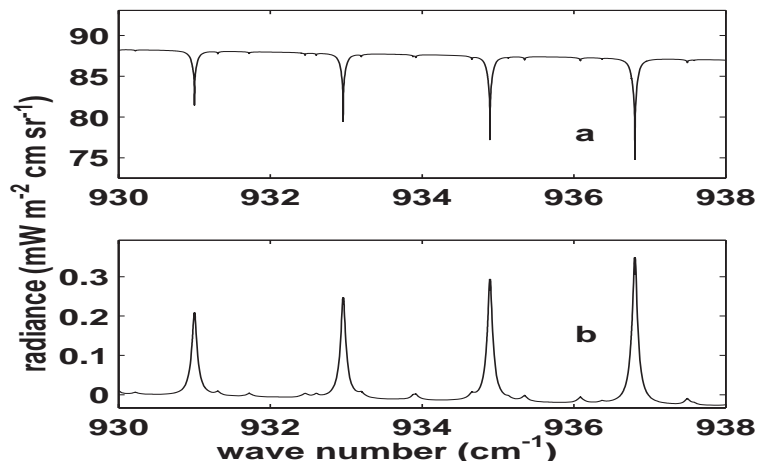


Figure 5.3 (a) Simulated outgoing spectrum from 930 to 938 cm^{-1} based on following configuration: temperature profile of US 1976 standard atmosphere, the constant mass mixing ratio of CO₂ $r_{\text{CO}_2} = 5.0 \times 10^{-4}$; cirrus cloud with optical depth 0.1 topping at 250mb. The spectrum is calculated from LBLCARTS. (b) The difference of adjusted-surface-temperature spectrum and cirrus spectrum (hereafter, the residual spectrum) shown in (a). Refer to the text for the meaning of the adjusted-surface-temperature spectrum.

Our approach is first to specify a small amount of cirrus cloud at certain levels and calculate the spectra at the top of atmosphere with zero zenith angle. Then we adjust the surface temperature, keep temperatures at other levels unchanged, and repeat the calculation for clear sky. The criterion for adjusting the surface temperature is to let the radiances in the micro window around $11 \mu\text{m}$ be the same as those derived from the cirrus calculation. Then we take the difference of these two spectra to obtain the residual spectra. Figure 5.3a is the spectrum at 930-938 cm^{-1} when thin cirrus with optical depth 0.1 is present at 250mb. There are several weak CO₂ absorption lines in this region. Figure 5.3b is difference between thin cirrus spectrum and clear sky spectrum with

adjusted surface temperature (hereafter, the residual spectrum) at $930\text{-}938\text{ cm}^{-1}$. It can be seen that after the adjustment the baseline of thin cirrus spectrum and clear-sky spectrum are the same and the shape of the residual for weak absorption line is consistent with what we obtain in Figure 5.2 (dotted line). The solid line in Figure 5.4b shows the residual spectrum at $744\text{-}748\text{ cm}^{-1}$. There are several CO_2 medium absorption lines in this region. It can be seen that narrow feature of the residual for medium absorption line is also consistent with what we obtain in Figure 5.2 (solid line).

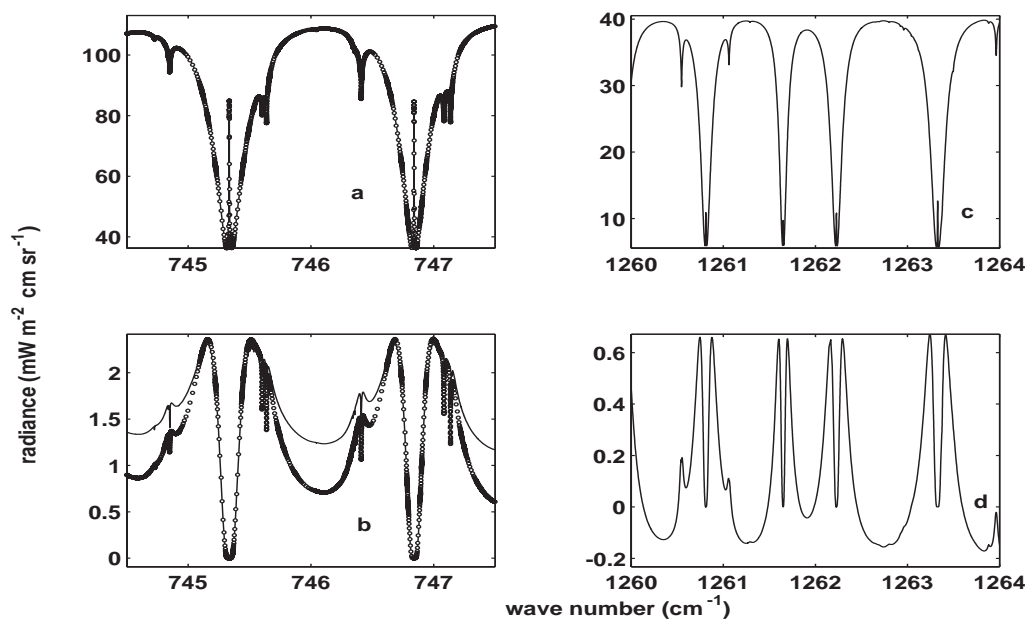


Figure 5.4 (a) Same as Figure 3(a) except the region is from 744 to 748 cm^{-1} . For the solid line, ice particles are assumed to be spherical and the optical properties are computed using Mie scattering theory. For the curve denoted by circles, the ice particles are assumed to be hexagonal and optical properties compiled by Baran *et al.*²⁴ are used. (b) Same as Figure 3(b), except the region is from 744 to 748 cm^{-1} . The solid line and the line denoted by circles have same meanings as they are in (a). (c) The simulated outgoing spectrum from 1260 to 1270 cm^{-1} based on following configuration: temperature profile of US 1976 standard atmosphere, the CH_4 profile of US 1976 standard atmosphere; cirrus cloud with optical depth 0.1 topping around 250mb . (d) The difference of adjusted-surface-temperature spectrum and cirrus spectrum shown in (c).

As we demonstrated in Section 5.3, the narrow feature is due to the misinterpretation of cirrus and it is associated with gas medium absorption lines. Therefore, it can be expected that under the influence of gas medium absorption, the specific angular scattering distribution of thin cirrus should have little contribution to the narrow feature. To test this idea, we conduct another calculation assuming the shape of ice particle is hexagonal instead of spherical. The single-scattering properties of hexagonal ice columns compiled by Baran *et al.* [2002] are used. The results are given by the line with circles in Figures 5.4a and 5.4b. It can be seen from the residual spectra in Figure 5.4b that the difference between two shape assumptions is significant only for the region between the two absorption lines. The reason is that the gas absorption is weak there, and the thin cirrus has more contribution to the radiance in this region. But in the line-core region, the difference between hexagonal and spherical particles is small and the amplitudes of the narrow features are almost same. Given this fact, although realistic assumptions about particle shapes should be made in the operational retrieval, for simplicity we will still use the spherical particle assumption in our following sensitivity study.

To see how these concepts work for non-uniformly mixed gases, we carry out modeling with absorption by methane, which is not uniformly distributed. The results are presented in Figures 5.4c and 5.4d. We use the methane profile from US 1976 standard atmosphere [Anderson *et al.*, 1986]. Cirrus is still present at 250mb with optical depth 0.1. It can be seen that for methane lines whose weighting functions have maximum values near the tropopause, similar narrow features can be seen in the residual spectra. We can see that, even for the very thin cirrus cloud with an optical depth of 0.1, the amplitudes of

the narrow features in the residual spectra (Figures 5.4b and 5.4d) are about 2% of the unperturbed radiances (Figure 5.4a and 5.4c). Given the potential SNR of modern high-resolution infrared sounders, residuals with such amplitudes are expected to be much larger than instrument noise. Therefore, this narrow feature in residual spectra can be seen at appropriate absorption lines of different trace gases and its amplitude is detectable with modern instrument.

In real measurements, we can obtain only spectra with limited resolution. It can be imagined that when resolution is low enough, the narrow feature in the residual spectra will be smoothed out. We investigate this by taking the difference after convolving the LBL spectra with different hypothetical ILS's that have different FWHM (full width of half maximum). We use a triangle function as ILS and apply three different FWHM, 0.04cm^{-1} , 0.1cm^{-1} , and 0.5cm^{-1} . The results for CO_2 lines from 742 cm^{-1} to 752 cm^{-1} are shown in Figure 5.5. It can be seen that the narrow features in the residual are clear for the cases of $\text{FWHM} = 0.04\text{ cm}^{-1}$ and $\text{FWHM} = 0.1\text{ cm}^{-1}$. As the FWHM degrades to 0.5 cm^{-1} , the narrow features are barely identified. When we convolve methane spectra shown in Figure 5.4 with above ILS's, we obtain a similar conclusion. Therefore, the narrow features in the residual are very sensitive to the instrumental resolution.

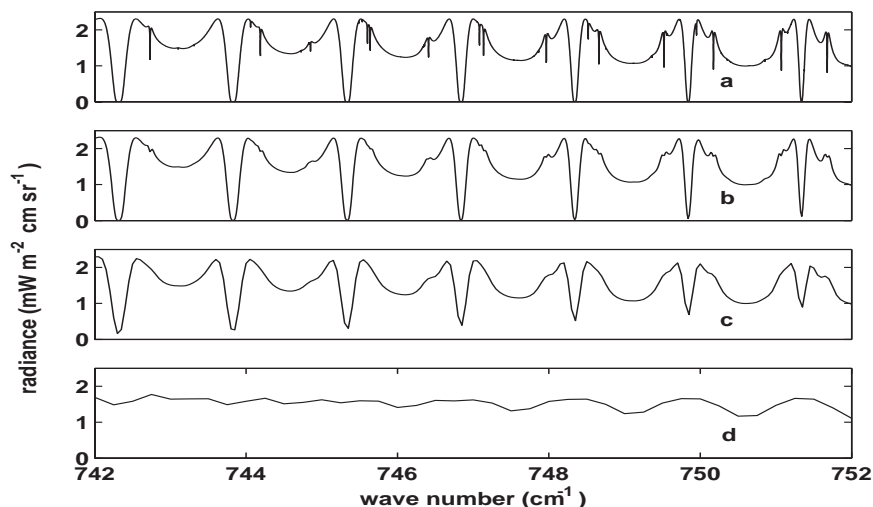


Figure 5.5 (a) Same as the solid line in Figure 4(b), except the region is from 742 to 752 cm^{-1} . (b) The convolution of spectrum in (a) and a triangular function with full width of half maximum $\text{FWHM} = 0.04 \text{ cm}^{-1}$. (c) Same as (b), except $\text{FWHM} = 0.1 \text{ cm}^{-1}$. (d) Same as (b), except $\text{FWHM} = 0.5 \text{ cm}^{-1}$.

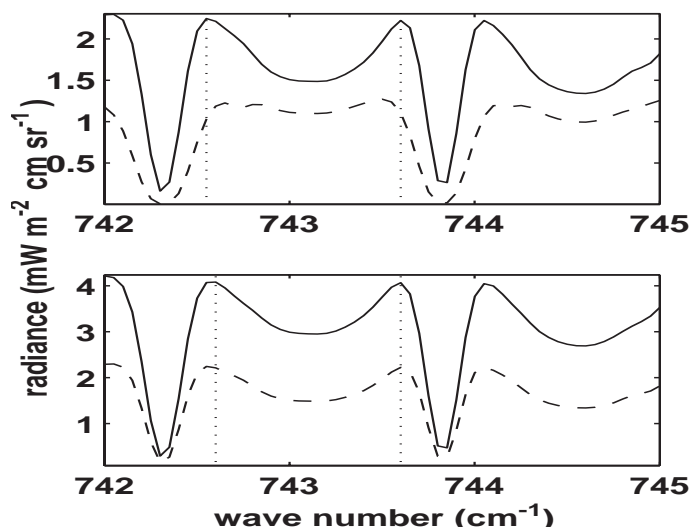


Figure 5.6 (a) The solid line is the residual spectrum from 742-745 cm^{-1} when the top of cirrus is at 250mb. The dash line is the residual spectrum from 742-745 cm^{-1} when the top of cirrus is at 450mb. For both cases, the cloud optical depth is 0.1. The spectra shown here are convolved with a triangular function with $\text{FWHM} = 0.1 \text{ cm}^{-1}$. (b) The solid line is the residual spectrum from 742-745 cm^{-1} with cloud optical depth $\tau_{\text{cloud}} = 0.2$. The dash line is the residual spectrum from 742-745 cm^{-1} with cloud optical depth $\tau_{\text{cloud}} = 0.1$. For both cases, the cloud top is at 250mb. The spectra shown here are convolved with a triangular function with $\text{FWHM} = 0.1 \text{ cm}^{-1}$.

For the above discussions, the cirrus top is assumed to be at 250mb and the optical depth is 0.1. Now we investigate the sensitivity of the residual spectra to the cloud top height and the cloud optical depth. First, we change the cloud top height to 450mb, keeping the optical depth the same. Second, we double the optical depth but keep the cloud top height the same. For both cases, we calculate the residual spectra according to the method described above (the spectra are all convolved with a triangle function with 0.1cm^{-1} resolution before taking the difference). As shown in Figure 5.6a, the magnitude of the residual is decreased approximately by half when the cloud top height is changed from 250mb to 450mb. The narrow features in the residual spectra still can be seen, but these features are wider than their counterparts with cloud top at 250mb. This is consistent with the discussion in Section 5.3. As the cloud top is lowered, the features would become wider and eventually take the shape of the dash-dotted line in Figure 5.2. From Figure 5.6b, when the cloud optical depth is changed from 0.1 to 0.2, the magnitude of the residual is approximately doubled. But the features are as wide as the counterparts of optical depth 0.1. This is because the cloud top is not changed. These results show that the residual spectra can reveal not only the existence of thin cirrus by their narrow features, but also information about cloud top height and optical depth by the magnitude of the residual and the shapes of those narrow features. All these sensitivity studies assume nadir viewing. If the satellites measure radiance from a nonzero zenith angle, the cirrus optical thickness becomes larger because of the slant path. Therefore, as shown in the simulation, for the same cirrus, the amplitude of the narrow features in the residuals of retrieving non-nadir viewing spectra would be larger than those in the residuals of retrieving nadir viewing spectra.

We have shown that, in realistic simulations for an appropriate absorption line with weighting function at line center peaked around the tropopause, the narrow feature which indicates the presence of thin cirrus in the residual spectra can still be seen. The narrow feature is sensitive to the resolution of ILS and its magnitude is higher than noise levels of modern high-resolution infrared sounders. The shape and magnitude of the narrow feature are related to cloud top height and cloud optical depth.

5.5 More considerations about realistic retrieval

5.5.1 Sensitivity studies

In Sections 5.3 and 5.4 we assume that, when we misinterpret the thin cirrus case as the clear-sky case, it will introduce error only in the estimation of surface temperature. In reality when we make such misinterpretation, we will most often introduce errors in almost all the retrieved quantities. This makes the retrieval problem much more complicated. In this section, we will explore whether we can see the narrow features in the residual spectra in the presence of errors in other retrieved quantities.

First, we still use our three-layer atmosphere model to explore this problem. But this time, we assume the temperature of the bottom layer is T_b and different from the surface temperature T_s . The corresponding blackbody emission is B_b . All other configurations are same as those in Section 5.3. When the cirrus with optical depth τ_c is present in the middle layer, the radiance at the top of atmosphere with zero zenith angle is

$$\begin{aligned}
 I(x) = \exp(-\tau_c) & \left[B_s \exp\left(-\frac{C_0}{x^2 + 1}\right) + B_b \left(\exp\left(-\frac{C_1}{x^2 + 1}\right) - \exp\left(-\frac{C_0}{x^2 + 1}\right) \right) \right. \\
 & \left. + B_m \left(\exp\left(-\frac{C_2}{x^2 + 1}\right) - \exp\left(-\frac{C_1}{x^2 + 1}\right) \right) \right] + B_T \left(1 - \exp\left(-\frac{C_2}{x^2 + 1}\right) \right)
 \end{aligned} \tag{5.11}$$

Now we assume that in the retrieval, we have misinterpreted the thin cirrus as the clear-sky. To simplify the problem, we assume the gas concentration is uniform everywhere and the error in gas concentration estimation is much smaller than the error in temperature estimation, so that we can neglect the former. The retrieved surface emission from micro window region is $B_s \exp(-\tau_c)$. The retrieved emissions for three layers are $B_b + \Delta B_b$, $B_m + \Delta B_m$ and $B_T + \Delta B_T$, respectively. Define the fractional errors: $\Delta B_b / B_b = \delta_b$, $\Delta B_m / B_m = \delta_m$, and $\Delta B_T / B_T = \delta_T$. Then the calculated radiance is

$$I'(x) = \exp(-\tau_c) B_s \exp\left(-\frac{C_0}{x^2 + 1}\right) + B_b (1 + \delta_b) \left(\exp\left(-\frac{C_1}{x^2 + 1}\right) - \exp\left(-\frac{C_0}{x^2 + 1}\right)\right) + B_m (1 + \delta_m) \left(\exp\left(-\frac{C_2}{x^2 + 1}\right) - \exp\left(-\frac{C_1}{x^2 + 1}\right)\right) + B_T (1 + \delta_T) \left(1 - \exp\left(-\frac{C_2}{x^2 + 1}\right)\right) \quad (5.12)$$

Given when $\tau_c \ll 1$, $\exp(-\tau_c) \approx 1 - \tau_c$. So the residual is approximated by

$$R(x) \approx I' - I = B_b (\delta_b + \tau_c) \left(\exp\left(-\frac{C_1}{x^2 + 1}\right) - \exp\left(-\frac{C_0}{x^2 + 1}\right)\right) + B_m (\delta_m + \tau_c) \left(\exp\left(-\frac{C_2}{x^2 + 1}\right) - \exp\left(-\frac{C_1}{x^2 + 1}\right)\right) + B_T \delta_T \left(1 - \exp\left(-\frac{C_2}{x^2 + 1}\right)\right) \quad (5.13)$$

The last term on the right-hand side of (13) is the contribution from the layer above the cirrus. The presence of cirrus has more effect on the retrieval of the temperature profile below the cirrus than above the cirrus. There is also a shortcut approach known as onion peeling [Russell and Drayson, 1972], which can make this term much smaller than the other two terms on the right-hand side. For simplicity, we ignore the last term in our discussion. Obviously, if $|\delta_b|$ (or $|\delta_m|$) $\gg |\tau_c|$, the signature of cloud will be smeared out. If $|\delta_b|$ (or $|\delta_m|$) $\ll |\tau_c|$, the signature of cloud will be dominant. Therefore, it is useful for

us to estimate the threshold value of the error in temperature estimation leading to $|\delta_b|$ (or $|\delta_m| \sim |\tau_c|$). Let us assume the error of retrieved temperature is ΔT , when $\Delta T \ll T$, we have

$$B_\nu(T + \Delta T) = B_\nu(T) + \frac{\partial B_\nu(T)}{\partial T} \Delta T \quad (5.14)$$

where

$$\frac{\partial B_\nu(T)}{\partial T} = \frac{\partial}{\partial T} \left(\frac{2hv^3}{c^2 (\exp(\frac{hv}{kT}) - 1)} \right) = B_\nu(T) \frac{\exp(\frac{hv}{kT})}{\exp(\frac{hv}{kT}) - 1} \frac{hv}{kT^2} \quad (5.15)$$

So when $|\delta_m| \sim |\tau_c|$, we have

$$\Delta T = \tau_c \frac{kT^2}{hv} (1 - \exp(-\frac{hv}{kT})) \quad (5.16)$$

If $\tau_c=0.1$, for the CO₂ lines that we studied in Section 5.4, $\nu \sim 750\text{cm}^{-1}$, $T \sim 210\text{-}290\text{K}$, then $\Delta T \sim 4.3\text{-}8.0\text{K}$. This means that, when we perform the retrieval with misinterpretation of thin cirrus, if the error of retrieved temperature profile is smaller than this threshold of ΔT , then the ‘‘cloud signature’’ will be the dominant contributor to the residual spectra.

To further illustrate this point, we use LBLCARTS to carry out a sensitivity analysis. In real satellite remote sensing, the residual is calculated by differencing the measured spectrum and the synthetic spectrum based on retrieved quantities. Here, we mimic this in the following way. Using the 1976 US standard atmosphere, we divide the troposphere into four layers, the first is from 200mb to 350mb, the second from 350mb to 500mb, the third from 500mb to 750mb and the last from 750mb to surface. We do two sensitivity studies. (1) The case of clear sky. We perturb the temperatures at different layers in this way: for any two neighboring layers, the magnitude of ΔT is same but the

sign of ΔT is opposite. We assume this new temperature profile as our “retrieved” profile. We calculate the two spectra based on the original profile and this “retrieved” profile respectively. Then we take the difference to obtain the “residual” spectrum. We try two different values of ΔT , 1K and 4K. (2) The case of thin cirrus. We change the temperatures in the same way as (1). In addition, the “retrieved” profile is assumed to be without cirrus and the surface temperature is adjusted according to the description in Section 5.4. Then we can obtain the “residual” spectrum. The results are shown in Figure 5.7. It can be seen that for $\Delta T=1K$, the residuals due to the errors of temperature estimation alone are very small (Figure 5.7a), compared with the error caused by the misinterpretation of cirrus cloud as clear sky (Figure 5.7b solid line). For $\Delta T=4K$, the contribution of errors in temperature estimation to the residual (Figure 5.7c) is roughly half of that due to the misinterpretation of cirrus cloud (Figure 5.7d solid line). For both cases, the residual of case (2) is significantly larger than the residual of case (1). Therefore, if a relation between the retrieved error in temperature and the magnitude of the residual spectrum could be set up, then in a realistic retrieval, it might be possible to determine from the residual spectrum whether thin cirrus is present.

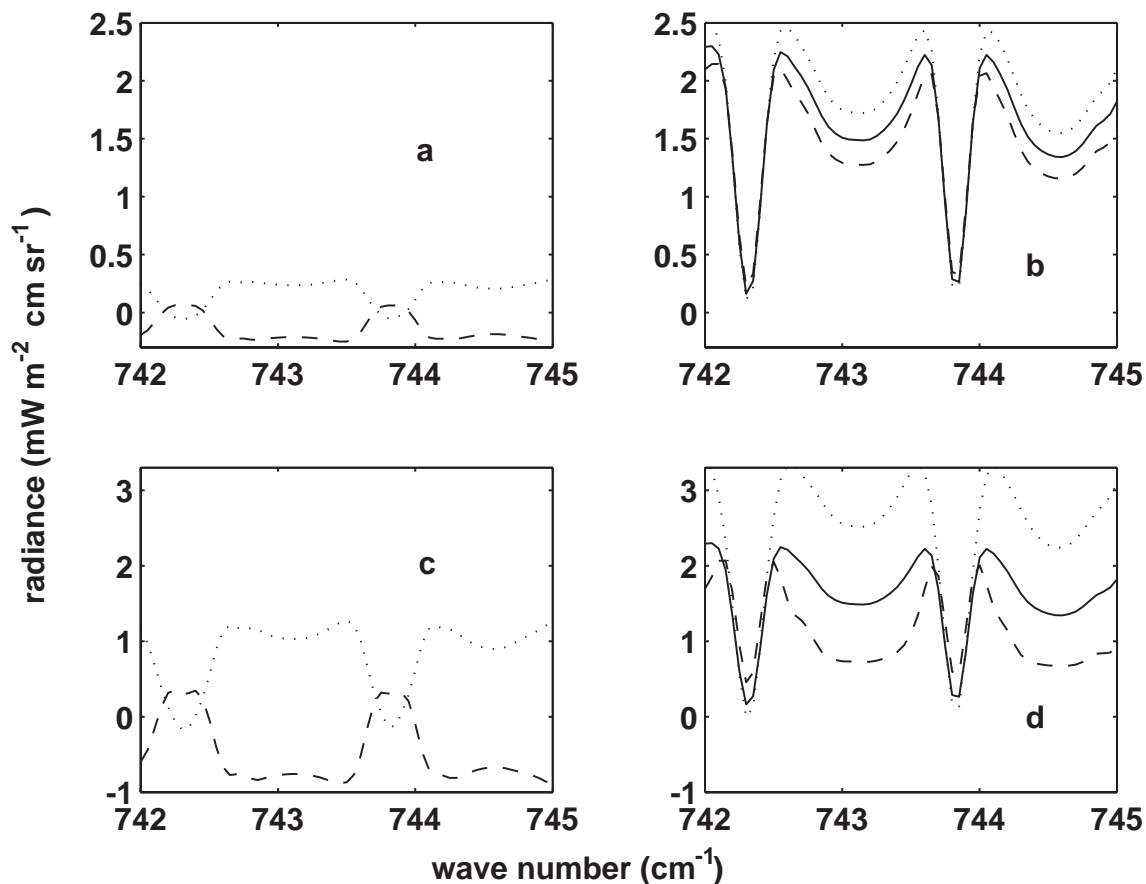


Figure 5.7 (a) The dash line is the difference of “retrieved” spectrum and original clear-sky spectrum. The original clear sky spectrum is calculated based on 1976 US standard atmosphere temperature profile and constant CO₂ mass mixing ratio of 5.0×10^{-4} . The “retrieved” spectrum is obtained by changing the temperatures in four layers (200mb- 350mb, 350mb-500mb, 500mb-750mb and 750mb-surface) by 1K and -1K alternatively. The dotted line is the difference with the “retrieved” spectrum obtained by changing the temperatures in four layers by -1K and 1K alternatively. The spectra shown here are convolved with a triangular function with FWHM = 0.1 cm⁻¹. (b) The solid line is the difference of adjusted-surface-temperature spectrum and cirrus spectrum. The dash line is the difference of “retrieved” spectrum and cirrus spectrum. The “retrieved” spectrum is obtained by adjusting the surface temperature as well as changing the temperatures in four layers by 1K and -1K alternatively. The dotted line is similar to the dash line except the “retrieved” spectrum is obtained by changing the temperatures in four layers by -1K and 1K alternatively. (c) Same as (a), except that the magnitude of temperature change is 4K. (d) Same as (b), except that the magnitude of temperature change is 4K.

Recently a sensitivity study has been carried out to assess the impact of thin clouds in atmospheric temperature retrievals [Eldering, 2002]. Synthetic spectra are created for a series of cloud optical depths using a plane parallel scattering model. Then a formal retrieval program with no scattering and an assumption of no cloud is used to retrieve atmospheric temperature profiles. When no cloud is present in the synthetic spectra, the temperature errors are about 0.5% throughout the atmosphere. When clouds are included in the generation of the synthetic spectra but not in the retrieval, temperature errors increase to about 2% at the surface level for cloud optical depths up to 0.05. At larger cloud optical depths (0.15), errors near 2% are evident at layers between the surface and the cloud height [Eldering, 2002]. In a realistic retrieval, if the errors of estimated temperature profiles are similar to those in this sensitivity study, then based on our simulation shown in this section, the “spectral signature” left by cirrus would still be clearly seen in the residual spectra.

5.5.2 From the point of view of information content

To further investigate how instrumental noise and resolution can affect the realistic retrieval in the presence of thin cirrus, we carry out the following study. Using LBLCARTS, we numerically calculate the weighting function matrix \mathbf{K} defined by $K_{ij} = \partial I_i(\mathbf{X}) / \partial x_j$ where $I_i(\mathbf{X})$ is the radiance at frequency ν_i and x_j is the j -th state variable. The state variables are temperatures at 58 levels, concentration of CO₂ (for simplicity, still assuming uniform distribution for CO₂), surface albedo, cloud optical depth and cloud height (for the case of clear sky, the last two quantities are not included). The frequency coverage is from 720 to 760 cm⁻¹ and 910 to 950 cm⁻¹, one is a strong CO₂ absorption band and the other is a weak CO₂ absorption band. Also, we create an *a priori*

covariance matrix (\mathbf{S}_a) in a way similar to that of Rodgers [2000]. We also create an error covariance matrix (\mathbf{S}_e) assuming that noise equivalent spectral radiance (NESR) is constant over the selected frequency range and the noise at other different frequencies is independent of each other. Then we calculate the degree of freedom for signal (df) based on the formula in Rodger's book [Rodgers, 2000]: $df = \sum_i \lambda_i^2 / (1 + \lambda_i^2)$ where λ_i is the singular value of the matrix $\tilde{\mathbf{K}} = \mathbf{S}_e^{-1/2} \mathbf{K} \mathbf{S}_a^{1/2}$. Here df describes the number of useful independent quantities which can be obtained in the measurements with a given error covariance matrix and an *a priori* covariance matrix. We repeat such calculation several times with varying NESR and instrumental resolution for both clear sky (df_{sky}) and thin cirrus (df_{cir}) cases and look for the differences between clear sky and thin cirrus cases, denoted by $\Delta df = df_{cir} - df_{sky}$. It can be expected that Δdf would be smaller as the instrumental resolution goes coarser, which means that less information about cloud can be retrieved. The results are summarized in Table 5.1. With instrumental resolution of 0.03 cm^{-1} and NESR smaller than $1 \text{ mW m}^{-2} \text{ cm sr}^{-1}$, Δdf is 1.5. This means that for this resolution and NESR, the thin cirrus case has 1.5 more degrees of freedom than the clear sky case. Given two cases are identical except for the presence of thin cirrus, these 1.5 degrees of freedom are solely due to thin cirrus. 1.5 degrees of freedom mean that at least one and probably two parameters related to thin cirrus can be retrieved. When the resolution is 1.0 cm^{-1} , Δdf is no more than 1.1 for the three given NESRs. Therefore, for this resolution, we can retrieve at most one quantity (maybe the combination of two parameters) about cirrus.

FWHM	NESR ($\text{mW m}^{-2} \text{cm sr}^{-1}$)	Degree of freedom (thin cirrus) df_{cir}	Degree of freedom (clear sky) df_{sky}	$\Delta df = df_{\text{cir}} - df_{\text{sky}}$
0.03 cm^{-1}	0.1	20.4	18.9	1.5
	1	14.0	12.5	1.5
	5	9.8	8.6	1.2
0.1 cm^{-1}	0.1	16.9	15.4	1.5
	1	11.3	9.9	1.4
	5	7.6	6.6	1.0
1.0 cm^{-1}	0.1	9.9	8.8	1.1
	1	5.8	5.0	0.8
	5	3.1	2.8	0.3

Table 5.1 The degrees of freedom for signal in the cases of clear sky retrieval and thin cirrus retrieval with different instrumental resolution (FWHM) and different NESR. The differences between thin cirrus cases and corresponding clear sky cases are presented in the last column.

Table 5.1 also presents the impact of NESR on the ability to detect cirrus. When NESR increases from 0.1 to $1 \text{ mW m}^{-2} \text{cm sr}^{-1}$, the difference between thin cirrus and clear sky cases (Δdf) changes little, although the degree of freedom decreases. But when NESR is greater than $1 \text{ mW m}^{-2} \text{cm sr}^{-1}$, the difference drops quickly. This can be understood in term of the cirrus “spectral signature” discussed in previous section. As long as NESR is considerably smaller than the magnitude of cirrus signature, it would not smear out the thin cirrus information in spectra. Therefore, although the degree of freedom (df_{cir} and df_{sky}) decreases as NESR becomes larger, the difference between thin cirrus and clear sky cases (Δdf) is essentially unchanged. But when NESR is larger than the magnitude of cirrus signature, it would smear out the thin cirrus information. As a result, the difference (Δdf), as well as the degree of freedom (df_{cir} and df_{sky}), is decreased when NESR increases.

The above analysis shows how the degrees of freedom for cirrus are decreased when instrumental resolution is degraded. The degrees of freedom related to thin cirrus remain the same as long as NESR is smaller than the magnitude of cirrus “spectral signature”. This is consistent with our sensitivity analysis.

5.6 Summary

In this chapter, we explore how to use the information from high spectral resolution measurements to help retrieval in the presence of thin cirrus. With the simple analytic model and LBLCARTS, we demonstrate that when thin cirrus is misinterpreted as surface emission under clear sky situation in the retrieval, the shapes of the residuals are different for absorption lines with different absorptivities. Those lines with weighting functions peaking around the tropopause show narrow features in the residual spectrum. The residual is much higher than the potential instrumental noise levels of modern high resolution infrared sounders. This holds for both uniformly distributed gas such as carbon dioxide and non-uniformly distributed gas such as methane. These narrow features are sensitive to the resolution of the ILS. For thin cirrus with optical depth 0.1, these features can be clearly seen with a resolution of the ILS of 0.1 cm^{-1} . When the resolution of the ILS is 0.5 cm^{-1} , these features cannot be seen at all. These features are also sensitive to cloud height and cloud optical depth. In reality, the issue is more complicated because the errors of other retrieved quantities also contribute to the residual spectrum. Our sensitivity simulations show that when the errors in temperature estimation are not very large, the contribution due to the misinterpretation of cirrus is still dominant in the residual. The analysis from the information point of view is also consistent with our sensitivity analysis.

To retrieve standard geophysical parameters in the presence of thin cirrus is a very complicated problem. Here, we look at this problem from the point of view of high spectral resolution measurement. We conduct some sensitivity analyses to explore how the information of high resolution can provide us additional clues for the retrieval. Realistic retrievals would follow this procedure: first apply the clear-sky retrieval routine to a spectrum, then evaluate the magnitude and the shape of residual spectrum to decide whether thin cirrus is present. If cirrus is present, try to make an estimate of cloud optical depth and cloud top height based on the residual, feed these estimates as initial guesses to the cirrus retrieval routine to retrieve the spectrum. Our future work will incorporate the ideas presented here into an operational retrieval algorithm.

5.7 Acknowledgement

We thank M. Gerstell, Z.M. Kuang for valuable comments. We also wish to thank two anonymous referees for improving the paper. This research is supported by NOAA grant Grant No. NA06EC0505 to the California Institute of Technology.

5.8 Reference

- Ackerman, S. A., H. E. Revercomb, R. O. Knuteson, and P. Antonelli, Analysis of the high-spectral resolution infrared sounder (HIS) radiances collected as part of the FIRE program, in *11th conference on Atmospheric Radiation* (American Meteorological Society), Ogden, Utah, 2002.
- Ackerman, S. A., W. L. Smith, J. D. Spinhirne, and H. E. Revercomb, The 27-28 October 1986 FIRE IFO cirrus case-study: Spectral properties of cirrus clouds in the 8-12 μm window, *Monthly Weather Review*, 118 (11), 2377-2388, 1990.

- Anderson, G. P., S. A. Clough, F. X. Kneizys, J. H. Chetwynd, and E. P. Shettle, AFGL atmospheric constituent profiles (0-120km), pp. 43, U.S. AFGL-TR-86-0110, Hanscom Air Force Base, Massachusetts, 1986.
- Aumann, H. H., and R. J. Pagano, Atmospheric Infrared Sounder on the Earth Observing System, *Optical Engineering*, 33 (3), 776-784, 1994.
- Bantges, R. J., J. E. Russell, and J. D. Haigh, Cirrus cloud top-of-atmosphere radiance spectra in the thermal infrared, *Journal of Quantitative Spectroscopy & Radiative Transfer*, 63 (2-6), 487-498, 1999.
- Baran, A. J., S. Havemann, and D. Mackowski, A database of hexagonal column optical properties for wavelengths ranging between 0.2micron to 30 micron produced from ANNEX 7, Department of the Environment, Food, and Rural Affairs, contract no. 4b/3/02, London, UK, 2002.
- Beer, R., T. A. Glavich, and D. M. Rider, Tropospheric emission spectrometer for the Earth Observing System's Aura Satellite, *Applied Optics*, 40 (15), 2356-2367, 2001.
- Diebel, D., M. Langevin, D. Klaes, P. Courtier, T. Phulpin, F. Cayla, and G. Chalon, The advanced atmospheric temperature sounder IASI-a new development for the polar satellite Metop, in *the 1997 Meteorological Satellite Data Users' Conference*, (European Organization for the Exploitation of Meteorological Satellites), Brussels, Belgium, 1997.
- Eldering, A., Jet Propulsion Laboratory, Mail Stop 183-601, 4800 Oak Grove Drive, Pasadena, California 91109 (personal communication), 2002.

Goody, R. M., and Y. L. Yung, *Atmospheric Radiation: Theoretical Basis*, 591 pp., Oxford University Press, New York, 1989.

Hansen, J. E., and L. D. Travis, Light-scattering in planetary atmospheres, *Space Science Reviews*, 16 (4), 527-610, 1974.

Hutchison, K. D., Application of AVHRR/3 imagery for the improved detection of thin cirrus clouds and specification of cloud-top phase, *Journal of Atmospheric and Oceanic Technology*, 16 (12), 1885-1899, 1999.

Hutchison, K. D., and N. J. Choe, Application of 1.38 μm imagery for thin cirrus detection in daytime imagery collected over land surfaces, *International Journal of Remote Sensing*, 17 (17), 3325-3342, 1996.

Hutchison, K. D., K. R. Hardy, and B. C. Gao, Improved detection of optically thin cirrus clouds in nighttime multispectral meteorological satellite imagery using total integrated water-vapor information, *Journal of Applied Meteorology*, 34 (5), 1161-1168, 1995.

Rodgers, C. D., Information Aspects, in *Inverse Methods for Atmospheric Sounding: Theory and Practice*, pp. 24-26, World Scientific Publishing, Singapore, 2000.

Rossow, W.B., and R.A. Schiffer, Advances in understanding clouds from ISCCP, *Bulletin of the American Meteorological Society*, 80 (11), 2261-2287, 1999.

Rothman, L. S., C. P. Rinsland, A. Goldman, S. T. Massie, D. P. Edwards, J. M. Flaud, A. Perrin, C. Camy-Peyret, V. Dana, J.Y. Mandin, J. Schroeder, A. McCann, R. R. Gamache, R. B. Wattson, K. Yoshino, K. V. Chance, K. W. Jucks, L.R. Brown, V. Nemtchinov, and P. Varanasi, The HITRAN molecular spectroscopic database

- and HAWKS (HITRAN Atmospheric Workstation): 1996 edition, *Journal of Quantitative Spectroscopy & Radiative Transfer*, 60 (5), 665-710, 1998.
- Russell, J. M., and S. R. Drayson, Inference of atmospheric ozone using satellite horizon measurements in 1042 cm^{-1} Band, *Journal of the Atmospheric Sciences*, 29 (2), 376-&, 1972.
- Schlüssel, P., and M. Goldberg, Retrieval of atmospheric temperature and water vapor from IASI measurements in partly cloudy situations, in *Remote Sensing of Trace Constituents in the Lower Stratosphere, Troposphere and the Earth's Surface: Global Observations, Air Pollution and the Atmospheric Correction*, pp. 1703-1706, 2002.
- Smith, W. L., H. M. Woolf, C. M. Hayden, D. Q. Wark, and L. M. McMillin, TIROS-N operational vertical sounder, *Bulletin of the American Meteorological Society*, 60 (10), 1177-1187, 1979.
- Stamnes, K., S. C. Tsay, W. Wiscombe, and K. Jayaweera, Numerically stable algorithm for discrete-ordinate-method radiative-transfer in multiple-scattering and emitting layered media, *Applied Optics*, 27 (12), 2502-2509, 1988.
- Takano, Y., K. N. Liou, and P. Minnis, The effects of small ice crystals on cirrus infrared radiative properties, *Journal of the Atmospheric Sciences*, 49 (16), 1487-1493, 1992.
- Turner, D. D., and S. A. Ackerman, Cloud phase and microphysical property retrieval using the atmospheric emitted radiance interferometer (AERI), in *11th conference on Atmospheric Radiation* (American Meteorological Society), Ogden, Utah, 2002.

- Wang, J. X., G. P. Anderson, H. E. Revercomb, and R. O. Knuteson, Validation of FASCOD3 and MODTRAN3: Comparison of model calculations with ground-based and airborne interferometer observations under clear-sky conditions, *Applied Optics*, 35 (30), 6028-6040, 1996.
- Warren, S. G., Optical-constants of ice from the ultraviolet to the microwave, *Applied Optics*, 23 (8), 1206-1225, 1984.
- W.M.O., The World Weather Watch Programme 1988-1997, World Meteorological Organization, Geneva, 1987.

Chapter 6: Detecting dust, water ice cloud and surface anisothermality from the Martian low-resolution outgoing thermal IR spectra: a tri-spectral approach

Xianglei Huang, Junjun Liu, Yuk L.Yung

Division of Geological and Planetary Sciences, California Institute of Technology, Pasadena, CA 91125

The majority of this chapter, together with the Chapter 4, was published in:

Huang, X.L., J.J. Liu, and Y. L. Yung, Analysis of Thermal Emission Spectrometer Data Using Spectral EOF and Tri-spectral Methods, *Icarus*, 165(2), pp.301-314, October 2003

6.1 Abstract

Here we propose a tri-spectral algorithm based on the differences between three bands (dust, ice and a weak CO₂ absorption band) to distinguish spectra sampled in different situations: water ice cloud, dust, and surface anisothermality. We use a line-by-line radiative transfer model coupled with multiple scattering to investigate the sensitivity of this algorithm to dust and ice optical depth as well as surface emissivity. The comparisons between results of this algorithm and the TES team's retrieved dust and ice opacity are consistent over all studied periods except during the peak of the dust storm. Our algorithm is complementary to the more sophisticated TES retrieval and can be used to screen large amounts of data to get an overview.

6.2 Description of tri-spectral algorithm

The tri-spectral method has been widely used in remote sensing of the terrestrial atmosphere to distinguish spectra obtained under different conditions: clear sky, liquid water cloud, and cirrus cloud (ice water cloud) [Ackerman *et al.*, 1990; Takano *et al.*, 1992]. The idea behind this method is that both ice and liquid water absorb strongly in the infrared window region (8-12 μm) but their peak absorptions occur at different frequencies. Furthermore, a weak water-vapor absorption band is also present in the window region. As a result, it is possible to discriminate cirrus, liquid water cloud and clear sky by the brightness temperature differences (ΔBT) between different bands in a scatter-plot. For example, $\Delta\text{BT}_{8\mu\text{m}-11\mu\text{m}}$ is often plotted against $\Delta\text{BT}_{11\mu\text{m}-12\mu\text{m}}$. Similarly, we design a tri-spectral scheme for Martian outgoing thermal infrared spectra. A line-by-line radiative transfer model with multiple scattering is used to study the sensitivity of this tri-spectral algorithm in the presence of varying dust and ice optical depths and surface emissivity. The tri-spectral algorithm can be used for fast screening of very large amounts of data to get first order information. This is complementary to the more sophisticated complete retrieval of dust and ice opacities [Smith *et al.*, 2000b].

Our proposed tri-spectral method is based on the following facts about Martian emission spectra [Bandfield *et al.*, 2000; Smith *et al.*, 2000a]:

- (1) The maximum absorption of water-ice is around 800cm^{-1} (12.5 μm);
- (2) The maximum absorption of dust is around 1100cm^{-1} (9 μm);
- (3) There is a weak CO_2 absorption band around 1366cm^{-1} (7.3 μm).

As a result, if the surface is a blackbody, then the brightness temperature difference between 12.5 and 9 μm is negative for icy spectra and positive for dusty spectra.

At the same time, the brightness temperature difference between 9 and 7.3 μm is negative for dusty spectra and positive for icy or clear-sky spectra because of the CO_2 weak absorption band. Compared with a simple method looking at only the brightness temperature difference between ice and dust band, this tri-spectral method uses the 7.3 μm band and thus effectively reduces the ambiguity between dusty and icy spectra.

In reality, the Martian surface is not a blackbody, and the surface emissivity must be taken into account. So we define *the effective brightness temperature* $BT_e = B^{-1}(R(\nu) / \varepsilon_s(\nu), \nu)$, where $R(\nu)$ is the measured radiance at frequency ν , $\varepsilon_s(\nu)$ is the surface emissivity at frequency ν , and $B^{-1}(R, \nu)$ is the inverse Planck function. If the atmosphere is transparent at ν , the effective brightness temperature is exactly the same as the surface temperature. When the atmosphere is opaque, complicated absorption and scattering processes make the effective brightness temperature lower than the surface temperature if the atmospheric temperature is lower than surface temperature (e.g., daytime and non-polar region) and higher than the surface temperature if the situation is the opposite (e.g., nighttime or polar region), and the physical meaning of the effective brightness temperature is not very clear. Given these facts, we use the effective brightness temperature difference only between the 9 and 7.3 μm bands and limit our analysis to 50°N to 50°S daytime spectra only. For 12.4 and 9 μm , we use just the difference of brightness temperatures. As for the values of $\varepsilon_s(\nu)$, we use 0.94 for 9 μm and 1.00 for 7.3 μm . These values are consistent with the emissivity of surface type 1 and surface type 2 derived by Bandfield *et al.* (2000). The global mean emissivity derived from one Viking IRTM channel centered at 9 μm with a band width of 1.5 μm [Christensen, 1998] is 0.941 with a standard deviation of 0.046, which is similar to the

value we choose for $9\mu\text{m}$. The values we use here might be unrealistic for the polar region, so we limit our study to the region from 50°S to 50°N . Ultimately, if the surface emissivity derived from TES can be tabulated as a function of latitude or even longitude, then more realistic values of $\varepsilon_s(\nu)$ can be used.

	$\Delta\text{BT}_{12.5-9}$	$\Delta\text{BT}_{e9-7.3}$
Icy	-	+
Dusty	+	-
Clear sky	+	+
Anisothermality or ice-dust mixture	-	-

Table 6.1 Summary of the tri-spectral algorithm to distinguish icy and dusty spectra. $\Delta\text{BT}_{12.5-9}$ refers to the brightness temperature difference between $12.4\ \mu\text{m}$ ($12.33\text{--}12.48\mu\text{m}$) and $9\mu\text{m}$ ($9.03\text{--}9.11\mu\text{m}$), $\Delta\text{BT}_{e9-7.3}$ refers to the effective brightness temperature difference between $9\mu\text{m}$ ($9.03\text{--}9.11\mu\text{m}$) and $7.3\mu\text{m}$ ($7.28\text{--}7.33\mu\text{m}$). The effective brightness temperature is defined as $BT_e = B^{-1}(R(\nu)/\varepsilon_s(\nu), \nu)$ (see text for details of this definition). For $9\mu\text{m}$, we use $\varepsilon_s(\nu) = 0.94$; for $7.3\mu\text{m}$, we use $\varepsilon_s(\nu) = 1.0$.

Our proposed tri-spectral algorithm for the Martian atmosphere is summarized in Table 6.1. As we shall see later, quite a few of the TES¹ spectra show negative signs for both $\Delta\text{BT}_{e12.5-9}$ and $\Delta\text{BT}_{e9-7.3}$. There are three possible ways for $\Delta\text{BT}_{12.5-9}$ and $\Delta\text{BT}_{e9-7.3}$ to be both negative ($\text{BT}_{12.4} < \text{BT}_9 < \text{BT}_{7.3}$):

(1) There could be enough dust in the atmosphere to make $\Delta\text{BT}_{e9-7.3}$ negative and, simultaneously, enough ice to make $\text{BT}_{12.5}$ even smaller than BT_9 .

(2) Surface anisothermality: when we observe the superposition of emission from two blackbodies with different temperatures, the observed brightness temperature at the larger wavenumber is much closer to the higher blackbody temperature than it is at the

¹ The instrumental characteristics of TES can be found in the section 4.2 of the Chapter 4.

smaller wavenumber. Therefore, if there is a horizontal surface temperature gradient, we might observe a spectrum with $BT_{12.4} < BT_9 < BT_{7.3}$. Surface anisothermality was used before to explain the dependence of thermal emission on phase angle observed by Viking IRTM (Kieffer *et al.*, 1977). The same thing can happen when part of the field of view has a thick dust or ice cloud and the rest does not.

(3) If the noise equivalent spectral radiance (NESR) is roughly constant over these bands, but the signal is decreasing from 12.4 μ m to 7.3 μ m because of the characteristics of blackbody emission at Martian surface temperature, the SNR would be decreasing too. As a result, $BT_{12.4} < BT_9 < BT_{7.3}$ might be seen even when the sky is clear and the surface and atmosphere properties are horizontally homogenous.

6.3 Sensitivity studies with a line-by-line radiative transfer model

To understand how sensitive this method is to the amount of dust or ice in the atmosphere, we conduct a sensitivity analysis using our Line-by-Line Code for Atmospheric Radiative Transfer with Scattering (LBLCARTS) (Huang *et al.*, 2003). LBLCARTS is a line-by-line radiative transfer model coupled with the DISORT code [Stamnes *et al.*, 1988] (version 1.3)¹ for multiple scattering. Sixteen streams are used in DISORT. A Voigt line profile is used in LBLCARTS and the molecular spectroscopic parameters are taken from HITRAN 2K [Rothman *et al.*, 1998]. We use a zonal-averaged temperature profile taken at the equator for northern hemisphere fall equinox, retrieved by the TES team (Smith *et al.*, 2001, plate 6). A uniform CO₂ mass mixing ratio of 0.966 is assumed. We adopt the modified gamma distribution for the dust and ice size distribution. For dust, the effective radius is 1.6 μ m and the effective variance is

¹ The code was obtained from ftp://climate.gsfc.nasa.gov/pub/wiscombe/Multiple_Scatt/DISORT1.3/

0.6 μm . For ice, the effective radius is 2.5 μm and the effective variance is 0.5 μm . Then, based on the spectral-dependent refraction index of ice [Warren, 1984] and dust [Toon *et al.*, 1977], we calculate the optical properties of cirrus using a Mie scattering code [Hansen and Travis, 1974]. The vertical profiles of dust and ice are assumed to be constant from the surface to 20km, which is same assumption used in the TES team retrieval [Pearl *et al.*, 2001]. When the water vapor mass mixing ratio is assumed to be 1.35×10^{-4} from the surface to 1mb, it turns out at the three bands considered, the optical thicknesses of water vapor are two orders of magnitude smaller than the corresponding carbon dioxide optical depths. Therefore, we exclude water vapor in our calculation.

We calculate the spectra in these three bands with varying dust and ice optical depths (hereafter, τ_{dust} refers to dust optical depth at 9 μm and τ_{ice} refers to ice optical depth at 12.4 μm) as well as 9 μm surface emissivity (hereafter, ε_9), then degrade the spectra to 10 cm^{-1} resolution and apply our tri-spectral algorithm to characterize them. Based on the spectral surface emissivity derived by Bandfield *et al.* (2000), we assume the surface emissivity at 12.4 μm (hereafter $\varepsilon_{12.4}$) is 0.985. We vary τ_{dust} and τ_{ice} from 0.1 to 0.8, and ε_9 from 0.90 to 0.98. The results are summarized in Figure 6.1

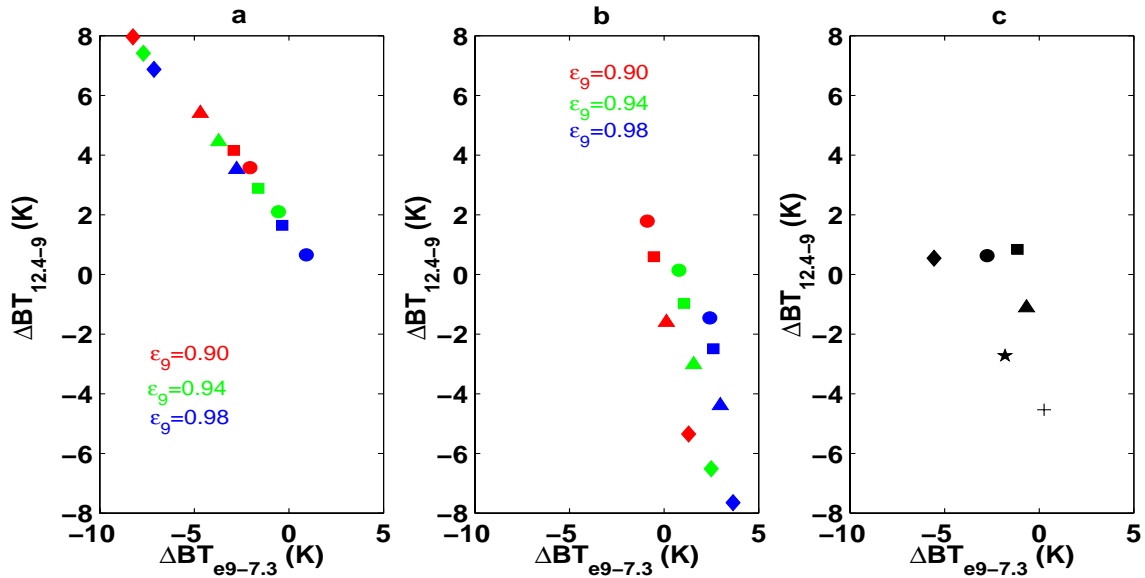


Figure 6.1 (a) The simulated $\Delta BT_{12.4-9}$ vs. $\Delta BT_{e9-7.3}$ for $\tau_{\text{dust}} = 0.1$ (circle), 0.2 (square), 0.4 (triangle), 0.8 (diamond). Red, green and blue correspond to $\epsilon_9=0.9$, $\epsilon_9=0.94$ and $\epsilon_9=0.98$ respectively. For all simulations, $\epsilon_{12.4}=0.985$. (b) The simulated $\Delta BT_{12.4-9}$ vs. $\Delta BT_{e9-7.3}$ for $\tau_{\text{ice}} = 0.1$ (circle), 0.2 (square), 0.4 (triangle), 0.8 (diamond). The color coding is same as in (a). (c) The simulated $\Delta BT_{12.4-9}$ vs. $\Delta BT_{e9-7.3}$ for different combinations of dust and ice optical depths, $\tau_{\text{dust}}=0.2$ and $\tau_{\text{ice}}=0.2$ (square), $\tau_{\text{dust}}=0.4$ and $\tau_{\text{ice}}=0.4$ (circle), $\tau_{\text{dust}}=0.8$ and $\tau_{\text{ice}}=0.8$ (diamond), $\tau_{\text{dust}}=0.2$ and $\tau_{\text{ice}}=0.4$ (triangle), $\tau_{\text{dust}}=0.2$ and $\tau_{\text{ice}}=0.8$ (plus), $\tau_{\text{dust}}=0.4$ and $\tau_{\text{ice}}=0.8$ (star). For all simulations, $\epsilon_9=0.94$, $\epsilon_{12.4}=0.985$.

For dust (Figure 6.1a), when $\epsilon_9 = 0.98$, the detectable threshold is $\tau_{\text{dust}}=0.2$. This is because we use $\epsilon_9 = 0.94$ in our algorithm, so the effective brightness temperature at $9 \mu\text{m}$ is overestimated. For $\epsilon_9 = 0.94$ and $\epsilon_9 = 0.90$, the detectable threshold is $\tau = 0.1$ or less. For ice, it can be seen from Figure 6.1b that when $\epsilon_9=0.9$, spectra with τ_{ice} up to 0.2 are still misclassified. This is because $\epsilon_{12.4}$ is much higher than ϵ_9 . As a result, a large optical depth is needed to bring the brightness temperature at $12.4 \mu\text{m}$ down below the brightness temperature at $9 \mu\text{m}$. For $\epsilon_9 = 0.94$, ice optical depth larger than 0.1 is

detectable by this tri-spectral algorithm. For $\varepsilon_9 = 0.98$, optical depth as small as 0.1 is detectable because the difference of surface emissivity for the two bands is small.

We also carry out case studies for the coexistence of dust and ice in the atmosphere. We do this study only for $\varepsilon_9=0.94$ and vary τ_{dust} and τ_{ice} from 0.2 to 0.8. The results are presented in Figure 6.1c. It shows that when τ_{dust} is larger than the detectable threshold and τ_{ice} is no more than τ_{dust} , the tri-spectral algorithm will classify it as a dusty spectrum. When τ_{ice} is larger than τ_{dust} by a factor of 2, the spectrum falls into the third quadrant, the heterogeneous quadrant. Therefore, if we use only the tri-spectral algorithm, this case would be indistinguishable from the surface anisothermality case. When τ_{ice} is larger than τ_{dust} by a factor of 4, the spectrum will be classified as an icy spectrum.

The sensitivity studies here are admittedly crude given that we use only one temperature profile in our sensitivity studies and assume a constant mixing ratio of water-ice cloud from the surface to 20km. The lower the lapse rate is, the lower the sensitivities are. This can be shown in an extreme case where the lapse rate is zero. In this case, the atmosphere and the surface have the same temperature. According to Kirchhoff's Law, the outgoing spectrum is the blackbody spectrum if the surface emissivity is unity. Then the brightness temperature differences for any two frequencies are zero and nothing can be detected. Also, uncertainty exists in the optical properties and size distribution of dust and water-ice clouds. However, through these studies we can understand the limitation of tri-spectral algorithm and how the surface emissivity could have an effect on its results.

6.4 Case studies and comparison with TES retrievals

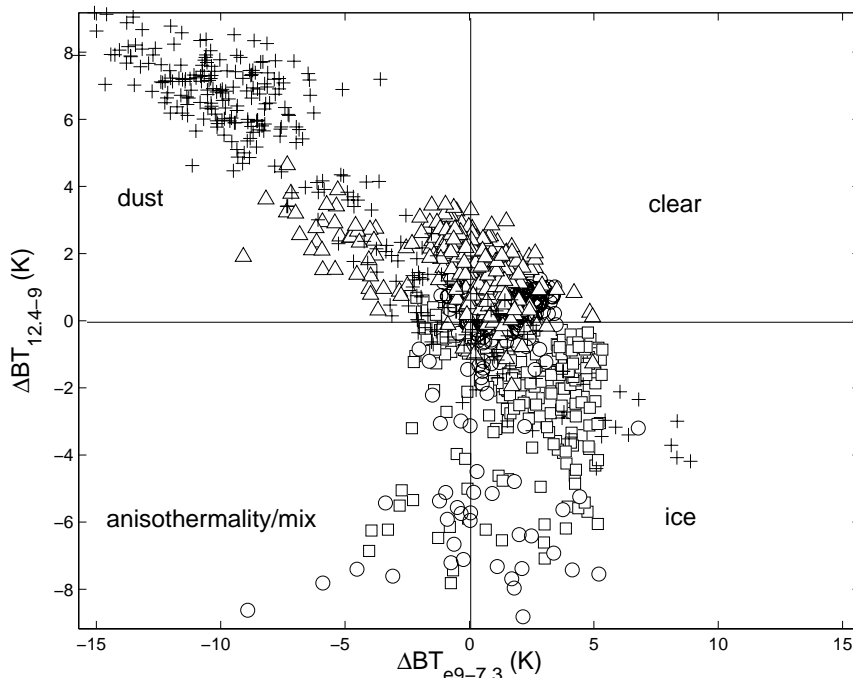


Figure 6.2 Squares are $\Delta BT_{12.4-9}$ vs. $\Delta BT_{e9-7.3}$ of 300 TES daytime spectra randomly selected from volume mgst1229 over 50°S - 50°N . Circles, triangles and pluses are the same as squares except that they are from volume mgst1232, 1238 and 1245, respectively.

To apply our tri-spectral method to the TES data, we select four volumes of TES data of the second MGS mapping year: mgst1229 (Solar longitude $L_s = 139^{\circ}$ to 142°), mgst1232 ($L_s = 149^{\circ}$ to 153°), mgst1238 ($L_s = 179^{\circ}$ to 183°) and mgst1245 ($L_s = 206^{\circ}$ to 210°). Mgst1229 corresponds to an ice-rich period while mgst1245 corresponds to a dust-rich period. Mgst1232 is a period between the ice-rich and dust-rich period, and mgst1238 is the very beginning of the global dust storm. We limit our selection of spectra to 50°N - 50°S , around 2PM (for the reason stated in Section 6.2), and double scan mode (5cm^{-1} resolution), one detector (detector 3) only to reduce the amount of data to be processed.

First, from each volume, we randomly choose 300 spectra for analysis by the tri-spectral algorithm. The results are summarized in Figure 6.2. It can be seen that most

spectra chosen from mgst1229 fall into the “ice quadrant” and most spectra from mgst1238 and mgst1245 fall into the “dust quadrant”. There are quite a few spectra in the third quadrant with both $\Delta BT_{12.5-9}$ and $\Delta BT_{e9-7.3}$ being negative. As we discussed in Section 6.2, there are three possible explanations. From the sensitivity studies in Section 6.3, it can be seen that if coexistence of dust and ice makes $\Delta BT_{12.5-9}$ and $\Delta BT_{e9-7.3}$ both negative, then the optical depth of ice should be larger than that of dust. From previous studies (Smith *et al.* 2001, plate 1) we can see that except for a few locations and times, this is unlikely. Therefore, surface anisothermality might be responsible for most spectra falling into the third quadrant.

To further show the effect of surface anisothermality on the spectrum, we pick a sample spectrum from TES data (Figure 6.3a solid line). The corresponding topography map is shown in Figure 6.3b. Using our tri-spectral method, it falls into the third quadrant. Also, the TES team retrieved dust and ice opacities for this spectrum are both smaller than 0.05. If we assume the surface in the field of view is composed of two areas with different surface temperature (e.g. shadow area and flat area both inside the field of view), we can model the radiance in the transparent region ($400-600 \text{ cm}^{-1}$, $1200-1400 \text{ cm}^{-1}$) as

$$R(\nu) = \alpha B(\nu, T_1) + (1 - \alpha) B(\nu, T_2) \quad (4)$$

where α is the fraction of area with surface temperature T_1 . Then we can get the best estimates of T_1 , T_2 and α simply by the grid search method. The dashed line presented in Figure 6.3a is the result of the grid search method. It is a superposition of two areas with about 60K surface brightness temperature difference: one occupies 33% of total area with brightness temperature of 257.6 K and the other occupied 67% of total area with

brightness temperature of 199.6 K. Our model here is an over-simplified model for surface anisothermality. The result is only qualitatively reliable. But it shows that large surface anisothermality is needed to interpret this spectrum. Several factors can contribute to this surface anisothermality: (1) given that this spectrum was taken during Southern winter ($L_s=139.2^\circ$) at 41° south, if some parts of the footprint are covered by patchy surface ice, it would make the temperature over surface ice much lower than that over surface directly exposed to sunlight; (2) the emissivity may be different from one part to the other part inside the footprint; (3) surface roughness inside the footprint, detailed modeling studies (Colwell and Jakosky, 2002) show that surface roughness can strongly alter the slope of an outgoing thermal infrared spectrum. Colwell and Jakosky (2002) also show that the larger the solar incidence angle, the stronger is the change of slope. This is mainly due to more areas in the shadow at large incident angle. For this case, the solar incidence angle is 68.6° . Therefore, surface roughness can also contribute to the surface anisothermality.

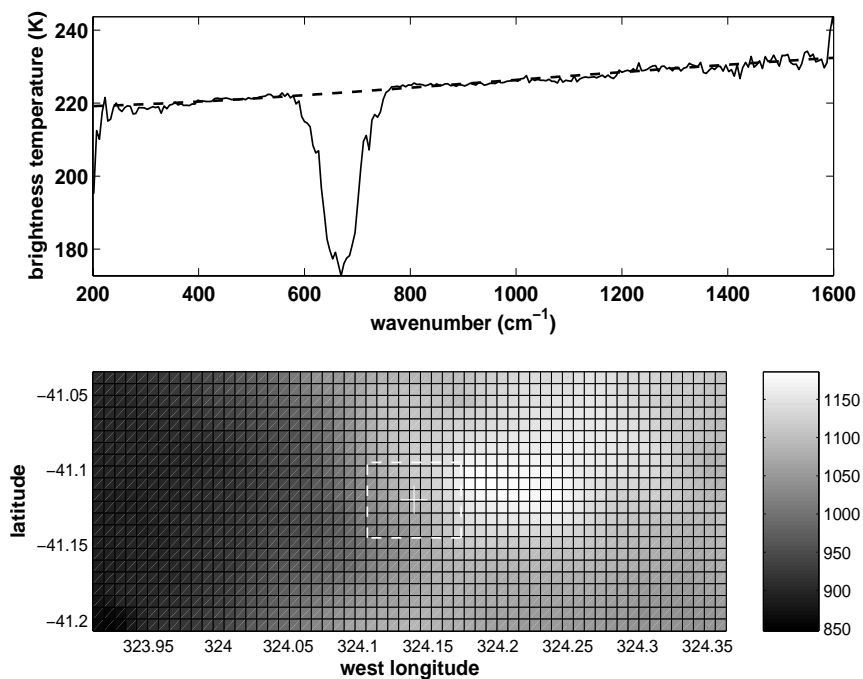


Figure 6.3 (a) The solid line is a TES spectrum collected at 41.12°S, 324.14°W, $L_s=139.2^\circ$, local time=14.685 by detector 3 at spacecraft clock time 670599978. The solar incidence angle is 68.61° and the phase angle is 68.36° . The dashed line is a fit to radiance in the transparent spectral range ($400\text{-}600\text{ cm}^{-1}$, $1200\text{-}1400\text{ cm}^{-1}$) with the superposition of two areas with different surface temperatures (see text). (b) The 20km-by-10km topography map centered at 41.12°S, 324.14°W. The topography data is from MOLA MEGDR global topographic maps at resolution of 128 pixels per degree available from <http://wufs.wustl.edu/missions/mgs/mola/megdr.html>. The TES footprint is about the rectangle in white dashed line. The elevation unit is meters.

To further study the relation between the spectra falling into the third quadrant and surface anisothermality, we apply the tri-spectral algorithm to all spectra chosen with the criteria stated in the first paragraph of this section. Figure 6.4a and Figure 6.4b are the geographic distributions of all spectra with $BT_{12.4} < BT_9 < BT_{7.3}$ in volume mgst1229 and mgst1232, respectively. It can be seen that, to some extent, geographic distributions of these spectra are correlated with surface roughness because surface roughness can

produce surface anisothermality at a scale comparable to the footprint of TES. Few such spectra come from Utopia planitia, Acadia planitia, Amazonis planitia and Tharsis montes, four regions where the surface roughness is low [Aharonson *et al.*, 2001]. Moreover, the majority of these spectra come from the part of southern hemisphere where the surface roughness is known to be large. For the volumes mgst1238 and mgst1245, which are not shown here, we also see few observations of such spectra in the low surface roughness regions, but the number of spectra in the high surface roughness regions is also small. We speculate that the dust storm makes the atmosphere more opaque so that the effect of surface heterogeneity is masked. We conclude that this tri-spectral algorithm might be useful in detecting the surface anisothermality.

We can compare our results with results retrieved by the TES team. The TES team provides retrieved ice and dust optical depth as well as other retrieved quantities in TES data version 2. For this comparison, besides those criteria stated in the first paragraph of this section, additional constraints are the brightness temperature over the continuum region larger than 220K and retrieved CO₂ optical depth in the hot and isotope bands between -0.01 and 0.05. These constraints are recommended by the TES team for opacity users¹. For those qualified spectra we use the tri-spectral algorithm to classify them, and then display them in a scatter-plot with respect to the TES team's retrieved dust and water-ice opacities. The results are summarized in Figure 6.5. It clearly shows the dominance of icy spectra in the ice-rich period and the dominance of dusty spectra in the dust-rich period and the transitions from ice-rich to dust-rich period. When dust and

¹ A sample of such document can be found at http://wufs.wustl.edu/geodata/mgs-m-tes-3-tsdr-v2/mgst_1262/data/mars/atm.fmt

ice opacity is small, there is quite a lot of overlap between the scatter-plots of icy spectra and dusty spectra. It shows again that the tri-spectral algorithm is not sensitive to small opacities. As the dust and ice opacities become larger, the scatter-plots of dusty and icy spectra classified by the tri-spectral algorithm are well separated. Moreover, if we draw a straight line to separate dusty and icy spectra in our scatter plots, the slope of this line is almost same for volumes mgst1229, mgst1232 and mgst1238. The relations between the tri-spectral algorithm and TES team retrieved opacities are consistent over these three volumes.

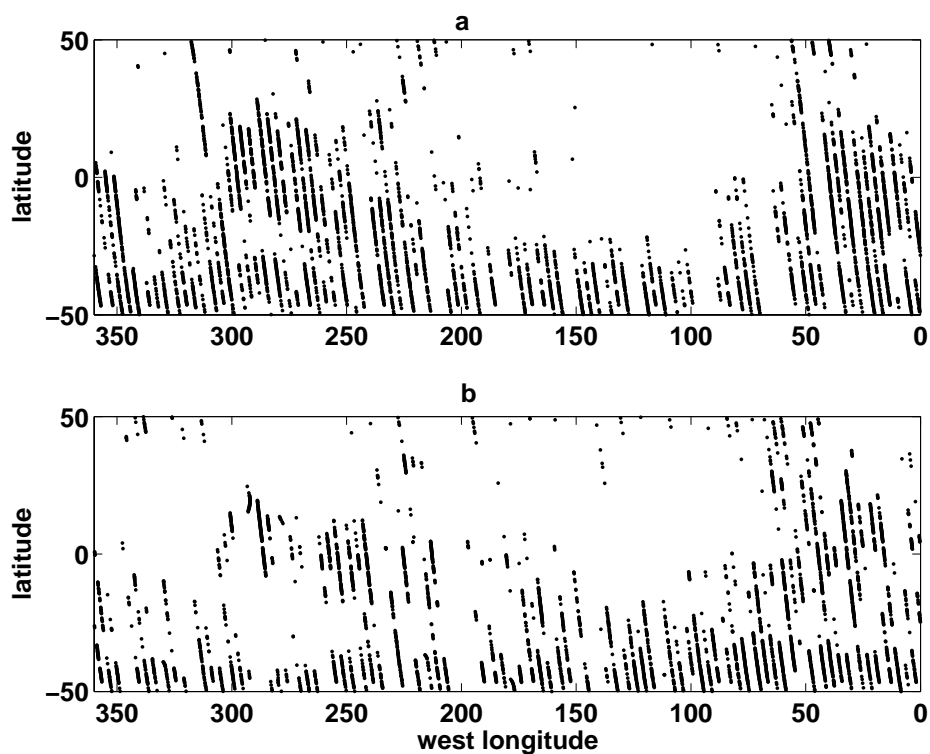


Figure 6.4 (a) Geographical distribution of all TES daytime spectra in volume mgst1229 over 50°S-50°N with $\Delta BT_{12,4-9} < 0$ and $\Delta BT_{e9,7,3} < 0$. Each dark point represents one spectrum. (b) Same as (a) except the volume is mgst1232.

For volume mgst1245, a period around the peak of the global dust storm, the scatter plot of dusty and icy spectra (Figure 6.5d) is not similar to the plots of the other volumes. As Smith *et al.* (2001) mentioned, the non-scattering assumptions used in the TES team retrieval is only qualitatively useful for the dust storm peak period during which the dust optical depth reaches unity or even higher. On the other hand, the number of icy spectra classified by the tri-spectral algorithm is only 1.1% of the number of dusty spectra. When we map the distribution of these 108 icy spectra in Figure 6.6, we can see that they are largely confined to regions that are known to have icy features during this period. Many icy spectra come from Hellas planitia and Argyre planitia. Ice clouds could be there because of the slope effect due to the deep low terrain. We also see some icy spectra in the zonal band 45°S -50°S. Given that mgst1245 is coincident with the period of polar cap retreat, these icy spectra might be due to the residue of the polar ice cap. Icy spectra in the zonal band 40°N-50°N are caused by water ice clouds in the northern subpolar region during northern winter [Zurek *et al.*, 1992].

In summary, we apply the tri-spectral algorithm to analyze the TES data and show that this algorithm can detect surface anisothermality as well as dust and ice in the atmosphere. The comparisons with TES retrieved dust and ice opacities show good consistency over different periods except during the peak of the global dust storm. The geographic distribution of icy spectra during the global dust storm peak period is reasonable. This shows the tri-spectral algorithm is at least partially valid during a global dust-rich period.

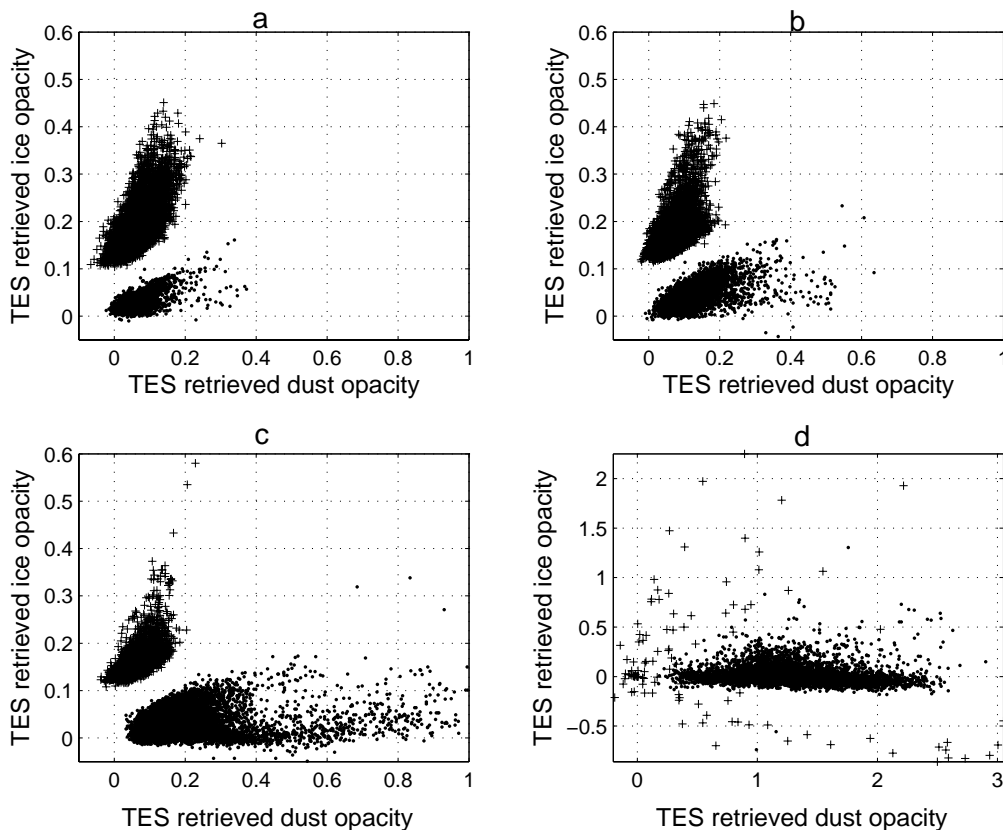


Figure 6.5 (a) The scatter-plot of the TES team's retrieved dust opacity vs. its retrieved ice opacity for qualified TES daytime spectra in volume mgst1229 (refer to text for details of the qualification). The pluses denote icy spectra classified by the tri-spectral algorithm (offset by 0.1 in retrieved ice opacity for clarity) and the dots are dusty spectra classified by the tri-spectral algorithm. There are 11420 spectra classified by the tri-spectral algorithm as icy spectra and 3112 spectra as dusty spectra. (b) Same as (a) except that data are from mgst1232. The total numbers of icy and dusty spectra are 7099 and 7882, respectively. (c) Same as (a) except that data are from mgst1238. The total numbers of icy and dusty spectra are 2676 and 17377, respectively. (d) Same as (a) except that data are from mgst1245 and there is no offset for icy spectra classified by the tri-spectral algorithm. The total numbers of icy and dusty spectra are 108 and 8753, respectively.

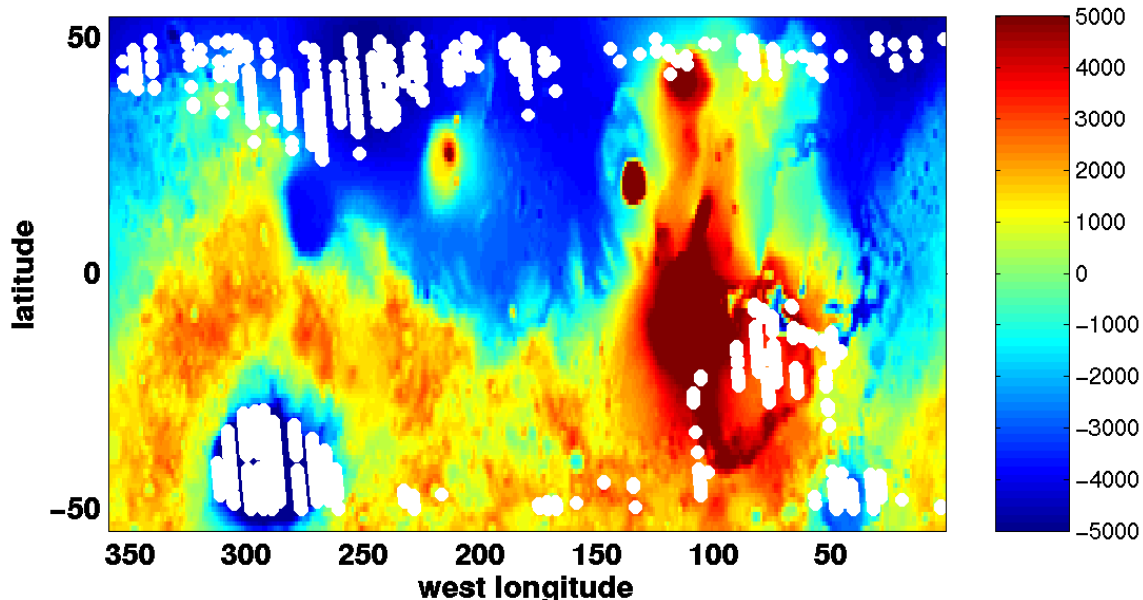


Figure 6.6 The white circular dots are the locations of those daytime spectra classified as icy spectra in volume mgst1245 (dust-rich period). The background is the Mars topography map. The unit for topography is meters.

6.5 Summary

Including the CO₂ weak absorption band in the tri-spectral algorithm decreases the ambiguity between cloud and ice and surface heterogeneity. The tri-spectral algorithm is capable of processing a very large amount of data quickly, which makes it supplementary to more sophisticated retrieval such as that used by the TES team. The sensitivity studies show that the applicability of the tri-spectral algorithm depends on how well we know the surface emissivity. With the expected success of mapping by the TES team, reliable surface spectral emissivity data will become available. These data, with the tri-spectral algorithm, can be useful for analyzing infrared spectral observations of the Martian atmosphere.

6.6 Acknowledgement

We thank S. Byrne, M. Gerstell, A. Ingersoll, T. Martin and M. Richardson for helpful discussions. We are greatly indebted to M. Richardson for his help in accessing TES data. One of the authors, Y.L. Yung, is indebted to T. Martin for pointing out the importance of anisothermality. We also thank two referees, including J. L. Bandfield for greatly improving the paper. This research was supported by NASA grant NAGS-10724 to the California Institute of Technology.

6.7 References

- Ackerman, S. A., W. L. Smith, J. D. Spinhirne, and H. E. Revercomb, The 27-28 October 1986 FIRE IFO cirrus case-study: Spectral properties of cirrus clouds in the 8-12 μm Window, *Monthly Weather Review*, 118 (11), 2377-2388, 1990.
- Aharonson, O., M. T. Zuber, and D. H. Rothman, Statistics of Mars' topography from the Mars Orbiter Laser Altimeter: Slopes, correlations, and physical Models, *Journal of Geophysical Research-Planets*, 106 (E10), 23723-23735, 2001.
- Bandfield, J.L., V. E. Hamilton, and P. R. Christensen, A global view of Martian surface compositions from MGS-TES, *Science*, 287 (5458), 1626-1630, 2000.
- Christensen, P. R., Variations in Martian surface composition and cloud occurrence determined from thermal infrared spectroscopy: Analysis of Viking and Mariner 9 data, *Journal of Geophysical Research-Planets*, 103 (E1), 1733-1746, 1998.
- Hansen, J. E., and L. D. Travis, Light-scattering in planetary atmospheres, *Space Science Reviews*, 16 (4), 527-610, 1974.
- Pearl, J. C., M. D. Smith, B. J. Conrath, J. L. Bandfield, and P. R. Christensen, Observations of Martian ice clouds by the Mars Global Surveyor Thermal

- Emission Spectrometer: The First Martian year, *Journal of Geophysical Research-Planets*, 106 (E6), 12325-12338, 2001.
- Rothman, L. S., C. P. Rinsland, A. Goldman, S. T. Massie, D. P. Edwards, J. M. Flaud, A. Perrin, C. Camy-Peyret, V. Dana, J.Y. Mandin, J. Schroeder, A. McCann, R. R. Gamache, R. B. Wattson, K. Yoshino, K. V. Chance, K. W. Jucks, L. R. Brown, V. Nemtchinov, and P. Varanasi, The HITRAN molecular spectroscopic database and HAWKS (HITRAN Atmospheric Workstation): 1996 edition, *Journal of Quantitative Spectroscopy & Radiative Transfer*, 60 (5), 665-710, 1998.
- Smith, M. D., J. L. Bandfield, and P. R. Christensen, Separation of atmospheric and surface spectral features in Mars Global Surveyor Thermal Emission Spectrometer (TES) spectra, *Journal of Geophysical Research-Planets*, 105 (E4), 9589-9607, 2000a.
- Smith, M. D., J. C. Pearl, B. J. Conrath, and P. R. Christensen, Mars Global Surveyor Thermal Emission Spectrometer (TES) observations of dust opacity during aerobraking and science phasing, *Journal of Geophysical Research-Planets*, 105 (E4), 9539-9552, 2000b.
- Stamnes, K., S. C. Tsay, W. Wiscombe, and K. Jayaweera, Numerically stable algorithm for discrete-ordinate-method radiative-transfer in multiple-scattering and emitting layered media, *Applied Optics*, 27 (12), 2502-2509, 1988.
- Takano, Y., K. N. Liou, and P. Minnis, The effects of small ice crystals on cirrus infrared radiative properties, *Journal of the Atmospheric Sciences*, 49 (16), 1487-1493, 1992.

Toon, O. B., J. B. Pollack, and C. Sagan, Physical properties of the particles composing the Martian dust storm of 1971-1972, *Icarus*, 30, 663-696, 1977.

Warren, S. G., Optical-constants of ice from the ultraviolet to the microwave, *Applied Optics*, 23 (8), 1206-1225, 1984.

Zurek, R. W., J. R. Barnes, R. Haberle, J. B. Pollack, J. E. Tillman, and C. Leovy, Dynamics of the atmosphere of Mars, in *MARS*, edited by H. H. Kieffer, B. M. Jakosky, C. W. Snyder, and M. S. Matthews, pp. 860, The University of Arizona Press, Tucson & London, 1992.